



Supplementary Materials for

Toward a Cenozoic history of atmospheric CO₂

The Cenozoic CO₂ Proxy Integration Project (CenCO₂PIP) Consortium

Corresponding authors: Bärbel Hönlisch, hoenisch@ldeo.columbia.edu; Dana L. Royer, droyer@wesleyan.edu;
Daniel O. Breecker, breecker@jsg.utexas.edu; Gabriel J. Bowen, gabe.bowen@utah.edu; Pratiqya J. Polissar,
polissar@ucsc.edu; Andy Ridgwell, andy@seao2.org

Science **382**, eadi5177 (2023)

DOI: [10.1126/science.adi5177](https://doi.org/10.1126/science.adi5177)

The PDF file includes:

Supplementary Text

Figs. S1 to S13

Tables S1 to S3

References

Supplementary Text

This supplementary information details the procedures reported in the main text. Sections 1-8 provide the current understanding of each paleo-CO₂ proxy, the criteria for vetting, categorizing and revising individual records, and future directions for further proxy validation and improvement. Of these, Section 1 is the most detailed because the theory behind the phytoplankton proxy is currently being re-evaluated. Section 9 describes the approximation of age uncertainties assigned to marine paleo-CO₂ estimates. Section 10 describes the model for estimating the joint evolution of Cenozoic CO₂ as constrained by the compiled Category 1 proxy data, including alternative scenarios calculated at 100-kyr and 1-Myr resolution. This section also includes a figure displaying the number of data and proxies included in each 500-kyr timestep, an assessment of the last time CO₂ was as high as today, and a comparison of our results with a previous estimate by Hansen et al. (44). Table S1 summarizes the vetting criteria for classifying each proxy into data categories 1, 2, or 3. The specific categorization criteria for individual records and data points are reported in the product data sheets for each record, which are archived in [NCEI](#). Table S2 provides an index to guide the reader to details for each proxy, as described in Sections 1-8. Table S3 provides the age uncertainty estimates assigned to those marine records that were published without such estimates.

1. Phytoplankton

1.1. Current understanding of the phytoplankton proxy and recent advances

Reconstructing paleo-CO₂ from carbon isotope ratios in algal organic matter is based on the difference in ¹³C/¹²C isotope ratios between aqueous CO₂ and the organic products of photosynthesis (118-120). In both laboratory cultures (e.g., 121) and open marine settings (122, 123), the magnitude of phytoplanktic isotope fractionation (ϵ_p) is positively correlated to the ambient [CO_{2(aq)}]. The predominantly invoked explanation describes this relationship based on principles of diffusive supply and demand: as [CO_{2(aq)}] increases, so too does the diffusive influx of CO₂. This results in less complete CO₂ utilization by the organism and allows more discrimination between the two carbon isotopes (124, 125). Thus, ϵ_p is large when CO_{2,atm} and [CO_{2(aq)}] are high, and ϵ_p is small when CO_{2,atm} and [CO_{2(aq)}] are low; this general relationship is used for paleobarometry not only in the Cenozoic (e.g., 126), but throughout the Phanerozoic (127).

The mechanism behind variation in ϵ_p is believed to lie with kinetic rate differences between the transport and fixation of ¹³CO₂ vs. ¹²CO₂ during irreversible step(s) of the net photosynthetic process. The CO₂-fixing enzyme ribulose 1,5-bisphosphate carboxylase/oxygenase (RuBisCO) in plants and algae preferentially utilizes ¹²CO₂, yielding a primary photosynthate that is 11-30‰ depleted in ¹³C relative to the CO₂ supply (128-132). In addition to [CO_{2(aq)}] and the effect of RuBisCO, algal culture experiments have identified other factors that contribute to the net expression of ϵ_p . These variables include growth rate, cell size and geometry, species, growth conditions such as nutrient or light limitation, and potentially the expression of carbon concentrating mechanisms (CCMs) (121, 133-136).

Because algal species vary across many of the above parameters, the community has traditionally tried to reduce this variability by focusing on biomarkers with well-constrained biological sources, such as alkenones, which are produced exclusively by coccolithophorid algae belonging to the order Isochrysidales (clade Haptophyta). These are the organisms also utilized for the $U_{37}^{K'}$ alkenone paleotemperature index (e.g., 137). Other than the datasets of Witkowski et al. (127) and Mejía et al. (138), which use the generic compound phytane and diatom-bound organic carbon, respectively, all phytoplankton data in the present compilation represent alkenone ϵ_p values. [Error! Reference source not found.](#)[Error! Reference source not found.](#)[Error! Reference source not found.](#)[Return to Error! Reference source not found.](#)[Error! Reference source not found.](#)[Error! Reference source not found.](#)**Table S2.**

1.2. Details of theory

1.2.1. Method 1 - Traditional Framework

The photosynthetic fractionation of carbon isotopes, ϵ_p , is calculated from estimates of the $\delta^{13}C$ values of CO₂ and biomass (Eq. 1.1):

$$\epsilon_p = \left[\frac{\delta^{13}C_{CO_2(aq)} + 1000}{\delta^{13}C_{biomass} + 1000} - 1 \right] \cdot 1000 \cong \delta^{13}C_{CO_2(aq)} - \delta^{13}C_{biomass} \quad (\text{Eq. 1.1})$$

The former are reconstructed from sedimentary carbonates (such as planktic foraminifera) and estimates of local sea-surface temperature, while the latter are from biomarkers corrected for biosynthetic offsets from bulk cellular biomass $\delta^{13}\text{C}$. For more details, see section 1.4.

The classical framework for using alkenone-derived ε_p values to reconstruct atmospheric CO_2 (139, 140) assumes that ε_p changes in an inverse linear relationship to the ratio of carbon demand to $[\text{CO}_{2(\text{aq})}]$:

$$\varepsilon_p = \varepsilon_f - \frac{b}{[\text{CO}_{2(\text{aq})}]} \quad (\text{Eq. 1.2})$$

Here, ε_f is assumed to be the maximum expressed fractionation by RuBisCO at the limit of infinite CO_2 (generally taken as 25 to 28‰). The b term represents all non- $[\text{CO}_{2(\text{aq})}]$ effects on ε_p , including growth rate and all other biological controls on carbon demand. This relationship has been the basis for paleo- CO_2 reconstructions from alkenones (e.g., 141) and other algal biomarkers such as chlorophyll and its degradation products (119, 120), phytane and phytol (cf. 127), and the C_{17} n -alkane (e.g., 142). Atmospheric $p\text{CO}_2$ is calculated using the temperature and salinity-adjusted Henry's law constant, K_H (143).

Equation 1.2 requires an input value for the parameter b . The conventional strategy to determine b for a given location uses empirical calibrations of modern samples that show a linear correlation between b and *in-situ* surface ocean $[\text{PO}_4^{3-}]$. The value of b is calculated using measured ε_p and $[\text{CO}_{2(\text{aq})}]$ data for modern phytoplankton samples and/or core-tops, and then is correlated with measurements or best estimates for the local PO_4^{3-} concentrations in the photic zone:

$$b = (\varepsilon_f - \varepsilon_p)[\text{CO}_{2(\text{aq})}]; \text{ } b \text{ plotted vs. } [\text{PO}_4^{3-}] \text{ to yield } b = A + B[\text{PO}_4] \quad (\text{Eq. 1.3})$$

For paleobarometry applications, the modern or modeled $[\text{PO}_4^{3-}]$ in surface waters overlying the core location (often back-projected to its paleo latitude/longitude) is used in Eq. 1.3, enabling calculation of a single location-specific b value to plug into Eq. 1.2. Various solutions for the calibration parameters A and B have been proposed. Historically, most applications have used $b = 119[\text{PO}_4^{3-}] + 84$ (126). Here we use a recently updated compilation (144), filtered to include only photic zone samples from the water column (Figure S1, $b=130[\text{PO}_4^{3-}]+93$). Sediment core-top values were not used due to uncertainties in the age and duration over which these sediments accumulated and therefore corresponding difficulty in assigning their appropriate $[\text{CO}_{2(\text{aq})}]$ and $[\text{PO}_4^{3-}]$ reference values. This approach is hereafter called Method 1, or the “traditional b ” method. More recently, several modified approaches have been developed to account for some of the underlying physiological complexity encompassed by the parameter b . These revised schemes are elaborated in sections 1.2.2-1.2.4, where they are called Methods 2, 3, and 4.

Factors underlying the b parameter. A theoretical model by Rau et al. (145) proposed a formal description of the physiological parameters underlying ε_p . In this framework, the fractionation is related to the cellular carbon budget, τ (adapted from 146), which is defined by the ratio of carbon demand to diffusive CO_2 supply (both mol C s^{-1}) (Eq. 1.4).

$$\tau = \frac{\text{C demand}}{\text{C supply}} = \frac{V \cdot [C_{\text{cell}}] \cdot \mu_i}{SA \cdot P_C \cdot [\text{CO}_{2(\text{aq})}]} \quad (\text{Eq. 1.4})$$

This implies τ is a unitless ratio, where V is cell volume (m^3), $[C_{\text{cell}}]$ is the organic carbon density of the cell (mol C m^{-3}), μ_i (seconds^{-1}) is the photoperiod-normalized (also termed instantaneous) growth rate (per second, 134), SA is the surface area (m^2), P_C is the permeability of the cell membrane to diffusion of aqueous CO_2 (m s^{-1}), and $\text{CO}_{2(\text{aq})}$ is in units of mol m^{-3} ; thus the numerator and denominator are each mol C s^{-1} . Note that some versions of Eq. 1.4 replace $V \cdot [C_{\text{cell}}]$ with POC (particulate organic carbon, mol C cell^{-1}).

Expression in this form easily shows how ε_p is a function of the relative degree of carbon utilization (τ) and the isotope effects of diffusive transport (ε_t) and carbon fixation (ε_f):

$$\varepsilon_p = \varepsilon_f - (\varepsilon_f - \varepsilon_t)\tau \quad (\text{Eq. 1.5})$$

Since ε_t is nearly zero in aqueous systems (147), when C demand and supply are equal (τ approaching 1), ε_p approaches zero. Conversely, decreases in C demand or increases in C supply (lower τ) increase ε_p . Thus, b accounts for all the physiological (i.e., non- $[\text{CO}_{2(\text{aq})}]$) components of τ :

$$b = (\varepsilon_f - \varepsilon_t)[\text{CO}_{2(\text{aq})}]\tau = (\varepsilon_f - \varepsilon_t) \frac{V \cdot [C_{\text{cell}}] \cdot \mu_i}{SA \cdot P_C} \quad (\text{Eq. 1.6})$$

The implications of understanding b as a shorthand for net cellular properties include the realization that cell geometry significantly impacts the expression of ε_p (145, 148). Traditional alkenone biomarker paleo- CO_2 reconstructions reduce this complexity due to the spherical geometry of Isochrysidales, but do not completely account for the changing V:SA ratios that accompany changes in cell size.

Several recent studies discuss the relative importance of incorporating these additional physiological parameters (39-41, 138, 144, 149-152). The proposed modifications fall into two categories: (i) modulating b using size-scaling and growth rate relationships, or (ii), empirical approaches based upon the response of ε_p to $[\text{CO}_{2(\text{aq})}]$ observed in laboratory cultures. [Return to Error! Reference source not found.](#)

1.2.2. Method 2 - size correction

The first major correction developed for the diffusive b model was based on the recognition that coccolith length scales with cell radius (Figure S2) (38).

This relationship was then applied to sedimentary alkenone paleo- CO_2 records using co-occurring fossil coccoliths to adjust the value of b (Eq. 1.7) according to the V:SA ratio for cells of the corresponding predicted radius (153):

$$b' = b \left[\frac{V/SA_{\text{fossil}}}{V/SA_{\text{modern}}} \right] \quad (\text{Eq. 1.7})$$

This approach and the Method 3 strategy (below) both start with the standard definition of b and calculate a multiplier to account for changes in algal community properties. As such, Eq. 1.7 assumes that $[C_{\text{cell}}]$ and P_C remain constant so that past changes in V/SA capture changes in carbon demand and diffusive supply solely due to cell geometry.

1.2.3. Method 3- size and growth rate corrections

Modifications to b also have been adapted to account for estimated changes in growth rate (cf. 149, 154, 155). These studies assume that changing physiological forms also indicate changes in cell-specific growth rates, with growth rate inferred from changes in paleo-productivity or nutrient proxies (149, 156). Alternatively, estimates of past phosphate concentrations are used to calculate a variable b parameter with the relationship shown in Figure S1 (cf. 140, 155). The b value is adjusted for changes in growth rate similarly to cell size:

$$b' = b \left[\frac{\mu_{i,\text{fossil}}}{\mu_{i,\text{modern}}} \right] \quad (\text{Eq. 1.8})$$

More recently, Zhang et al. (41) developed an approach that combines the geometric correction (Eq. 1.7) with the principles of the growth-rate correction (Eq. 1.8). This approach, here called Method 3, uses the cell size both to adjust for $V:SA$ (diffusion dependence on geometry), and also to directly estimate the growth rate. The components of b that represent the term $[CO_{2(aq)}]\tau$ come from the Rau et al. (145) model and are symbolized as the $CO_{2(aq)}$ uptake rate per unit cell surface area (Q_S), the temperature-dependent $CO_{2(aq)}$ diffusivity (D_T), the cell radius (r), reacto-diffusive length (r_k , the term r/r_k accounts for the relative contribution to the CO_2 flux by extracellular spontaneous conversion of HCO_3^- to CO_2), and permeability (P_C):

$$b = (\varepsilon_f - \varepsilon_t) Q_S \left(\frac{r}{D_T \left(1 + \frac{r}{r_k} \right)} + \frac{1}{P_C} \right) \quad (\text{Eq. 1.9})$$

The empirical relationship between coccolithophore cell volume (V) and instantaneous growth rate (μ_i) (Figure S3) was established using the data from 89 nutrient- and/or light-limited chemostat and semi-continuous diluted batch culture experiments as compiled by Aloisi (157). Cell size, surface area and volume are estimated by measuring the coccolith length, as above (Figure S2). The cellular carbon content (POC/cell) is estimated from cell volume and an empirical relationship of POC to cell volume (Eq. 3 of 41):

$$POC \text{ (fmol C per cell)} = 14.6 * V(\mu\text{m}^3) \quad (\text{Eq. 1.10})$$

The growth rate vs. size relationship (Figure S3, 41) yields μ_i , which is then multiplied by POC and divided by the cell surface area to determine Q_S . The membrane permeability (P_C) was calculated from Pleistocene alkenone-producers ($5.09 \pm 0.16 \times 10^{-5} \text{ m s}^{-1}$) using ice core CO_2 and ε_p data from Pleistocene sediment samples at two sites, based on a boot-strap resampling technique (41). This value for P_C is broadly consistent with laboratory estimates of the permeability of *E. huxleyi* (158).

1.2.4. Method 4 – empirical relationships

Finally, two recent studies have taken an empirical approach, bypassing the Rau et al. (145) approach to defining the sub-components of τ (Eq. 1.4; i.e., the underlying terms of b), thereby

allowing for the presence of non-diffusive or other modes of carbon uptake (including bicarbonate) and CCMs. Using data for *E. huxleyi* and *G. oceanica* in cultures, both Stoll et al. (40) and Phelps et al. (39) found a different sensitivity of ϵ_p to changes in $[CO_{2(aq)}]$ when compared to any version of the purely diffusive model (Methods 1-3). Rae et al. (34) used this new approach to produce a revised paleo- CO_2 record. They first calculate CO_2 anomalies over the Neogene, and then referenced these anomalies to samples from the late Pleistocene, where paleo- CO_2 is known from ice core measurements. In this approach, relative changes in $[CO_{2(aq)}]$ are calculated using the slope (m) of the statistical relationship between $\ln[CO_{2(aq)}]$ and ϵ_p , and the relative changes are anchored with Quaternary sediment samples from the same site where atmospheric CO_2 from ice-core records is known. For each Quaternary-aged sample, an offset value ($I_{sample,Quaternary}$) is calculated:

$$I_{sample,Quaternary} = \epsilon_p - m * \ln([CO_2]_{aq}) \quad (\text{Eq. 1.11})$$

where m equals 2.66 ± 0.42 (± 1 -sigma, 40). The mean of these offset values for each site is then used as the Quaternary anchor ($I_{Quaternary}$) for that site. The aqueous CO_2 concentration is then calculated from ϵ_p and Eq. 1.11, substituting the mean Quaternary intercept and slope to find $[CO_{2(aq)}]$. This approach requires Quaternary samples that overlap the ice-core record and is thus limited to a few sites in the dataset. [Return to Error! Reference source not found.](#)[Error! Reference source not found.](#) **Table S2.**

1.2.5. Remaining challenges for understanding the systematics of algal carbon isotopes

The above approaches primarily focus on improving how relative cellular carbon demand (τ , and by extension, b) is estimated. As such, they presume (i) that the diffusive model is correct and complete, and (ii) that the isotope fractionation associated with carbon fixation (ϵ_f , i.e., the value inferred to result from RuBisCO) is well understood and can be set as a constant. However, recent advances in understanding algal physiology are challenging both premises (see following section), and new factors soon may be incorporated into further revisions of the algal paleobarometry model. These additional considerations are summarized briefly here, because Method 4 utilizes aspects of these additional physiological factors such as irradiance.

The C isotope effect of RuBisCO. Isotopic fractionation during algal carbon fixation, ϵ_f ($\approx 25\%$, 121, 148), originally was thought to be equivalent to the fractionation by RuBisCO, $\epsilon_{RuBisCO}$, as is observed in land plants ($\approx 29\%$, 159, 160). However, experiments demonstrate that Form ID RuBisCO of modern marine phytoplankton has a significantly smaller value of $\epsilon_{RuBisCO}$ ($\approx 11\%$ in the coccolithophore *E. huxleyi* and $\approx 18\%$ in the diatom *Skeletonema costatum*, 131, 132). This finding is particularly problematic for alkenone paleobarometry, because it would set a maximum value of $\approx 11\%$ for alkenone-derived ϵ_p (Eq. 1.2), despite observations of much larger values (20-24%) in the early and mid-Cenozoic portions of the existing ϵ_p dataset. Values of ϵ_p greater than $\epsilon_{RuBisCO}$ are not permitted by the existing diffusive-supply model framework. The implication is that additional fractionation processes are required to explain high values of ϵ_p , and ϵ_f cannot simply be presumed to equal $\epsilon_{RuBisCO}$ (161).

Irradiance. The effects of varying the photosynthetic irradiance provide clues about a potential source of this additional isotopic fractionation. Laboratory experiments (e.g., 135) and

environmental data (summarized in 152) show that irradiance influences ϵ_p beyond simply the increase in growth rate enabled by higher light levels. In laboratory experiments across several different algal groups, high and continuous (24 hour) irradiance appears necessary to generate large values of ϵ_p (39, 40) but to date, the specific conditions that yield high ϵ_p values in the sedimentary record remain unknown despite their apparently common occurrence during the Eocene and Oligocene.

Carbon-concentrating mechanisms (CCMs). A further unanswered question is the role of carbon-concentrating mechanisms (CCMs) in altering both carbon acquisition and CO₂ concentration at the site of fixation (e.g., 162). CCMs can mimic a diffusive CO₂ source, in which case they can be treated as “diffusive-like”. Recently, Badger (107) observed that CO₂ reconstructed from algal ϵ_p values during Pleistocene glacial cycles was systematically in error only at sites where the aqueous CO₂ concentration was < 7 $\mu\text{mol L}^{-1}$. This observation could suggest that CCMs affect ϵ_p at low CO₂ levels, but that diffusion dominates at higher CO₂ levels, i.e., during the Cenozoic until the Plio-Pleistocene (107). Alternatively, from analysis of laboratory cultures, Stoll et al. (40), Wilkes and Pearson (161), and Phelps et al. (39) suggest CCMs are ubiquitously present and functional, but that they scale with a curvilinear relationship between ϵ_p and $1/[\text{CO}_{2(\text{aq})}]$ or τ (39, 162). [Return to Error! Reference source not found.](#)[Error! Reference source not found.](#) **Table S2.**

1.3. Criteria for vetting phytoplankton proxy records

The data compiled for this study and database come from over 30 years of published research, with varied approaches to constraining the necessary biological, geochemical, and environmental parameters needed to reconstruct past atmospheric CO₂ (41, 108, 118, 126, 127, 138, 140, 141, 149-151, 154-156, 163-172). These data were classified into three categories based upon the data completeness and several other criteria. 'Category 1' data are CO₂ estimates of high quality whose sources of uncertainty are fully developed. 'Category 2' data encompass estimates of high quality, but their sources of uncertainty are not yet fully constrained. 'Category 3' estimates are either superseded by newer evaluations of the same proxy data or are considered unreliable due to a variety of factors such as incomplete or outdated sample preparation and/or not fully quantifiable uncertainty estimation. The following criteria were used to categorize each phytoplankton data point in each study:

Category 1 – Fully quantified paleo-CO₂ estimates

- A. All data needed to calculate paleo-CO₂ with modern methods are reported. We required the following data to be reported (or reporting of variables needed to calculate them): algal biomass $\delta^{13}\text{C}$ values, $\delta^{13}\text{C}$ values of aqueous CO₂ or DIC, and sea surface temperature (SST). Some additional variables are only needed for particular methods of calculating surface ocean PCO₂: $[\text{PO}_4^{3-}]$ and coccolith length (Method 2), coccolith length (Method 3), and Pleistocene samples from the same site for Quaternary anchoring (Method 4). If multiple values for a variable (e.g., SST from U^K₃₇ and TEX₈₆) were reported, we used the original publication's choice of values, or averages of where the selection was ambiguous in the original publication (explained in the “notes” columns in data spreadsheets).
- B. Known sources of error have been quantified and/or sensitivity of the paleo-CO₂ estimate to those sources is small.

Category 2 – Incompletely quantified paleo-CO₂ estimates

- A. Samples include all of the data needed to quantify paleo-CO₂ but the aqueous CO₂ concentration falls outside the range used in calibrating empirical factors used in the estimation of paleo-CO₂. In Method 2, the range is from the minimum and maximum [CO₂]_{aq} in the *b*-[PO₄²⁻] calibration dataset. In Method 4, the range is from the minimum and maximum [CO₂]_{aq} values in the laboratory culture experiments that form the calibration dataset.
- B. Samples/records where the organisms contributing to the algal carbon δ¹³C value are unknown. This category includes samples where the δ¹³C of algal organic matter is determined from biomarkers that lack taxonomic specificity (such as phytol and phytane).

Category 3 – Not used to estimate paleo-CO₂

- A. Samples that are superseded by newer studies where additional or better information was added. Parent samples are superseded by the child samples and not included, but their citation is noted.
- B. Samples where measurements of particular input variables in the published dataset were subsequently shown to be inaccurate (and could not be corrected). An example of exclusion for inaccurate values is the recognition that temperature estimates from δ¹⁸O values of diagenetically altered foraminifera were systematically too low (141).
- C. Datasets where data essential for re-calculating paleo-CO₂ were missing and could not be obtained from the authors.
- D. Samples are from oceanic upwelling regions that are far out of equilibrium with atmospheric *p*CO₂ and thus cannot provide estimates for atmospheric CO₂. This excluded the data of Mejía et al. (138), the only diatom-based paleo-CO₂ reconstruction in the database, plus several other alkenone-based studies. These samples are still included in the database as they could be used to examine changes in upwelling or other processes that lead to air-sea disequilibrium. However, they are not used in the reconstruction of atmospheric CO₂.
- E. Samples where paleo-CO₂ is calculated using a method that is no longer considered reliable for a particular proxy. For example, Method 1 does not use any correction for cell size – a correction considered essential for the alkenone-based paleo-CO₂ estimates. Therefore, all paleo-CO₂ estimates calculated from alkenone δ¹³C values using Method 1 are considered Category 3 data.

In a handful of instances, where data were reported graphically but not in data tables, we used data visualization software (<https://automeris.io/WebPlotDigitizer/>) to extract the underlying data from the figure. This is documented in the database. Uncertainties on data estimation using this digitization approach are much smaller than measurement and proxy errors and we consider it to be negligible. [Return to Error! Reference source not found.](#)[Error! Reference source not found.](#) **Table S2.**

1.4. Calculational methods

We applied four published methods to reconstruct paleo-CO₂ for the data compilation:

- Method 1 – diffusive framework (b) without size correction. Only used for phytane/phytol dataset.
- Method 2 – diffusive framework (b) with correction for cell size based on coccolith morphometry (38);
- Method 3 – diffusive framework with b calculated using permeability determined from Pleistocene sediment samples, cell size based upon coccolith morphometry and growth rate based upon a statistical relationship between cell size and growth rate (34, 41);
- Method 4 – statistical relationship of ϵ_p to $\ln([\text{CO}_{2(\text{aq})}])$ in culture (40) with anchoring to Quaternary samples with known $[\text{CO}_{2(\text{aq})}]$ (34).

As many methods as allowed by the data were applied to each sample. For example, if a site lacked Quaternary samples for anchoring, then no paleo-CO₂ estimates could be determined for that site with Method 4 (although other Methods could be applied).

We begin by describing the calculation of variables common to all method: sea-surface temperature (SST), sea-surface salinity (SSS), $\delta^{13}\text{C}$ of aqueous CO₂, $\delta^{13}\text{C}$ of cellular biomass, and ϵ_p . Following, we describe the calculation of surface ocean PCO₂ with each method, followed by calculation of a weighted mean estimate from all methods. For each of the methods, uncertainties in CO₂ values were determined by Monte Carlo resampling of input parameters. The resulting distribution of PCO₂ values reflects the uncertainties in the input parameters and the 95% confidence interval was calculated from this distribution.

Sea Surface Temperature. The datasets included in the compilation use SST estimates from the proportion of di-unsaturated to tri-unsaturated C₃₇ alkenones (U^k₃₇), the ratio of Mg to Ca in foraminifera shells (Mg/Ca), and the ratio of internal cyclization of glycerol dialkyl glycerol tetraether (GDGT) membrane lipids (TEX₈₆). The published temperature values in the original studies are used for these proxies because many datasets lacked information (such as raw proxy values) needed for re-calculation. This approach may lead to some increase in the scatter of paleo-CO₂ estimates, and thus recalculation of SSTs would be a natural target for future work.

SST values calculated from U^k₃₇, foraminiferal Mg/Ca ratios, and TEX₈₆ values were assigned uncertainties of ± 1.5 , ± 1.8 , and $\pm 5^\circ\text{C}$, respectively ($\pm 1\sigma$, normally distributed), based upon uncertainties in published calibrations (173-175). Analytical uncertainties are typically smaller and are not included here. Where multiple SST estimates are reported (e.g., both U^k₃₇ and TEX₈₆), the average of the two is calculated and the uncertainty is determined by the quadrature sum of the individual uncertainties.

Salinity. Salinity has a very minor influence on the solubility of CO₂ in seawater (Henry's constant; K_H) and the resulting $[\text{CO}_{2(\text{aq})}]$ calculated from algal ϵ_p . We apply a single salinity value of $35 \pm 2\text{‰}$ (1-sigma normal distribution) to all samples. This uncertainty captures variations from changes in the ocean's water balance (principally from ice volume) as well as probable long-term variations due to changes in solute balance.

Photosynthetic carbon isotope fractionation, ϵ_p . Isotopic values for algal biomass and aqueous CO₂ are required (Eq. 1.1) and are determined from $\delta^{13}\text{C}$ values of biomarkers and foraminifera calcite, respectively, as described below.

$\delta^{13}\text{C}_{\text{CO}_2(\text{aq})}$ values. The value of $\delta^{13}\text{C}_{\text{CO}_2(\text{aq})}$ is determined from surface dwelling planktic foraminiferal $\delta^{13}\text{C}$ values, if available. A few studies report DIC $\delta^{13}\text{C}_{\text{DIC}}$ values calculated from $\delta^{13}\text{C}_{\text{foram}}$, which we use as is. We use each publication's approach to deal with vital effects. The corrections are generally small and their uncertainty does not significantly affect the final paleo-CO₂ estimates.

$\delta^{13}\text{C}_{\text{CO}_2(\text{aq})}$ from $\delta^{13}\text{C}_{\text{DIC}}$. Where $\delta^{13}\text{C}_{\text{DIC}}$ is reported by the original authors, we use the relationship of Rau et al. (145) (following from 119, 176) to calculate $\delta^{13}\text{C}_{\text{CO}_2(\text{aq})}$. Where reported, the 1-sigma uncertainty (normal distribution) in $\delta^{13}\text{C}_{\text{DIC}}$ is used for error propagation, otherwise an average value of $\pm 0.3\%$ (1-sigma, normal) is applied.

$\delta^{13}\text{C}_{\text{CO}_2(\text{aq})}$ from $\delta^{13}\text{C}_{\text{foram}}$. Where $\delta^{13}\text{C}_{\text{foram}}$ is reported, we calculate $\delta^{13}\text{C}_{\text{CO}_2(\text{aq})}$ values using the relationship between $\delta^{13}\text{C}_{\text{CO}_2(\text{g})}$ and $\delta^{13}\text{C}_{\text{CaCO}_3}$ of Romanek et al. (177) combined with the relationship between CO_{2(g)} and CO_{2(aq)} determined by Mook et al. (176). Uncertainty in the $\delta^{13}\text{C}$ value of $\delta^{13}\text{C}_{\text{CO}_2(\text{aq})}$ from planktic foraminifera is propagated from the measurement uncertainty of foraminifera $\delta^{13}\text{C}$ values (normally distributed standard error of the mean) and uncertainty in the SST (described above). In studies where a uniform uncertainty is reported, a standard deviation is calculated by assuming this uniform distribution is equivalent to $\pm 3\sigma$. Samples with missing uncertainties or uncertainties that are in error (zero, negative values) are assigned the median of the uncertainties from the full dataset. For all data, the standard error of the mean is calculated from the number of observations (if reported), or assuming $n=1$ if the number is missing.

Several studies rely on $\delta^{13}\text{C}$ values of benthic foraminifera to estimate surface ocean $\delta^{13}\text{C}$ values. This approach applies a $\delta^{13}\text{C}$ offset that is meant to correct for the difference between surface and deep ocean $\delta^{13}\text{C}$ of DIC (largely due to the biological pump). We use the $\delta^{13}\text{C}$ values with the offset as applied in the original publication.

$\delta^{13}\text{C}_{\text{biomass}}$ values. Algal biomass $\delta^{13}\text{C}$ values are determined from measurement of $\delta^{13}\text{C}$ values of sedimentary algal biomarkers (alkenones, phytane/phytol) or fractions of cellular biomass (c.f. organic carbon in diatom frustules). Algal biomass is calculated using empirically determined fractionation factors between biomarker and cellular biomass. Fractionation factors are calculated from measurements of biomass and biomarker $\delta^{13}\text{C}$ values in laboratory culture:

$$\epsilon_{\text{biomass/biomarker}} = \left(\frac{\delta^{13}\text{C}_{\text{biomass}} + 1000}{\delta^{13}\text{C}_{\text{biomarker}} + 1000} - 1 \right) \cdot 1000 \quad (\text{Eq. 1.12})$$

The mean values and uncertainty for $\epsilon_{\text{biomass/biomarker}}$ are listed in **Table S3**. Uncertainties in $\delta^{13}\text{C}$ biomass values reflect the propagated measurement uncertainty of biomarker $\delta^{13}\text{C}$ values (± 1 standard error of the mean) and the uncertainty in $\epsilon_{\text{biomass/biomarker}}$. Biomarker $\delta^{13}\text{C}$ uncertainty is based upon the standard deviation if reported. If no uncertainty is reported or is entered as zero, then the median of the reported standard deviation across all samples is applied. The standard error of the mean is calculated for all samples using the number of replicates (if

reported) or assuming $n=2$ (as is common for compound-specific isotope analysis). In all cases the normally distributed standard error of the mean is used for error propagation.

We assume that the standard deviation of $\varepsilon_{\text{biomass/biomarker}}$ reflects real differences due to variation in species and growth conditions, and captures differences likely encountered in the modern and ancient oceans. However, we do not include the uncertainty of $\varepsilon_{\text{biomass/biomarker}}$ in the error propagations because this uncertainty is already incorporated in the empirically determined b value (Methods 1 and 2), the calibration of permeability from Pleistocene sediments (Method 3), and the determination of the Quaternary anchor (Method 4).

1.4.1. Method 1 – diffusive framework, no size corrections

The procedure for Method 1 is:

1. calculate $\delta^{13}\text{C}_{\text{biomass}}$ from measurements of $\delta^{13}\text{C}_{\text{biomarker}}$ and Eq. 1.12.
2. calculate $\delta^{13}\text{C}_{\text{CO}_2(\text{aq})}$ from planktic foraminifera or DIC $\delta^{13}\text{C}$. The proxy reconstruction of SST is used for the temperature dependence of these equations.
3. calculate ε_p (Eq. 1.1) from $\delta^{13}\text{C}_{\text{biomass}}$ and $\delta^{13}\text{C}_{\text{CO}_2(\text{aq})}$
4. determine a b value from $[\text{PO}_4^{3-}]$ using Eq. 1.13 below
5. calculate $[\text{CO}_2(\text{aq})]$ from ε_p , ε_f , and b with Eq. 1.2
6. calculate PCO_2 from $[\text{CO}_2(\text{aq})]$ and the temperature-adjusted Henry's law constant.

We chose a uniform approach for calculating uncertainty to facilitate meaningful comparisons between samples. The uncertainty of the calculated PCO_2 was determined by 10,000 Monte Carlo simulations where each input parameter is resampled for every sample in the database 10,000 times. This assumes uncorrelated uncertainties in the input parameters. Parameters like SST that are used several times in the calculation of PCO_2 from a sample are only resampled once per Monte Carlo realization.

The b value is correlated to $[\text{PO}_4^{3-}]$ in the modern ocean, and this relationship is used to estimate a b value for each sampling location and its associated uncertainty. In this method the relationship of b to $[\text{PO}_4^{3-}]$ is assumed to remain unchanged in the past. The published $[\text{PO}_4^{3-}]$ value from each study is used in the recalculation and applied as a constant value for each site in a publication. We apply a uniformly distributed uncertainty equal to $\pm 20\%$ of the published $[\text{PO}_4^{3-}]$ value from the original study. The b values used for this relationship are recalculated with Eq. 1.3 using an ε_f value of 26.5‰. We use the compiled calibration data of Hernández-Almeida et al. (144) and a linear least-squares regression to relate b and $[\text{PO}_4^{3-}]$ to calculate b values (Fig. S1):

$$b = 129.621[\text{PO}_4^{3-}] + 93.043 \quad (\text{Eq. 1.13})$$

We calculate uncertainty in the calculated b values from both the uncertainty in $[\text{PO}_4^{3-}]$ values, the uncertainty in the fitted slope and intercept of the b - $[\text{PO}_4^{3-}]$, and the residuals from this fit. Uncertainty in the $[\text{PO}_4^{3-}]$ value has traditionally been the primary uncertainty propagated into paleo- CO_2 estimates, with some studies also including uncertainty in the fitted slope and intercept of the b - $[\text{PO}_4^{3-}]$ relationship. However, the residuals in the fit are substantial and reflect

additional effects not captured in the b -[PO₄³⁻] relationship. We therefore include the residual uncertainties as a more complete measure of the uncertainty in the b value (Fig. S1). At low [PO₄³⁻], the uncertainty in the regression prediction can (rarely) return values for b that are zero or negative. In such a case, additional Monte-Carlo draws are done until no zero or negative b values are present.

All samples using phytane or phytol to determine biomass $\delta^{13}\text{C}$ are assigned a b value at the midpoint of the range in the calibration Tables S2 and S3 of Witkowski et al. (127). The uncertainty is applied as a uniform distribution with values that span the range of b values in the calibration tables ($b = 191 \pm 89$, uniform distribution). This value and distribution are chosen to capture the range of values present due to the variety of sites in these datasets. [Return to Error! Reference source not found.](#)

1.4.2. Method 2 – diffusive framework with size correction

The calculation of PCO_2 and uncertainty using Method 2 is identical to Method 1 except that a correction to the b term is applied for changes in cell size:

1. calculate steps 1-4 as described in Method 1 (above)
2. calculate a mean cell radius using coccolith length and Eq. 1.14 (described below)
3. calculate a b' term corrected for changes in V/S using Eq. 1.7
4. calculate [CO_{2(aq)}] from ϵ_p , ϵ_f , and b' with Eq. 1.2
5. calculate PCO_2 from [CO_{2(aq)}] and the temperature-adjusted Henry's law constant.

Coccolith length is taken as reported in individual studies, with reported uncertainties used to determine the ± 1 -sigma range of a normal distribution. Uncertainties reported as both a positive and negative value are averaged to give a single, normally distributed, uncertainty value. Samples with a coccolith length but a missing or zero uncertainty value are assigned the median of the distribution of all uncertainties from samples with measured values, and a uniform distribution is used for error propagation. Alkenone samples that do not have a measured coccolith length are assigned a size that is the midpoint of the range of sizes in the distribution of all samples with measured values. These samples are assigned a uniformly distributed uncertainty that spans the range of coccolith lengths found in all samples with measured values.

Cell radius is calculated from coccolith length using the relationship between radius (r) and length (L) measured on discrete individual coccospheres found in Cenozoic sediments (Fig. S2) (38). The uncertainty in coccolith length, and the parameter uncertainty in the regression are used to propagate the error in predicted cell radius. The parameter uncertainty is the appropriate uncertainty, as the residual uncertainty would overestimate the uncertainty in the population of cell radii. At small coccolith length, the uncertainty in the regression prediction can (rarely) return values for the cell radius that are zero or negative. In such a case, additional Monte-Carlo draws are done until no zero or negative cell radii are present. Cell volume, surface area, and the volume/surface area ratio are calculated from the cell radius assuming a spherical cell. Uncertainties in the radii are propagated through these calculations.

In Method 2, Eq. 1.7 is used to calculate a revised b' value that reflects changes in cell size in the past. An important consideration is the modern cell size used to normalize past cell sizes. We follow the original work of Henderiks and Pagani (38) and use a V/SA ratio of 0.9 μm , determined from *E. huxleyi* cultures, to normalize past V/SA ratios and calculate b' values. [Return to Error! Reference source not found.](#)[Error! Reference source not found.](#) **Table S2.**

1.4.3. Method 3 – diffusive framework with cell size and growth-rate

Zhang et al. (41) developed an approach to calculating b that uses cell size to calculate both growth rate and the effects of V/S changes (Eq. 1.9). In this method, b is determined by six parameters, and among those, sensitivity analyses show that b is mostly dependent on growth rates, cell size and membrane permeability to CO_2 .

The detailed procedure to calculate PCO_2 with this method is:

1. calculate steps 1-3 as described in Method 1 (above)
2. calculate a mean cell radius using coccolith length and Eq. 1.14 (as in Method 2)
3. calculate a cell carbon content using Eq. 1.10
4. calculate instantaneous growth rate from cell radius using Figure S3
5. calculate a b value from Eq. 1.9
6. calculate $[\text{CO}_2(\text{aq})]$ from ϵ_p , ϵ_f , and b with Eq. 1.2.
7. calculate PCO_2 from $[\text{CO}_2(\text{aq})]$ and the temperature-adjusted Henry's law constant.

Membrane permeability. The membrane permeability of Pleistocene alkenone-producers is $5.09 \pm 0.16 \times 10^{-5} \text{ m s}^{-1}$, calculated using ice core CO_2 and ϵ_p data at two sites, based on a bootstrap resampling technique (41) (Sec 1.2.2). Uncertainty in the permeability is propagated from a normal distribution with a ± 1 -sigma of $0.16 \times 10^{-5} \text{ m s}^{-1}$.

Cell carbon content and Q_s . The cellular carbon content (POC/cell) is calculated from the cellular volume using Eq. 1.10 (Eq. 3 in 41). The cell volume is derived from measurements of coccolith length and the uncertainty in volume is propagated through the calculation of cellular carbon content.

Growth rate from cell volume. The empirical relationship between coccolithophore cell volume (V) and instantaneous growth rate (μ_i) was established using the data from 89 nutrient- and/or light-limited chemostat and semi-continuous diluted batch culture experiments compiled by Aloisi (157) and calculated by Zhang et al. (41) (Fig. S3). This growth rate is an instantaneous growth rate that accounts for the light/dark photoperiod length and respiration in algal experiments.

Uncertainty in growth rate is from both the uncertainty in the cell volume (as propagated from the lith length), the uncertainty in the fitting parameters of the relationship, and the residuals from this fit (Fig. S3). We include the residual uncertainties as a more complete measure of the overall numerical uncertainty in the growth rate. [Return to Error! Reference source not found.](#)[Error! Reference source not found.](#) **Table S2.**

1.4.4. Method 4 – Statistical framework with Quaternary anchoring

Rae et al. (34) presented paleo-CO₂ estimates recalculated using a statistical relationship between $\ln[\text{CO}_{2(\text{aq})}]$ and ε_p found in laboratory algal cultures (40). The detailed procedure is:

1. calculate steps 1-3 as described in Method 1 (above)
2. for Quaternary-age samples, calculate PCO_2 and $[\text{CO}_{2(\text{aq})}]$ from the ice-core CO₂ record
3. for Quaternary-age samples, use Eq. 1.11 to calculate the mean Quaternary anchor value for each site (described below)
4. For each site, use Eq. 1.11 to calculate $[\text{CO}_{2(\text{aq})}]$ from ε_p and the Quaternary anchor (described below)
5. calculate PCO_2 from $[\text{CO}_{2(\text{aq})}]$ and the temperature-adjusted Henry's law constant.

Calculating PCO_2 and $[\text{CO}_{2(\text{aq})}]$ from the ice-core CO₂ record. The surface ocean PCO_2 at the age of each Quaternary sample is calculated from the ice core CO₂ record (11) by linear interpolation between data points. The $[\text{CO}_{2(\text{aq})}]$ value in equilibrium with this PCO_2 value is then calculated each of these samples using Henry's law and the proxy SST value from each sample. These ice-core-inferred $[\text{CO}_{2(\text{aq})}]$ values are the target for anchoring the relative paleo-CO₂ changes at each site.

Calculating the Quaternary anchor. For each Quaternary-aged sample, an offset value ($I_{\text{sample, Quaternary}}$) is calculated for each sample with Eq. 1.11. The mean of these offset values for each site is then used as the Quaternary anchor ($I_{\text{Quaternary}}$) for that site. The standard error of the mean for the offset is used in the uncertainty analysis.

Calculating $[\text{CO}_{2(\text{aq})}]$ from ε_p and the Quaternary anchor. The aqueous CO₂ concentration is calculated from ε_p , the Quaternary intercept ($I_{\text{Quaternary}}$), and the slope of the statistical relationship between ε_p and $\ln([\text{CO}_{2(\text{aq})}])$ as determined by Stoll et al. (40) using Eq. 1.11. The uncertainty in each parameter is propagated through subsequent calculations, including $m = 2.66 \pm 0.42$ (1-sigma, normal distribution). Note that this approach ignores the effects of cell size, growth rate, and irradiance that were also present in the statistical relationship.

Uncertainty in this approach is calculated from the uncertainty in (m) from the statistical fit between ε_p and $\ln[\text{CO}_{2(\text{aq})}]$ as well as the standard error of the mean of the Quaternary anchor, and the propagated uncertainty in ε_p . [Return to Error! Reference source not found.](#)[Error! Reference source not found.](#) **Table S2.**

1.4.5. Calculation of weighted mean paleo-CO₂ from all Methods

Surface ocean PCO_2 and atmospheric pCO_2 are equal in ocean regions where surface seawater and the atmosphere are in CO₂-equilibrium, and at sea level (with ~1 atm pressure) PCO_2 and pCO_2 are approximately equal to the mole fraction of CO₂ (x_{CO_2}), which is independent of altitude. To prevent any altitude effects, all proxies in this study report x_{CO_2} , which we generally call 'paleo-CO₂'. Consequently, we refer to phytoplankton PCO_2 estimates as paleo-CO₂ and because we have applied up to 4 Methods for each ε_p value, we need to determine a mean paleo-CO₂ value for each sample. To do so, only Category 1 data are used, so not all methods are used for every

sample. For each sample, the mean paleo-CO₂ is the inverse-variance weighted mean. Calculations are done on $\ln(PCO_2)$ values as their uncertainties more closely approximate a normal distribution.

The detailed procedure to calculate paleo-CO₂ with this method is:

1. For each sample, calculate $\ln(PCO_2)$ on Methods with Category 1 estimates. This calculation is done on the central PCO_2 estimate and the Monte-Carlo resampling-derived distribution of PCO_2 values (reflecting the uncertainty in the input parameters).
2. Calculate the variance of $\ln(PCO_2)$ from the Monte-Carlo derived distributions for each Method in each sample.
3. Calculate the inverse-variance-weighted mean $\ln(PCO_2)$ value for each individual Monte-Carlo resampled estimate in each sample. The distribution of these values is the distribution of the new weighted-mean $\ln(PCO_2)$ estimate. This approach reduces the variance from parameters that are independent between the methods, while preserving variance from parameters shared between the methods.
4. Calculate paleo-CO₂ from the distribution of mean $\ln(PCO_2)$ estimates.

This approach assumes that the estimates of PCO_2 by the different methods are independent. Several of the underlying variables are common to all methods (e.g., ϵ_p , SST) which could violate this assumption. However, many of the parameters are unique to each method and thus would make the methods independent of each other. We tested this assumption by examining the correlation between the Monte-Carlo distribution of PCO_2 estimates from different methods in a single sample. These estimates were highly uncorrelated indicating the methods are largely independent and the weighted-mean approach is reasonable. An example of this lack of correlation is shown in Fig. S4. [Return to Error! Reference source not found.](#)[Error! Reference source not found.](#)Table S2.

1.5. Future opportunities

The approaches used here to re-calculate pCO_2 values from algal $\delta^{13}C$ values mostly rely on the assumption of diffusive (or diffusive-like) supply of CO₂ and an ϵ_f value that is assumed to reflect $\epsilon_{RuBisCO}$. However, algal ϵ_p records generated using these models are unable to consistently capture both the late Pleistocene glacial-interglacial paleo-CO₂ changes (107, 150, 151) and the large ϵ_p values of the early Cenozoic. Some modifications appear to be required, and such revisions are nascent and an active area of research (cf. 39-41, 107, 138, 151, 152, 161). Below we outline future research directions that may help address these issues and improve the algal paleo-CO₂ proxy. The cell size – growth rate relationship provides a possible approach to construct b as a variable for every sample used for paleo-CO₂ estimates. Automated systems have been developed to perform regional mapping of the size and weight of coccoliths in natural settings (e.g., 178, 179). In the future, these techniques could be used in the field to better evaluate the potential of using coccolith size as an indicator of haptophyte growth rate and hence b . This should include evaluation of potential changes over time in the relationship of coccolith size to growth rate.

It is critical to replicate and extend the *in vitro* measurements of $\epsilon_{\text{RuBisCO}}$ within algal groups. Measured carbon isotope fractionation in nutrient-limited, light-replete continuous chemostat cultures consistently indicate an effective maximum fractionation of $\sim 25\text{‰}$ for eukaryotic phytoplankton (128, 148, 180). Values approaching 25‰ are also found in Eocene and Oligocene sediments. Confirmation of the Boller et al. (131) *E. huxleyi* result of $\sim 11\text{‰}$, plus experiments on other algal groups, are needed to determine the magnitude of carbon isotope fractionation in algal carbon fixation.

The isotopic consequences of CCMs also remain largely unknown. CCM activity has been shown to increase with carbon limitation (e.g., 40, 181, 182, 183). Such an effect modifies the $[\text{CO}_{2(\text{aq})}]$ - ϵ_p relationship but may not present an insurmountable challenge to the existing proxy calibration if CCM activity is expressed in proportion to $[\text{CO}_{2(\text{aq})}]$. However, CCM activity may also be sensitive to interactions of light and nutrient limitation. For example, Wilkes et al. (161) proposed that a strongly fractionating CCM based on unidirectional hydration of CO_2 becomes active under nutrient-limited growth when photon fluxes exceed the requirement to synthesize biomass. Studies that relate CCM activity and isotopic consequences to $[\text{CO}_{2(\text{aq})}]$, nutrient availability, and irradiance will be essential in order to account for such effects in paleo- CO_2 studies.

Coccolith calcite may be an additional avenue to reconstruct the past physiology of these organisms. The trace element geochemistry of coccoliths may incorporate a record of growth rate (e.g., 184), while their stable isotopic composition ($\delta^{13}\text{C}$ and $\delta^{18}\text{O}$) is impacted by irradiance (e.g., 185). Whether qualitative or quantitative, these properties may yield insights into algal growth or paleo- CO_2 directly (cf. 114).

All of the factors described above are observed in laboratory cultures, the modern ocean, or core top sediments where we can constrain many environmental factors such as nutrient concentration, irradiance, temperature, and $[\text{CO}_{2(\text{aq})}]$. While direct paleo-proxies for nutrients and irradiance generally do not exist, proxies for oceanographic setting such as mixed layer depth and thermocline strength are sometimes available. A promising approach will be to relate these biological factors important for algal ϵ_p values to (paleo)oceanographic settings to improve estimates of past CO_2 levels. This same approach could also be useful to address ecological questions important for phytoplankton $p\text{CO}_2$. For example, better constraints on the depth of phytoplankton production in the past would inform the degree to which the reconstructed $[\text{CO}_{2(\text{aq})}]$ is in equilibrium with the atmosphere (i.e., the near surface versus, e.g., the deep chlorophyll maximum). [Return to Error! Reference source not found.](#)[Error! Reference source not found.](#)**Table S2.**

2. Boron Proxies

2.1. Current understanding of boron proxies and recent advances

The boron isotope and B/Ca proxies, recorded in marine carbonates, are built upon the predictable change in the abundance and isotopic composition of dissolved borate ion in seawater with a change in seawater pH (186). In open-ocean regions where surface waters are in equilibrium with the atmosphere, surface ocean pH closely tracks atmospheric CO_2 . As such,

these regions are targeted for boron-based paleo-CO₂ reconstructions, by measuring B/Ca or (more commonly) $\delta^{11}\text{B}$ in fossil shells of surface ocean dwelling planktic foraminifera from open ocean sediment cores. Since the common basis of these proxies was first proposed by Vengosh et al. (187) and Hemming and Hanson (188), both proxies have been subject to considerable testing and ground-truthing, and have evolved and developed considerably over the last couple of decades.

Of the two boron-based proxies, the future of planktic B/Ca as a proxy for CO₂ is less secure. The dependence of planktic foraminiferal B/Ca on seawater pH has been repeatedly demonstrated in culture (189-194), but a number of secondary factors has also been shown to affect B/Ca. These include salinity (189, 195), dissolved inorganic carbon concentrations, or [DIC] (189, 194), light intensity (196), nutrient concentrations (195), surface ocean saturation state (197), or calcification intensity (198). Of these secondary factors, the apparent dual dependency of the B/Ca proxy on pH and [DIC] could have great potential when paired with pH data from boron isotopes to solve the whole carbonate system and derive surface ocean paleo-CO₂, provided error propagation is comprehensive (199, 200). While this is a powerful approach, and the coherent changes often seen between $\delta^{11}\text{B}$ and B/Ca in deep time studies (200-203) are consistent with a predominant carbonate-system control on B/Ca as seen in culture, some lingering uncertainties remain. Specifically, until the sensitivity of B/Ca to the other secondary factors listed above can be falsified or corrected for, this will remain a background structural uncertainty to the application of B/Ca in planktic foraminifera shells to trace paleo-CO₂.

Contrastingly, since the first studies exploring the potential of the boron isotope proxy for reconstructing past atmospheric CO₂ (204, 205), subsequent culture and open-ocean studies have repeatedly shown that planktic foraminiferal $\delta^{11}\text{B}$ is predominantly a function of pH and the well-understood dependency of pK^*_B on temperature, salinity and pressure (186, 206). Notwithstanding refinements in the underlying physicochemical understanding of the proxy (207, 208), the basic understanding of the proxy has endured largely unchanged since the early studies of Hemming and Hanson (188) and Sanyal et al. (204). Because the $\delta^{11}\text{B}$ recorded in marine carbonates closely relates to the $\delta^{11}\text{B}$ of dissolved borate in seawater, pH can be calculated via $\delta^{11}\text{B}_{\text{borate}}$ from $\delta^{11}\text{B}_{\text{CaCO}_3}$ as follows:

$$\delta^{11}\text{B}_{\text{borate}} = (\delta^{11}\text{B}_{\text{CaCO}_3} - c)/m \quad (\text{Eq. 2.1})$$

where c is the intercept and m the slope of the regression (191).

$$\text{pH} = \text{pK}^*_\text{B} - \log \left(- (\delta^{11}\text{B}_{\text{sw}} - \delta^{11}\text{B}_{\text{borate}}) / (\delta^{11}\text{B}_{\text{sw}} - \alpha_{\text{B}_3\text{-B}_4} * (\delta^{11}\text{B}_{\text{borate}}) - \varepsilon_{\text{B}_3\text{-B}_4}) \right) \quad (\text{Eq. 2.2})$$

where pK^*_B is the dissociation constant of boric acid in seawater (186, 206), $\delta^{11}\text{B}_{\text{sw}}$ is the boron isotopic composition of seawater, $\alpha_{\text{B}_3\text{-B}_4}$ is the aqueous boron isotope fractionation factor (207, 208) and $\varepsilon_{\text{B}_3\text{-B}_4}$ the corresponding aqueous boron isotope fractionation. Because carbon speciation in seawater is coupled to equilibrium reactions, CO₂ can then be calculated from pH when paired with a second parameter of the marine carbonate system (e.g., alkalinity, dissolved inorganic carbon, Ω_{calcite}), in addition to estimates of temperature, salinity and pressure. For a review of how this is done in practice, see Rae (31) and Hönisch et al. (30). It is worth noting that *relative* change in CO₂ climate forcing can often be effectively reconstructed using boron isotopes even in the absence of these other constraints on seawater chemistry (209).

In recent years, the main advances in our understanding have come largely in the realm of understanding foraminiferal vital effects (both in extant and extinct species), in more fully propagating uncertainty, and in the application of seawater dissociation constants adjusted for seawater major ion variability on multi-million-year timescales (210, 211). In terms of vital effects, more and more measurements of open-ocean Holocene foraminifera have revealed coherent patterns across species, with surface-dwelling symbiont-bearing foraminifera recording higher pH than ambient seawater (e.g., 191, 212, 213, 214), and symbiont-barren and/or deeper-dwelling species recording lower pH than their surrounding seawater (e.g., 212, 215-221). Thus far, these findings have largely been in-keeping with existing models of vital effects being driven by chemical alteration in the foraminiferal microenvironment (218, 222, 223). [Return to Error! Reference source not found.](#)[Error! Reference source not found.](#)**Table S2.**

2.1.1. Uncertainties and error propagation

Uncertainty propagation has greatly been improved since the earliest boron isotope-based pH and paleo-CO₂ reconstructions that only considered the analytical uncertainty of the boron isotope analysis (e.g., 204, 205). Following Hönisch & Hemming (224), the additional uncertainties of the second parameter of the carbonate system, temperature, salinity and pressure are now commonly accounted for. More recently, and partly by necessity when approaching deeper time questions, studies have begun to quantify uncertainties inherent in species-specific calibrations, uncertainties on the $\delta^{11}\text{B}$ of bulk seawater and variable seawater elemental composition through time, to name a few (e.g., 60, 68, 225-227). Often, these error propagations use Monte Carlo approaches, which can be beneficial in yielding probability density functions of paleo-CO₂ that can be incorporated into future time series analysis, and can often better cope with linked uncertainties that apply at multiple stages on the path to a paleo-CO₂ estimate (e.g., major ion chemistry effects on accessory Mg/Ca temperatures, equilibrium constants, and carbonate saturation). [Return to Error! Reference source not found.](#)[Error! Reference source not found.](#)**Table S2.**

2.2. Criteria for vetting boron proxy records and data revisions

The paleo-CO₂ archive includes only boron proxy records that have been collected in the open ocean and outside of upwelling areas (56, 60, 68, 156, 164, 191, 199, 205, 212, 215, 224-226, 228-240). Several published studies have recalculated earlier data with the most recent proxy understanding and error propagation routines (e.g., 225, 230, 231, 239), so that much of the vetting process focused on identifying superseded data and eliminating duplicate representation (for details, see vetting information in individual product proxy sheets).

Only three boron proxy studies have been placed in Category 3. These include Tripathi et al. (228), who used the B/Ca proxy and their CO₂ estimates have been found to be driven mostly by temperature, while the actual B/Ca data play only a very minor role in the CO₂ these authors reconstructed (241). Stap et al. (240) did not measure the boron concentrations of their samples and their large data variability suggests their signal to noise ratio was too small. In addition, the pioneering work of Pearson and Palmer (205) over the Cenozoic is subject to uncertainties stemming from the inclusion of some mixed species foraminifer samples, variable size fractions, unverifiable efficacy of sample cleaning, and laboratory-specific analytical offsets. Anagnostou et al. (212) attempted to correct the data for these technique-specific offsets but cautioned that

variable size fractions and possibly other factors might undermine this correction. Given that better-constrained and more highly-resolved data are now available, we err on the side of caution and exclude the data of Pearson & Palmer (205) from the vetted compilation.

The B/Ca study of Haynes & Hönisch (199) reports paleo-CO₂ estimates for the PETM, but the CO₂ estimates require two uses of pH estimates from boron isotopes, once to remove the pH (or better: the borate ion concentration) effect from the B/Ca signal, and then again to pair the DIC signal with pH as the second parameter of the carbonate system. Because of this, the CO₂ estimates are not strictly independent, and have been excluded from Category 1. However, given the growing uncertainty of CO₂ reconstructions further back in time, and the entirely proxy-based calculation, we report the data in Category 2.

Finally, Anagnostou et al. (60, 212), Sosdian et al. (239), Henehan et al. (68) and Guillermic et al. (242) provide multiple scenarios for CO₂ depending on underlying assumptions made. To eliminate duplicate representation of the data, the vetted product includes only one of those options, which has been selected in consultation with the original authors as the most likely best estimate. For example, Sosdian et al. (239) explored a range of options for the Mg and Ca elemental composition of seawater, the depth of the CCD and $\delta^{11}\text{B}_{\text{sw}}$. Of these, the best estimates used the elemental composition from fluid inclusions (243, 244), the CCD after Pälke et al. (245), and $\delta^{11}\text{B}_{\text{sw}}$ after Greenop et al. (246). For details on other boron proxy studies, please review the vetting information in individual product proxy sheets. [Return to Error! Reference source not found.](#)[Error! Reference source not found.](#) **Table S2.**

2.3. Future directions

Although great progress has been made in grounding and expanding the boron isotope proxy in particular in the past decades, several key areas remain where there is scope to improve the precision and reliability of past CO₂ reconstructions. Broadly speaking, these fall into four categories: 1) detection and quantification of vital effects in extinct foraminifera; 2) better and independent reconstructions of past $\delta^{11}\text{B}_{\text{sw}}$; 3) improved reconstruction of the second parameter of the carbonate system, and 4) analytical advances.

As previously discussed, vital effects in modern planktic foraminifera are increasingly widely documented, with all modern species displaying some offset in $\delta^{11}\text{B}$ from the $\delta^{11}\text{B}$ of ambient borate ion. When applying the boron isotope proxy as far back as the first appearance of *T. trilobus* (~23 Ma, 247), empirical calibrations based on extant species (e.g., 191, 219, 223, 225, 235, 239) can be used. Earlier in the Cenozoic, however, the question of whether and how to apply modern-species calibrations to extinct species adds a structural uncertainty to paleo-CO₂ reconstructions, and has led to subtly different approaches being taken in earlier Cenozoic studies published to date. Anagnostou et al. (212) found that applying modern analogue vital effects to different tropical Eocene taxa according to their habitat depth and strength of photosymbiosis (as discerned from species-specific trends in $\delta^{18}\text{O}$ and $\delta^{13}\text{C}$ with shell size) resulted in likely unrealistic reconstructions of the water column pH profile. Because this study found certain shallow-dwelling photosymbiotic Eocene taxa not to display resolvable increases in $\delta^{11}\text{B}$ with size (as mixed-layer photosymbiotic species do today, 191, 213), the authors suggested that boron isotope vital effects in the Eocene may have been smaller than observed in modern species. In contrast, Henehan et al. (68) found that applying modern analogue vital

effects to middle Eocene planktic foraminifera successfully reconciled otherwise divergent trends in reconstructed pH from different species and locations, lending tentative support to this approach. Similarly, using modern vital effect calibrations for different species results in a more consistent magnitude of surface ocean pH change across the Paleocene-Eocene Thermal Maximum (202). Collectively, these deep-time studies illustrate the importance of careful interrogation of potential taxon-specific vital effects in extinct foraminifera. Fortunately, and in practice, the difference between Eocene paleo-CO₂ calculated from tropical mixed-layer taxa using a modern *T. sacculifer/trilobus* calibration is typically within uncertainty of assuming no vital effects at all (60, 212). That said, the fact that symbiont-bearing calibrations typically have a lower sensitivity of $\delta^{11}\text{B}$ to pH means that this decision also affects the magnitude of pH and paleo-CO₂ change reconstructed over a given interval or excursion (e.g., 30, 201, 202).

To resolve issues surrounding vital effects going forward, there is a clear need to mechanistically understand vital effects in foraminiferal $\delta^{11}\text{B}$ and place this in a numerical framework that allows prediction of $\delta^{11}\text{B}$ vital effects in extinct species given a number of measurable parameters (e.g., foraminiferal test volume, presence/absence of spines, depth habitat, carbon and boron isotope changes with size/ontogeny, B/Ca ratios). A basis for this exists in the pioneering model of Zeebe et al. (222), which has already been useful in explaining vital effects on early Cenozoic foraminiferal $\delta^{13}\text{C}$ (248), and might yet be used to predict deep time boron isotope vital effects pending further empirical physiological measurements from laboratory cultures (e.g., rates of respiration, photosynthesis and calcification, and spatially-resolved microenvironment pH change). Recent work has also demonstrated the power of fast repetition rate fluorometry (FRRF), Chlorophyll *a* quantification, and symbiont counts to quantify photosynthetic capacity (223, 249, 250), providing encouragement that these sorts of advances are within reach. Similarly, to constrain respiration rates in extinct species, shell porosity may yet prove informative (251).

Besides vital effects, another source of considerable uncertainty further back in geological time is the boron isotope composition of seawater, $\delta^{11}\text{B}_{\text{sw}}$ – a crucial parameter in converting foraminiferal $\delta^{11}\text{B}$ to seawater pH. A number of techniques has been used to estimate this parameter: researchers have studied which values of $\delta^{11}\text{B}_{\text{sw}}$ would produce feasible vertical ocean pH gradients or ocean saturation states given measured foraminiferal $\delta^{11}\text{B}$ (212, 232, 234, 246, 252), or have compared bottom water pH reconstructed from benthic foraminiferal $\delta^{11}\text{B}$ to predictions of Earth system models, and back-calculated $\delta^{11}\text{B}_{\text{sw}}$ (253). While often elegant, all approaches rely to some extent on model reconstructions of either ocean pH, alkalinity or [DIC], and some require assumptions to be made about the presence, magnitude or sign of vital effects, which as we discuss above, are not always certain. If a reliable independent record of $\delta^{11}\text{B}_{\text{sw}}$ could be found, it would remove a significant source of uncertainty in Cenozoic paleo-CO₂ reconstruction from this proxy. Fluid inclusions might yet provide one such archive, although the only reconstruction of $\delta^{11}\text{B}_{\text{sw}}$ from fluid inclusions published to date from evaporites (254) produced values too low to be compatible with early Cenozoic carbonate $\delta^{11}\text{B}$ values. Model estimates based on the long-term boron cycle also exist (255, 256), but these are extremely sensitive to the assumptions made (257), and cannot easily be corroborated independently.

Similarly, improving estimations of a second parameter of the marine carbonate system is an area of active research. In the absence of a proxy for alkalinity or DIC, reconstructions of

Pleistocene CO₂ have tied modern alkalinity or DIC to sea level-modulated variations in salinity (e.g., 191, 224), but variations in terrestrial weathering, mantle fluxes and seafloor weathering on multi-million year time scales have changed the elemental composition of seawater over the Cenozoic (e.g., 258) and therefore also alkalinity and DIC (e.g., 211, 259). Because the relative importance of weathering and mantle fluxes on marine carbonate chemistry is only weakly constrained, deeper time reconstructions therefore often utilize the surface ocean calcium carbonate saturation state (i.e., $\Omega_{\text{calcite}} = [\text{Ca}]_{\text{sw}} * [\text{CO}_3^{2-}]/K_{\text{sp}}$) as a constraint (e.g., 60, 68, 212). This is because model estimates suggest that surface ocean Ω_{calcite} varied little (i.e., ± 1) over the Cenozoic (211, 245, 259, 260). Studies often apply a modern or a modelled latitudinal gradient of Ω_{calcite} (e.g., from 6.5 in the tropics to 4.5 in the high latitudes), with some bounds of uncertainty, to estimate paleo- Ω_{calcite} . This provides a reasonable approximation to surface ocean [CO₃²⁻], which can then be paired with $\delta^{11}\text{B}$ -derived pH to estimate paleo-CO₂. We note however that reconstructions based on this approach are doubly subject to uncertainty in past ocean [Ca], since [Ca] is used both for adjusting dissociation constants in deeper time reconstructions and also in the numerator of Ω_{calcite} . Although development of a targeted DIC or alkalinity proxy would substantially refine paleo-CO₂ estimates from boron isotopes, efforts to date have not yet found a proxy candidate with sufficient sensitivity or specificity.

Further development of the boron isotope proxy can also be made by leveraging recent analytical advances. Technological improvements, such as 10¹³Ω amplifiers (261) allow precise measurements to be made from < 2 ng of B, opening up the proxy to time periods where suitable carbonate material may be scarce. Additionally, the ability to analyse smaller samples should permit better exploration of vital effects: for instance, increasing $\delta^{11}\text{B}$ with shell size is a diagnostic feature of modern symbiont-bearing foraminifera (203, 213, 217), but typical ~20 cm³ IODP core samples rarely yield sufficient material to analyse multiple size fractions of a species with previous sample-size requirements. Furthermore, new amplifiers coupled with advances in correcting for CaCO₃-matrix effects (262-264), could allow chamber-by-chamber analyses of foraminiferal shells by in situ laser ablation approaches - potentially informing on depth migration and changing physiology with ontogeny. [Return to Error! Reference source not found.](#)[Error! Reference source not found.](#)Table S2.

3. Stomatal frequencies

3.1. Current understanding of stomatal frequency proxies and recent advances

McElwain and Steinthorsdottir (23), Porter et al. (265) and Konrad et al. (22) provide a comprehensive overview of stomatal frequency proxies, their assumptions, limitations and recent methodological advances. These proxies are based on the observation that the frequency of stomatal pores often scales inversely with the concentration of atmospheric CO₂ during growth. This is because stomatal complexes are the main sites for CO₂ and water vapor exchange, and leaves operate following optimality principles to maximize CO₂ uptake and minimize water loss. Consequently, **stomatal density**, i.e., the number of stomata per unit leaf area, is typically low when atmospheric CO₂ is abundant, thereby minimizing water loss. In contrast, when CO₂ is low, a high stomatal density is necessary to ensure sufficient carbon supply, albeit at a higher

water cost. Although conceptually straight-forward, the stomatal density proxy is affected by multiple environmental parameters in addition to CO₂ and there are always biological exceptions to these rules. This led to the use of the **stomatal index**, which is the percentage of stomata in the sum of stomatal and epidermal cells. The stomatal index is much less affected by humidity and other non-CO₂ factors than stomatal density, but both proxies (stomatal density and index) are explicitly defined by calibrations using living species. The **stomatal ratio** extends the concept to extinct species, by relating the ratio of modern/paleo stomatal density or stomatal index to the ratio of paleo/modern CO₂.

While leaf growth and subsequent development of stomatal patterning, geometry and density in direct contact with the paleoatmosphere is a major advantage of these proxies, the stomatal density and index proxies (also called transfer functions) are empirical and their calibrations are time consuming. While several studies have recorded species-specific responses (sometimes—but not always—different even within the same genus), many genera (and even higher taxonomic levels) record similar stomatal densities and stomatal indices of fossil leaves, and parallel responses to CO₂ (e.g., 266, 267-270). To date, around 40 species have been calibrated for the stomatal density and stomatal index proxies, which means that most of the paleobotanical record currently cannot be used when the goal (such as here) is to generate fully quantitative CO₂ records that can be compared to independent proxy estimates. However, much can still be learned about relative paleo-CO₂ changes using more semi-quantitative methods, such as **stomatal ratios** and **stomatal indices** calibrated with non-conspecific nearest living equivalents. In addition, many species lose their sensitivity at high CO₂ (above 500 to 1000 ppm), meaning that the upper uncertainties become unbounded, whereas others only seem sensitive to above-ambient CO₂ (271, 272). Recent advances address several of these limitations (22, 23), and assemblage approaches have been suggested to overcome inter-species variations (e.g., 265). [Return to Error! Reference source not found.](#)[Error! Reference source not found.](#)**Table S2.**

3.1.1. Uncertainties and error propagation

Most recent estimates using calibrated functions of stomatal density and stomatal index constrain the uncertainties in estimated CO₂ by propagating the uncertainties in the calibration function and fossil measurements using Monte Carlo simulations (269, 273). Our strategy for updating uncertainties in older estimates is described in the following section. [Return to Error! Reference source not found.](#)[Error! Reference source not found.](#)**Table S2.**

3.2. Criteria for vetting stomatal frequency proxy records and data revisions

A total of 29 Cenozoic records has been published using these proxies (95, 266, 273-299). *Category 3:* Several records are considered unreliable in their current form, some for multiple reasons. For instance, stomatal density is usually more strongly affected than stomatal index by variations in environmental factors such as water availability and irradiance (300); this impacted three records (276, 289, 297). Estimates of Retallack (285) are based on measuring stomatal index from published figures of mixed quality (see examples in 277) and do not represent a random field-of-view. Some stomatal index estimates applied calibrations of extant species to different fossil taxa (281, 283, 285, 289-293), the concern being that some stomatal index responses to CO₂ are species-specific, even within the same genus (95, 266, 271, 301-303), although this is not always the case (see above). Furthermore, some estimates do not fully propagate uncertainties

in both the fossil and calibration measurements (95, 281, 289, 291, 292, 295, 304). In such cases where the calibration data are publicly available, estimates not placed into Category 3 for other reasons were revised using the approach of Beerling et al. (273), which fully propagates uncertainties in all fossil and calibration measurements (95, 277, 295). Similarly, the *Metasequoia* estimates of Beerling et al. (273) were updated with the more extensive calibration of Doria et al. (280).

Category 2: The stomatal ratio proxy relates the ratio of paleo-to-modern CO₂ to the ratio of fossil-to-modern stomatal density or stomatal index. The proxy assumes a prescribed inverse power law response between CO₂ and stomatal frequency, and applies a one-point calibration between present-day CO₂ and stomatal frequency measurements (e.g., 305). This proxy is most often applied when the nearest living relative of a fossil is not clearly known and where it can be argued that selection of an ecological and/or morphological equivalent is a more robust approach than selection of a very distantly related phylogenetic relative. As such, these estimates and their associated uncertainties are less quantitative (298, 306) and thus cannot be compared directly to more quantitative estimates from other proxies. Because of this, we place stomatal ratio estimates into Category 2 if they do not otherwise satisfy conditions for Category 3 (287, 290-293, 298, 299). In cases where estimates at individual sites are based on multiple species (292, 293), the mean of the individual estimates and uncertainties is reported.

Additional stomatal frequency estimates that are valued semi-quantitatively (Category 2) are those whose (i) measured fossil stomatal values fall outside the range captured in the extant training set (277); (ii) where the same cuticles were used to estimate CO₂ using a leaf gas-exchange proxy (273, 274, 282, 284), which should yield more quantitative estimates (22, 305); or (iii) when estimates are based on fewer than five leaves, which is the minimum level of sampling generally observed to reduce the risk of spurious CO₂ estimates (307, 308). This final criterion affects the records of Kürschner et al. (283) and Stults et al. (276), who did not report the number of leaves analyzed, and parts of several others that measured <5 leaves for some of their data points (273, 277, 281, 285, 291, 292, 295, 297, 304). [Return to Error! Reference source not found.](#)**Table S2.**

3.3. Future directions

In all stomatal proxies, confidence in estimated CO₂ improves when multiple species (293) and multiple proxies (282, 293, 309) are analyzed. Stomatal frequency and leaf gas-exchange proxies would benefit from comparing paleo-CO₂ estimates from all methods on the same sample material, so that better insight can be gained for their respective strengths and weaknesses. Most importantly, a solid theory needs to be established for why stomatal frequency proxies tend to record low paleo-CO₂ for the Cenozoic relative to other proxies. Most climate models cannot reproduce the temperatures recorded for many parts of the Cenozoic with the paleo-CO₂ estimates of the stomatal frequency proxies (310); our current understanding of how the Earth system works does not support such low paleo-CO₂. Intra- and inter-proxy differences need to be mapped out carefully, and it needs to be established whether, e.g., a systematic correction factor could be justified for stomatal frequency proxies. Haworth et al. (271) and Elliott-Kingston et al. (311) have suggested that the magnitudes of plant developmental and physiological responses to atmospheric CO₂ are contingent on the long-term baseline CO₂ values under which

the entire lineage has evolved, which may support the introduction of systematic correction factors. To this end, an IODP cruise to specifically target shallow marine Cenozoic sediments with abundant cuticle material or charcoaled fragments could be a compelling tool for evaluating and comparing stomatal proxies with marine based proxies and high stratigraphic control. The cuticle could be used to compare all aspects of isotope- and stomatal-based proxy methods, and comparison to marine proxies may be possible if abundance, preservation state and air-sea CO₂ equilibrium allow. More advanced plant growth chamber studies under elevated CO₂ atmospheres are also required to tease out limitations of the stomatal proxy and their underlying basis. An important target will be multi-generation studies where first, second and third generation seed produced under different long-term baselines can be evaluated for their capacity to generate robust CO₂ estimates under radically different CO₂ conditions (that is outside their ‘evolutionary memory’). Finally, identifying well-preserved fossil plants (ideally with close living relatives) from well-dated (or datable) terrestrial strata, deposited at key intervals during the Cenozoic remains an important goal. [Return to Error! Reference source not found.](#)[Error! Reference source not found.](#)**Table S2.**

4. Leaf gas exchange

4.1. Current understanding of the leaf gas-exchange proxies and recent advances

Atmospheric CO₂ estimation based on leaf gas-exchange principles follows a mechanistic model that equates atmospheric CO₂ concentration (c_a) with the ratio of the rate of carbon assimilation during photosynthesis (A_n , the flux of CO₂ into a leaf in units of $\mu\text{mol m}^{-2} \text{s}^{-1}$) to the product of total leaf diffusive conductance to CO₂ ($g_{c(\text{tot})}$, in units of $\text{mol m}^{-2} \text{s}^{-1}$) and the relative CO₂ concentration gradient between atmosphere and leaf interior ($1 - c_i/c_a$) (312):

$$c_a = \frac{A_n}{g_{c(\text{tot})} \times (1 - \frac{c_i}{c_a})} \quad (\text{Eq. 4.1})$$

Equation 4.1 is a rearrangement of the basic diffusion equation governing A_n during photosynthesis (159). For a given relative CO₂ concentration gradient ($1 - c_i/c_a$), higher c_a will be associated with higher A_n and/or lower $g_{c(\text{tot})}$. The rationale behind the leaf gas-exchange proxies is that information about the components of equation 4.1 is preserved in the anatomical and chemical composition of fossil leaves.

There are two major leaf gas-exchange proxies for atmospheric CO₂ (312, 313). In both models, the ratio c_i/c_a is determined from measurements of fossil leaf $\delta^{13}\text{C}$ along with an estimate of paleoatmospheric $\delta^{13}\text{C}$, the latter of which probably varied by $\sim 3\%$ across the Cenozoic (314). In addition, the stomatal conductance to CO₂—one of the components of total leaf conductance along with boundary layer and mesophyll conductance—is calculated from fossil measurements of stomatal density and stomatal size. The inverse power law behavior between stomatal conductance and atmospheric CO₂ implied in Eq. 4.1 is broadly in keeping with the observations used in the stomatal frequency proxies described in section 3.1.

A_n and the other two components of leaf conductance (boundary layer and mesophyll conductance) cannot be measured directly on fossils. In the Franks et al. (312) model, A_n of the fossil leaf specimen referenced to modern c_a (i.e., A_0) is normally inferred from a nearest living

relative and scaled to its value at paleo- c_a according to the theory that plants adapt to c_a by optimizing the relative investment of chloroplast protein in light-limited vs. Rubisco capacity-limited photosynthetic reactions (315); boundary layer conductance is fixed at a value that is typical for when leaves are photosynthesizing normally; and mesophyll conductance scales with A_n . In the reduced order model of Konrad et al. (316), A_n and $g_{c(tot)}$ are determined with a mechanistic model of photosynthesis that requires inputs such as the mitochondrial respiration rate (R_d), maximum rate of rubisco carboxylase activity ($V_{C_{max}}$), leaf size, thickness of assimilation tissue and leaf temperature.

The second major leaf gas-exchange proxy is the optimization model of Konrad et al. (313). This model assumes that stomatal activity regulates gas exchange in a way that assimilation is maximized and transpiration is minimized. Input parameters include leaf anatomy (available from fossils) and (assumed) values of leaf temperature, air humidity, insolation, and (soil) water availability. Though this model is more comprehensive than the models of Franks et al. (312) and Konrad et al. (316), it requires a more detailed knowledge of (or more audacious assumptions about) the paleoenvironment. [Return to Error! Reference source not found.](#)[Error! Reference source not found.](#)**Table S2.**

4.1.1. Uncertainties and error propagation

For all leaf gas exchange models, the current standard practice for constraining uncertainty in estimated CO₂ is to propagate uncertainties in all of the inputs (both measured and inferred) using Monte Carlo simulations (282, 312). [Return to Error! Reference source not found.](#)[Error! Reference source not found.](#)**Table S2.**

4.2. Criteria for vetting leaf gas exchange proxy records and data revisions

A total of 18 Cenozoic leaf gas exchange records has been published to date (274, 275, 282, 284, 293, 312, 317-328). *Category 3:* We placed the paleo-CO₂ estimates reported in Franks et al. (312) into Category 3 because leaf $\delta^{13}\text{C}$, which is used to calculate c_i/c_a , was not measured on the same samples from which stomatal dimensions were collected; instead, the authors inferred c_i/c_a via regression from a Phanerozoic compilation. While their CO₂ estimates are broadly consistent with the overall patterns presented here (Figs. 1a and 2a), they possibly contain some error as a result of differences between the regression-derived and directly inferred c_i/c_a values for leaf cuticles, the latter taken to be the standard for this proxy method. Data revisions were applied for several reasons. First, several studies estimated paleo-CO₂ at individual sites from multiple species (282, 293, 323, 328). To avoid oversampling of the same time window from a single site, the resampled CO₂ distributions from all species were combined into a single paleo-CO₂ estimate. Second, uncertainty of most estimates generated with the Konrad et al. (313) leaf-gas exchange method only include variations in the most sensitive inputs that are not directly measured in fossils. Kowalczyk et al. (282) presented a more rigorous alternative, where all inputs—directly measured in fossils and inferred from nearest living relatives—were propagated using Monte Carlo simulations. All estimates from the Konrad approach were revised along these lines (322, 324, 325). [Return to Error! Reference source not found.](#)[Error! Reference source not found.](#)**Table S2.**

4.3. Future directions

The sensitivity of the input variables on estimated CO₂ is explored extensively elsewhere (282, 284, 305, 317, 329). The Franks leaf gas-exchange method is particularly sensitive to two inputs not directly measured on fossils: the assimilation rate at a known CO₂ concentration (A_0) and the ratio between operational and maximum stomatal conductance to CO₂ (i.e., $g_{c(\text{op})}/g_{c(\text{max})}$, or ζ , 284, 329). Global surveys of woody angiosperm taxa demonstrate generalized scaling relationships between $g_{c(\text{op})}/g_{c(\text{max})}$ (330) that broadly support the recommended values originally proposed by Franks et al 2014). However, tests with living plants generally yield more accurate CO₂ estimates when A_0 and $g_{c(\text{op})}/g_{c(\text{max})}$ are measured instead of assumed from recommended values for broad taxonomic groups (265, 317, 328, 331). Thus, accuracy in paleo-CO₂ estimates is likely best when based on taxon-specific information of A_0 and $g_{c(\text{op})}/g_{c(\text{max})}$.

As in all stomatal proxies, accuracy in estimated CO₂ improves when based on multiple species (293, 323) and multiple proxies (282, 293). For example, in a test of the Franks leaf gas-exchange proxy in 40 extant species, estimated CO₂ for individual species ranged between 275 and 850 ppm but the multi-species median was 472 ppm, close to the target concentration of 400 ppm (305). Multiple species and multiple proxies should be applied whenever possible. [Return to Error! Reference source not found.](#)[Error! Reference source not found.](#)**Table S2.**

5. Liverworts

5.1. Current understanding of the liverwort proxy and recent advances

Liverworts are one of the oldest groups of land plants. They are small in stature, have no tissues to conduct fluids (i.e., no xylem or phloem), and their photosynthetic gametophytic tissue always lacks stomata but typically has pores that remain fixed in size and shape when the epidermal cells are hydrated. Because liverworts lack functional stomata, their CO₂ uptake is controlled by passive diffusion across cell membranes or through fixed pores. As such, the carbon isotope fractionation during photosynthesis is partly controlled by the amount of atmospheric CO₂, where higher CO₂ allows the plants to be more selective in their carbon assimilation and $\delta^{13}\text{C}$ of the plant tissues decreases. Similar to the marine phytoplankton proxy, carbon isotope fractionation is also affected by growth rate. This is accounted for with a photosynthesis model (for details, see 332) that requires inputs such as irradiance. [Return to Error! Reference source not found.](#)[Error! Reference source not found.](#)**Table S2.**

5.2. Criteria for vetting liverwort proxy records and data revisions

Because liverwort fossils are uncommon, the proxy is rarely used - only three estimates have been published in two studies (282, 333). The only revision applied to these records is the update of atmospheric $\delta^{13}\text{C}$ following Tipple et al. (314). [Return to Error! Reference source not found.](#)[Error! Reference source not found.](#)**Table S2.**

5.3. Future directions

Similar to the leaf gas-exchange proxies, the leaf assimilation rate is an important input in the liverwort proxy and solar irradiance strongly affects this rate. This is normally not a problem with trees, because sun leaves dominate the fossil record (see 305), but liverworts grow close to the forest floor. As a result, selecting sites with an interpreted open canopy or habitat is important

(282) but given the rarity of liverwort fossils, future sampling efforts will likely be limited. [Return to Error! Reference source not found.](#)[Error! Reference source not found.](#) **Table S2.**

6. Land Plant $\delta^{13}\text{C}$ proxy

6.1. Current understanding of the land plant $\delta^{13}\text{C}$ proxy and recent advances

The modern land plant $\delta^{13}\text{C}$ -based CO_2 proxy is based on a combination of observations of natural trends (e.g., 334, 335) and experimental studies by Schubert and Jahren (24) that related increasing carbon isotope fractionation ($\Delta\delta^{13}\text{C} \approx \delta^{13}\text{C}_{\text{air}} - \delta^{13}\text{C}_{\text{plant}}$) to increasing atmospheric CO_2 . The mechanism for the CO_2 effect on $\Delta\delta^{13}\text{C}$ is proposed to reflect carbon isotope fractionation during photorespiration (336, 337), a process that occurs when stomata close during hot and dry conditions during the day, and the concentration of O_2 in the leaves exceeds the concentration of CO_2 . Under such conditions, formerly fixed glycine is reverted to CO_2 and O_2 is consumed. Photorespiration thus curbs carbon fixation and reduces the efficiency of photosynthesis. Experiments have shown that ^{13}C discrimination during photorespiration decreases the $\delta^{13}\text{C}$ of *Arabidopsis* by a few per mil (Schubert and Jahren, 2018). Photorespiration may have evolved when CO_2 levels were relatively high and oxygen levels exceptionally low (338-340).

The accuracy of the land plant $\delta^{13}\text{C}$ proxy has been tested using geological materials across the ~ 100 ppm CO_2 increase from the last glacial to the Holocene, and through analysis of fossil faunas or plant organic matter at (usually) elevated CO_2 , but for which CO_2 is known only through other proxies (341-345). To minimize the dependency on other paleo- CO_2 proxies, it is recommended to calculate CO_2 concentrations relative to an independent baseline CO_2 value. For instance, for their Deglacial and Neogene reconstructions, respectively, Schubert and Jahren (341) and Cui et al. (346) calculated CO_2 relative to Holocene ice core measurements of 270 ± 7 ppm between 11,500 and 100 yrs ago (Method 1). However, using a Holocene baseline is not considered feasible for deep time studies (e.g., 347); Cui and Schubert (348) therefore used CO_2 estimates from stomatal and paleosol proxies as baseline for deep time studies (i.e., 286, 349, 350).

Another approach (Method 2) to apply this proxy requires the knowledge of changes in CO_2 (ΔCO_2) across a rapid climate change event (e.g., the PETM and subsequent Early Eocene hyperthermals, 351) and the difference in the magnitude of carbon isotope excursion (CIE) between the atmosphere and terrestrial organic matter (i.e., $\Delta\text{CIE} = \text{CIE}_{\text{atm}} - \text{CIE}_{\text{OM}}$). Because ΔCO_2 is often poorly known, or determined by carbon cycle models that require the assumption of a carbon source to determine the amount of carbon added to the Earth system, Method 2 is considered to be qualitative. The sensitivity of the proxy using Method 1 has been evaluated in several studies. An analysis of plant organic matter for the last glacial-Holocene transition suggested good correspondence with ice core measurements (341), with a sensitivity of $\sim 2\%$ increase in $\Delta^{13}\text{C}$ per 100 ppm increase in CO_2 , although the reliability of this interpretation has been questioned in the context of other confounding factors (345)

Recent experiments (265, 337, 352-354) explored additional variables and emphasize three factors that independently contribute to $\Delta\delta^{13}\text{C}$: the ratio of atmospheric CO_2 to O_2 , the latter of which has also varied through Earth history, water availability, and species or phylogeny (especially spore-producing vs. seed-producing plants, but also conifers vs. angiosperms, see 345,

355). Other factors that can affect the $\Delta\delta^{13}\text{C}$ record include organic matter preservation (e.g., mixing, reworking, or diagenesis) and contributions from isotopically disparate C_4 plants and diatoms (e.g., 356). While the effects of water availability and plant species on $\delta^{13}\text{C}_{\text{plant}}$ can be on the order of several per mil (345, 352, 355), the effects of variable O_2 are likely small (265). Direct measurements from ice cores show a 0.7% decrease in O_2 over the past 800 kyr (357), and models of Cenozoic O_2 suggest a range from $\sim 18\%$ to $\sim 24\%$, with no consensus on trend (see summary by 358). An uncertainty of $\pm 3\%$ in O_2 would propagate to a CO_2 uncertainty of $\sim \pm 15\%$, which is smaller than uncertainties in calculated paleo- CO_2 that arise from annual precipitation and plant species, but still a significant contributor that would benefit from additional research. For instance, modern studies suggest a small CO_2 -effect ($\sim 0.4\text{‰}/100$ ppm) for oak (*Quercus*, 359) and no resolvable CO_2 -effect for pine (*Pinus*, 359), tropical hardwoods (345), or ginkgo (354). Instead, ginkgo showed changes in other leaf characteristics, rather than $\Delta\delta^{13}\text{C}$ (354). Analyses of speleothems (360), which inherit their $\delta^{13}\text{C}$ values from surrounding vegetation, and tree ring cellulose (343) support a CO_2 effect across the last deglaciation, albeit smaller than proposed by Schubert and Jahren (24): $1.6 \pm 0.3\text{‰}$ and $1.7 \pm 1.5\text{‰}$ per 100 ppm, respectively. Analysis of collagen, which also inherits its $\delta^{13}\text{C}$ values from surrounding vegetation, is inconclusive ($0.5 \pm 1.5\text{‰}/100$ ppm, 343). In contrast, sparse studies of Late Cretaceous through Pliocene sedimentary organic matter and tooth enamel of mammals show no clear CO_2 effect on $\Delta\delta^{13}\text{C}$, or possibly even a negative effect ($-0.4\text{‰}/100$ ppm) (342, 344, 345). However, these studies make corrections for precipitation, which is not always well known, and assume proxy-derived paleo- CO_2 estimates, which are subject to large uncertainties and/or may not coincide exactly in time.

One recent study did not find significant statistical relationship between $\Delta\delta^{13}\text{C}$ and CO_2 over short timescales (i.e., decadal to centennial, 361), while other studies show that carbon isotope fractionation of angiosperms and gymnosperms responds to CO_2 differently, such that $\Delta\delta^{13}\text{C}$ is more sensitive to CO_2 in angiosperms (347, 362), and the carbon isotope fractionation may be negatively related to CO_2 at low levels (< 400 ppm) (151, 363). These conflicting results suggest that further work is needed to better quantify the effect of carbon isotope fractionation in land plants in both laboratory and natural settings.

Several recent studies have reconstructed Cretaceous through Cenozoic paleo- CO_2 including assessments of calibration uncertainty (e.g., 346, 348). Because the sedimentary record offers a rich archive of organic carbon throughout the Phanerozoic, the land plant $\delta^{13}\text{C}$ -based CO_2 proxy offers an opportunity to reconstruct paleo- CO_2 at much higher temporal resolution than many other proxies (364). In summary, significant progress has been made over the last 10 years to quantify paleo-atmospheric CO_2 from $\Delta\delta^{13}\text{C}$ in the fossil remains of C_3 land plants, but more work is required to constrain the magnitude of the CO_2 effect, to define deep-time baseline CO_2 values and their effect on the CO_2 reconstruction, to account for variations in local flora that may have different sensitivity to CO_2 , and to better understand the controlling mechanisms over geological timescales [Return to Error! Reference source not found.](#)[Error! Reference source not found.](#)[Table S2.](#)

6.2. Criteria for vetting land plant $\delta^{13}\text{C}$ proxy records and data revisions

Because paleo- CO_2 estimates from this proxy change with the selected CO_2 baseline value, these estimates (293, 341, 346, 348, 365) are not truly independent of other CO_2 estimates and have

therefore been excluded from the paleo-CO₂ compilation used for constraining the Cenozoic CO₂ curve (Fig. 1a), but are shown relative to that curve on Fig. 1b (Category 2). In addition, several revisions have been made relative to original publications. Because data from this proxy were originally published with 68% confidence intervals; these estimates have been recalculated using the R script developed by Cui and Schubert (348) and are now reported with propagated 95% confidence intervals. The error propagation includes the uncertainties of calibration equations and of the $\delta^{13}\text{C}$ values of organic matter, atmospheric CO₂, and modern leaves. Plant species effects and potential paleo-moisture variability are addressed by increasing the $\delta^{13}\text{C}$ uncertainties of fossil organic matter beyond the analytical uncertainty (365). Corrections for paleo-O₂ are not applied because this parameter is poorly constrained and proxy sensitivity to this parameter is relatively minor. Diagenesis is also not yet addressed because there is no clear basis for correcting data. In addition, Cui et al. (365) reported individual CO₂ estimates of 5-15 replicate analyses of coeval subsamples from the same collection site. To avoid overrepresentation of data from the same samples and time period, these replicate estimates have been averaged and uncertainties are reported as the maximum and minimum 95% confidence limits of the highest and lowest original CO₂ estimates of each sampling interval. [Return to Error! Reference source not found.](#)[Error! Reference source not found.](#) **Table S2.**

6.3. Future directions

Improving the land plant $\delta^{13}\text{C}$ proxy will require probing in several directions. In particular, previous experiments have been mostly restricted to a constant water regime (24, 353). Experiments testing the moisture effect on $\delta^{13}\text{C}_{\text{plant}}$ often used watering rates in excess (i.e. >950 mm/yr, 352) of the mean annual precipitation rates that $\delta^{13}\text{C}_{\text{plant}}$ is most sensitive to (i.e. ≤ 500 mm/yr, 355, 366). New experiments are needed to investigate different phylogenetically disparate plant species under environmental and watering regimes that encompass more natural conditions, e.g., in free air experiments (e.g., 354). Correction for precipitation should be included and may be estimated using proxies based on water isotopes (e.g., 367), tree rings (e.g., 368, 369), leaf fossils (e.g., 370) and/or organic compounds (371). Although independent precipitation proxies are scarce, progress may be possible using other geochemical indices such as paleosol chemistry (372) or from new advances in constraining paleoaridity using either isotopic discrimination among sympatric taxa or from multiple isotopes (e.g., 373, 374-376).

Furthermore, it has been suggested that land plant $\delta^{13}\text{C}$ might be sensitive to CO₂ on short timescales, but evolves to show smaller sensitivity on longer, evolutionary, timescales (345). Further laboratory, field and geological studies are needed to improve the accuracy and precision of the land plant $\delta^{13}\text{C}$ proxy on both short and long evolutionary timescales. The rapid deglacial and anthropogenic CO₂ increases provide excellent opportunities to better quantify the CO₂ effect on recent and short time scales. For deeper-time validation, $\Delta^{13}\text{C}$ of fossil faunal and floral remains could be cross-validated against other paleo-CO₂ proxies. Furthermore, and because most observational data are as yet restricted to northern Europe, tests should be conducted in different areas of the world with different species. Analyses of sedimentary organic matter should also be supplemented with information on the preservation state of the studied organic materials, and, if possible, taxonomic specification, so that species-specific fractionation can be

taken into account and phylogenetic correction factors applied where applicable (e.g., 353). [Return to Error! Reference source not found.](#)[Error! Reference source not found.](#)Table S2.

7. Paleosols

7.1. Current understanding of the paleosol proxy and recent advances

The paleosol carbonate paleo-CO₂ proxy is based on the mixing of CO₂ in soil pore spaces between two endmembers 1) respired CO₂ from plant roots and microbes in the soil and 2) atmospheric CO₂ (Fig. S5, 25, 377). In the relevant mixing relationship, typically expressed as:

$$CO_{2,atm} = S(z) \left[\frac{\delta_s - 1.0044\delta_r - 4.4}{\delta_a - \delta_s} \right] \quad (\text{Eq.7.1})$$

there are five variables: 1) the concentration of atmospheric CO₂ (CO_{2,atm}) 2) the concentration of CO₂ from soil respiration (S(z)), 3) the δ¹³C value of atmospheric CO₂ (δ¹³C_a), 4) the δ¹³C value of respired CO₂ (δ¹³C_r, sometimes referred to as soil-respired CO₂ to distinguish from CO₂ respired aboveground) and 5) the δ¹³C value of soil CO₂ (δ¹³C_s, this is the CO₂ mixture that occupies the soil pore spaces). The constants in equation 7.1 account for carbon isotope fractionation that occurs during gas phase diffusion in the soil pore network (Cerling 1984) and are based on well-established theory (378, 379). Atmospheric CO₂ concentrations are determined by specifying values of the other four variables. Whereas various approaches have been used over the past 30 years to determine values for S(z), δ¹³C_r and δ¹³C_a (as reviewed by Breecker 2013) all applications of this proxy determine values for δ¹³C_s from measurements of δ¹³C values of paleosol carbonates and a temperature-sensitive carbon isotope fraction factor relating δ¹³C values of calcite to δ¹³C values of CO₂ gas (177). In the subsequent paragraphs, we discuss each of these variables, the methods that have been used to determine their values for use in Eq. 7.1 and current understanding of the proxy.

Values of δ¹³C_a for use in Eq. 7.1 are based on either the δ¹³C of contemporaneous marine carbonates or on the δ¹³C of land plants, applying relevant carbon isotope fractionation factors (e.g., 380). Values of δ¹³C_r have been either based on 1) the δ¹³C of organic matter from the paleosol of interest, from stratigraphically nearby coal, or from more geographically distant locales, or 2) the δ¹³C of marine carbonates from which the δ¹³C of atmospheric CO₂ and δ¹³C of land plants have been inferred. The sensitivity of C₃ plant δ¹³C values to atmospheric CO₂ (see also Section 6 above, e.g., 24, 334) and rainfall (e.g., 342, 345) indicate complications associated with calculating atmospheric CO₂ δ¹³C values from plant δ¹³C values (or vice versa). This is particularly the case since soils that precipitate calcium carbonate are most common in arid – subhumid environments, where plant δ¹³C is most sensitive to rainfall. For this same reason, the δ¹³C of plants growing in coal swamps may not be representative of plants growing in calcic soils, even if these deposits are stratigraphically close together. Therefore, it is preferable to determine δ¹³C_a from marine records and δ¹³C_r from organic matter in the paleosol of interest. That said, if multiple variables sensitive to CO₂ can be measured from the same deposits – e.g., δ¹³C values of organic carbon and of paleosol carbonate – this would certainly be worthy of exploration, with the understanding that other factors may affect both.

There are also complications associated with using $\delta^{13}\text{C}$ of paleosol organic matter as a proxy for $\delta^{13}\text{C}_r$. These complications are rooted in the effects of decomposition on the $\delta^{13}\text{C}$ values of soil organic matter. For instance, in well-drained modern soils, the $\delta^{13}\text{C}$ of organic carbon typically increases with depth by up to 6‰ (Fig. S5, e.g., 381, 382). Approximately 2‰ of this down-profile $\delta^{13}\text{C}$ increase can be explained by the decrease in $\delta^{13}\text{C}$ values of atmospheric CO_2 over the past century (i.e., the Suess effect, 383), leading to organic carbon with lower $\delta^{13}\text{C}$ in shallower soils. However, the magnitude of the Suess effect is insufficient to explain the entire down-profile $\delta^{13}\text{C}$ increase. In addition, the study of an archived soil core (avoiding most of the Suess effect) shows a relatively small, but non-zero down-profile $\delta^{13}\text{C}$ increase (from the A to the B horizon) of approximately 1.5‰ (384). These considerations suggest other processes contribute to down-profile $\delta^{13}\text{C}$ increases. It has been suggested that soil microbes release CO_2 with a lower $\delta^{13}\text{C}$ than the organic carbon they consume (385, 386). Although laboratory soil incubations suggest that $\delta^{13}\text{C}$ of respired CO_2 is nearly indistinguishable from $\delta^{13}\text{C}$ of total organic matter in the top 2 cm of soil where the youngest and freshest organic matter resides (387), it is possible that fractionation occurs during metabolism of more recalcitrant organic carbon deeper in soils, contributing to the down-profile $\delta^{13}\text{C}$ increase. Although respiration occurs throughout the soil, the organic matter preserved in paleosols is typically from the deeper B horizon, where respiration rates are lower (Fig. S5). Therefore, the organic matter preserved in paleosols probably does not directly reflect the majority of soil respiration which occurred at shallower depths where organic matter $\delta^{13}\text{C}$ values are typically lower. Therefore, a small adjustment (currently estimated at -1‰) is probably necessary to determine $\delta^{13}\text{C}_r$ from measured $\delta^{13}\text{C}$ values of paleosol organic carbon. However, for most paleosols, the uncertainty in the magnitude of this adjustment is strongly overshadowed by uncertainty in the value of $S(z)$ (see below).

Temperatures of paleosol carbonate formation can be determined using the clumped isotope thermometer (388, 389). The temperature sensitivity of calculated atmospheric paleo- CO_2 is 4% of the calculated CO_2 per Kelvin. Therefore, a temperature uncertainty of $\pm 3^\circ\text{C}$ results in reasonably small error. However, soil carbonate formation temperatures determined from modern soils span a few degrees below mean annual air temperature (MAAT) to maximum monthly air temperature (MMAT, 390). The difference between MAAT and MMAT is large and quantifying temperature of carbonate formation rather than assuming mean annual temperature can make a difference (e.g., compare Ji et al. (35) with Heitmann et al. (391) and Zhang et al. (392) with Huang et al. (393), and is recommended when possible (e.g., when samples are not too deeply buried, 26).

The concentration of CO_2 contributed by soil respiration ($S(z)$) is the most uncertain variable in Eq. 7.1 and the largest source of error for this proxy. The values for $S(z)$ used in early applications of this proxy ranged between 5000 and 10,000 ppmV and were based on mean growing season CO_2 concentrations in modern soils (394). By solving Eq. 7.1 for $S(z)$ and applying to Holocene soils for which atmospheric CO_2 levels are known from ice cores (395), Breecker et al. (396) suggested average $S(z)$ were closer to 2500 ppmV. Recent advancements (discussed below) have further refined values for $S(z)$ but this variable is still difficult to quantify precisely.

Several advancements to the paleosol carbonate paleo- CO_2 proxy have been made in the past decade. In particular, the Cenozoic record of atmospheric $\delta^{13}\text{C}_{\text{CO}_2}$ (314) provides a consistent

framework from which paleosol-based studies can extract this necessary constraint for the time period of interest. Several new approaches for estimating $S(z)$ have recently been proposed, including reconstructions based on (i) soil order (397), which is recognizable from paleosols and varies with climate and soil parent material, both of which influence soil carbon cycling, (ii) independently reconstructed mean annual precipitation (398), (iii) the depth in the soil to the calcium carbonate accumulating horizon (399) and (iv) magnetic susceptibility (36), which is thought to proxy rainfall in the East Asian Monsoon region (400). Although these approaches might allow secular change in $S(z)$ to be resolved, it is clear that more precise estimates are needed and the error associated with these proxies needs to be better quantified (Fig. S6). Of the existing $S(z)$ proxies, magnetic susceptibility has the smallest error but its current calibration is entirely empirical and therefore may only be applicable to soils on the Chinese Loess Plateau.

Uncertainty on the value of $S(z)$ aside, the paleosol CO_2 proxy has a number of advantages. One advantage is that paleosols with calcium carbonate horizons are common in much of the Phanerozoic geologic record. Another is the relative simplicity of the proxy, being possibly void of, or at least relatively immune to, vital effects. A third and perhaps the most significant advantage is that unlike most CO_2 proxies which saturate in the 500 – 1000 ppm range, the paleosol carbonate paleo- CO_2 proxy typically works better at higher CO_2 . The better performance at higher CO_2 occurs because uncertainty is reduced when atmospheric CO_2 concentrations and soil-respired CO_2 concentrations are approximately equal to each other (26). Appropriate soil-respired CO_2 concentrations (i.e., those that occur during the formation of soil carbonates), although currently difficult to quantify in paleosols (see below), typically range from 400 to several thousand ppm (397, 398, 401), meaning that application of this proxy is generally best suited to times periods with atmospheric CO_2 higher than modern. However, paleo respiration rates determine how well a specific paleosol is suited for use with this proxy. Paleosols with lower respiration rates are better suited for periods with low atmospheric CO_2 whereas more productive paleosols are better suited to periods with high CO_2 because the proxy works best when $S(z)$ and atmospheric CO_2 are approximately equal to each other (402). This versatility is a specific advantage of this proxy. The suitability of a paleosol (in terms of the comparison between respired CO_2 and atmospheric CO_2 levels) can be determined using Eq. 7.2 below.

$$\frac{\text{CO}_2}{S(z)} = \left[\frac{\delta_s - 1.0044\delta_r - 4.4}{\delta_a - \delta_s} \right] \quad (\text{Eq. 7.2})$$

If the $\text{CO}_2/S(z)$ ratio is less than 0.3, then sensitivity of $\delta^{13}\text{C}_s$ to atmospheric CO_2 is small because the mixture is dominated by respired CO_2 (i.e., with a little higher or lower atmospheric CO_2 the mixture would still be dominated by respired CO_2 , hence the small sensitivity) and the soil should be avoided for the purpose of atmospheric CO_2 reconstruction (399, 402). Theoretically, saturation can also occur if soil respiration rates are very low (or atmospheric CO_2 very high), in which case the soil pore spaces would be dominated by atmospheric CO_2 (i.e., paleosol carbonate $\delta^{13}\text{C}$ would record $\delta^{13}\text{C}_a$ but not atmospheric CO_2 concentration), but that problem has not, to our knowledge, been encountered in nature. Despite the absence, for all practical purposes, of loss of sensitivity at high CO_2 , many CO_2 determinations made using this proxy have right (or high CO_2)-skewed probability distributions, resulting from $S(z)$ distributions that are skewed high and from effects inherent to propagating error through an expression with variables that are multiplied by each other (Eq. 7.1).

As described above, the primary weakness of this proxy is the poor quantification of $S(z)$ values and this is where future work refining this proxy should focus. Another weakness is the uncertainty associated with decomposition effects (including possible microbial fractionation) on the $\delta^{13}\text{C}$ of soil organic matter. Error on $\delta^{13}\text{C}_r$ has a relatively small effect on CO_2 (Eq. 7.1) that scales with $\text{CO}_2/S(z)$. As $\text{CO}_2/S(z)$ increases, the difference between $\delta^{13}\text{C}_s$ and $\delta^{13}\text{C}_r$ increases (Eq. 7.2) and therefore errors on $\delta^{13}\text{C}_r$ matter less. But uncertainty about the effect of decomposition on the $\delta^{13}\text{C}$ of paleosol organic matter may be more important for time periods when atmospheric CO_2 was relatively low (i.e., the ratio of $\text{CO}_2/S(z)$ was small). Carbon isotopic fractionation during microbial respiration is one possible decomposition effect that should be further investigated, particularly in the lower parts of the A and the B horizons of soils (Fig. S5). However, quantifying microbial carbon isotope fractionation in natural soils is difficult because it can be easily conflated with preferential respiration of organic matter of different ages, which can have different carbon isotope compositions due to the Suess effect. For instance, preferential respiration of younger organic matter with lower $\delta^{13}\text{C}$ could easily be confused with microbial fractionation. Additionally, use of this proxy requires quantification of the depth beneath the paleosurface from which the carbonate sample was acquired or, at minimum, demonstration that samples were acquired from depths at which soil CO_2 concentrations were approximately invariant with depth, i.e., typically taken at >30 cm below the paleosurface. While this can be determined in some cases (e.g., 391, 403) in many paleosols, this term is difficult to define due to erosion or non-preservation of the tops of soil profiles. This is, however, likely to be only a minor contributor to error in this proxy. A final weakness is the need to correlate marine records of $\delta^{13}\text{C}_a$ to values of $\delta^{13}\text{C}_s$ and $\delta^{13}\text{C}_r$ that are determined from terrestrial deposits. This can introduce error, especially when rapid carbon cycle perturbations are being investigated. [Return to Error! Reference source not found.](#)[Error! Reference source not found.](#) **Table S2.**

7.2. Criteria for vetting paleosol proxy records and data revisions

A total of 17 Cenozoic paleosol proxy records has been published to date (35-37, 42, 349, 350, 392, 393, 398, 399, 404-410). Three primary criteria were used to vet the paleosol-based records: 1) $\delta^{13}\text{C}$ values of respired CO_2 must be determined from $\delta^{13}\text{C}$ values of paleosol organic matter; 2) the paleosols must be appropriate for this approach; and 3) $S(z)$ must be estimated with quantifiable uncertainty. The rationale for criterion 1 is the large spatiotemporal variability of vegetation $\delta^{13}\text{C}$ values (355, 366, 411). The best indicator for $\delta^{13}\text{C}$ values of respired CO_2 is the organic matter in the paleosol of interest (ideally occluded within the paleosol carbonate nodules). Enforcing this criterion resulted in five records being placed in Category 3 (392, 393, 399, 406, 409). The rationale for the second criterion is that soils with high respiration rates have too small of an atmospheric component in soil CO_2 , which results in loss of sensitivity as described above (402). Therefore, in practice, some highly productive soils are not appropriate for this approach. We screened the records and removed those for which $\text{CO}_2/S(z) < 0.3$ (see above). Enforcing this criterion resulted in two records being placed in Category 3 (350, 412), as well as some of the estimates from two additional records (37, 42). The rationale for the third criterion is that without error for $S(z)$, the uncertainty of reconstructed atmospheric CO_2 cannot be determined. Enforcing this criterion resulted in two additional records being placed in Category 3 (349, 404). One record (36) satisfies all three criteria and was placed in category 1. Da et al. (36) determined $S(z)$ from magnetic susceptibility, and the calibration and application of this $S(z)$

proxy use soils formed from similar parent material in similar climates, supporting high confidence in quantification.

In order to help evaluate whether or not error is fully quantified in the remaining records, we compared, where possible, CO₂ estimates from the same paleosols using two different methods to determine S(z) (Fig. S6). This was only possible for a few records in the database. We examined some Eocene records (37, 42) for which we compared S(z) estimated from 1) soil order (26, 397) and 2) mean annual precipitation (MAP, 398), which was determined from the chemical index of alteration minus potassium (CIA-K, 413). The soil-order based S(z) values are similar to the smallest S(z) values estimated from MAP and therefore the difference between the two CO₂ estimates for each paleosol increases with increasing MAP. This discrepancy could result from actual sensitivity of S(z) to MAP that is not recorded by soil order and/or it could result from extrapolation beyond the S(z)-MAP calibration curve (398). Importantly, for more than half of the paleosols for which the comparison was made there is no overlap of 97.5 and 2.5 percentile error bars. Although agreement between the two proxies is somewhat better during the Miocene (399), we conclude that the error associated with S(z) is semi-quantified by soil order and MAP-based proxies and therefore place paleosol records based on these S(z) proxies in Category 2.

Several older records had already been updated in the peer-reviewed literature. Specifically, the uncertainty quantification for Cotton and Sheldon (398) was updated by Breecker and Retallack (399) and the record originally published by Da et al. (405) is superseded by Da et al. (36). We also recalculated the original paleo-CO₂ estimates published by Ji et al. (35) and Breecker and Retallack (399) to provide 97.5 and 2.5 percentile values for CO₂. Records originally published by Hyland & Sheldon (42) and Hyland et al. (37) were also recalculated. In particular, Hyland et al. (42) determined temperature from running means of paleosol carbonate $\delta^{18}\text{O}$ values. In our recalculation, we replaced the running means by averaging $\delta^{18}\text{O}$ values from the specific paleosol of interest. Both records were also recalculated using the computer program PBUQ (26), which involves updated calculation of $\delta^{13}\text{C}_r$ from $\delta^{13}\text{C}$ of bulk paleosol organic matter, calculation of calcium carbonate formation temperatures from mean annual temperatures, and an updated regression approach for calculating mean annual precipitation from a commonly employed weathering index (CIA-K, for the original regression see 413). [Return to Error! Reference source not found.](#)[Error! Reference source not found.](#)**Table S2.**

7.3. Future directions

The largest source of error in atmospheric CO₂ reconstructed from paleosol carbonates is associated with the estimation of S(z) (26). Disentangling secular changes in soil respiration rates from changes in atmospheric CO₂ levels requires an independent proxy for soil CO₂ and/or pH (414). New calibrations for estimating S(z) from magnetic susceptibility (36) might be possible for regions outside of the Chinese Loess Plateau with different soil parent material, and several groups are currently working on developing new proxies for quantifying the respiratory contribution to soil CO₂. Alternatively, Eq. 7.1 can be solved for S(z) and measurements in paleosols can then be used with CO₂ determined from other proxies to reconstruct changes in soil respiration (e.g., 415, 416-418). Ultimately, inversion of forward, process-based models that relate the various measurable quantities in paleosols may be the most useful approach to determining environmental changes that are consistent with all the observations.

Whereas improved precision of $S(z)$ determinations is the single most important direction for the improvement of paleosol carbonate-based CO_2 reconstructions, there are other directions that might also be fruitful to pursue. The use of leaf wax $\delta^{13}\text{C}$ values in addition to bulk soil organic matter as a proxy for respired $\delta^{13}\text{C}_{\text{CO}_2}$ would avoid uncertainty associated with decomposition because it would provide insight into paleo-soil carbon cycling. While $\delta^{13}\text{C}_r$ is currently the second largest contributor to the uncertainty of paleo- CO_2 estimates from the paleosol proxy, it could become the largest source of error if $S(z)$ estimates are improved. In comparison, $\delta^{13}\text{C}_a$ is generally less important than $\delta^{13}\text{C}_r$ for paleosol CO_2 estimates, but a high-resolution record of atmospheric $\delta^{13}\text{C}_{\text{CO}_2}$ for the Mesozoic (similar to this recent example for the Cretaceous, 419) and Paleozoic would certainly improve all proxies that rely on this constraint.

The Loess-Paleosol sequence and the underlying Red Clay on the Chinese Loess Plateau is a promising target for future application of the paleosol carbonate proxy (e.g., 35, 36, 405). The abundant calcic paleosols, good exposure and uniformity of soil parent material through space and time in this region should allow for continuous, high resolution CO_2 records spanning much of the Neogene, including replication across paleoenvironmental gradients. [Return to Error! Reference source not found.](#)[Error! Reference source not found.](#) **Table S2.**

8. Nahcolite

8.1. Current understanding of the nahcolite/trona proxy and recent advances

Eugster (420) first proposed that estimates of paleo- CO_2 could be made from the sodium carbonate minerals (nahcolite/trona) formed in ancient saline alkaline lakes. The amount of dissolved carbonate and other constituents in a paleolake, the temperature, and the concentration of atmospheric CO_2 in equilibrium with surface brines control which sodium carbonate mineral forms. The nahcolite/trona proxy was reexamined by Lowenstein and Demicco (28), who proposed that the layered nahcolite deposits in the early Eocene Green River Formation, USA, indicate elevated paleo- CO_2 during a well-recognized warm period, the early Eocene climatic optimum (EECO). The nahcolite/trona proxy has since been improved by experiments using seeded reactants and known CO_2 concentrations, which revised the sodium carbonate mineral equilibria (trona, nahcolite, and a third sodium carbonate, natron) as a function of $p\text{CO}_2$ and temperature (27). That work constrained the position of the triple point in $p\text{CO}_2$ - temperature space and defined the minimum atmospheric $p\text{CO}_2$ at which nahcolite can form. New modeling of the temperatures and $p\text{CO}_2$ involved in precipitation of layered nahcolite and halite in the Eocene Piceance Creek Basin, Green River Formation, includes coupled summer-winter fluctuations in temperature and variations in total dissolved CO_2 in different parts of the paleolake (421). That work confirms that elevated $p\text{CO}_2$ was needed to form nahcolite during the EECO and that paleolake water temperatures in the Green River basin were high, similar to those of the modern Dead Sea. [Return to Error! Reference source not found.](#)[Error! Reference source not found.](#) **Table S2.**

8.2. Criteria for vetting nahcolite/trona proxy data and data revisions

The nahcolite/trona proxy requires petrographic study of the sodium carbonate minerals under consideration to ensure that they formed at the surface (air-water interface) of a saline alkaline

paleolake and not during burial. The paleo-CO₂ estimates of Lowenstein and Demicco (28) have been superseded by Jagiecki et al. (27) using their experimental constraints on the nahcolite-trona phase boundary and the nahcolite-trona-natron triple point in pCO₂ - temperature space. Depending on whether the brines contained NaCl and using a possible precipitation temperature range of 19.5-28°C, the lower limit of atmospheric paleo-CO₂ from these minerals can be constrained to 640-1260 μatm. The upper limit of nahcolite precipitation cannot be determined from the nahcolite proxy. In contrast, trona forms at lower pCO₂ than nahcolite and its occurrence in an ancient lake deposit can therefore establish an upper limit of paleo-CO₂. However, because conditions to precipitate trona occur almost throughout the entire Cenozoic, the presence of trona has less value in paleobarometry than the presence of nahcolite. We therefore follow Jagiecki et al. (27) and eliminate the trona-based paleo-CO₂ estimates of Lowenstein and Demicco (28) from the vetted paleo-CO₂ compilation. [Return to Error! Reference source not found.](#)[Error! Reference source not found.](#)**Table S2.**

8.3. Future directions

Paleo-CO₂ estimates of the nahcolite/trona proxy could be improved with the availability of independent data on the lake brine temperatures at which sodium carbonate minerals precipitated, e.g., based on clumped isotopes or the newly developed Brillouin thermometry, which uses femtosecond laser technology for nucleating vapor bubbles in evaporites (422). In addition, and although limited in number, there are additional trona/nahcolite lake deposits that have not yet been explored for their suitability as paleo-CO₂ indicators, most notably the late Eocene Anpeng and Wucheng deposits of Henan province, China. Finally, the pCO₂ in modern saline lakes is poorly known, but in some cases, is higher than in the atmosphere (423, 424). Understanding the reasons for this air-water disequilibrium and hindcasting such conditions for ancient lakes requires additional limnologic study of modern saline alkaline lakes. [Return to Error! Reference source not found.](#)[Error! Reference source not found.](#)**Table S2.**

9. Approximated sample age uncertainty for marine paleo-CO₂ records

Unlike terrestrial records, most publications based on marine sediment records do not estimate or report the age uncertainty. This is a problem that needs to be addressed systematically in the future. If not assessed by the original publications, we use sample ages as reported in the most recent publications and estimate the age uncertainty across marine-sediment-based datasets with a unified approach. We base the estimates on a power-law fit to the uncertainty reported in the LR04 benthic stack (425) (0 to 5.3 Ma, **Table 3**), extrapolated over the Cenozoic (Fig. S7). The larger of the power-law fit and the LR04 uncertainties is used. The uncertainties are treated as 1-sigma uniform distributions that are incorporated into the calculation of the Cenozoic CO₂ curve.

The approach used here ensures that comparisons of data from different sites include a reasonable estimate for the uncertainty in their age alignment. Within a site, however, the age uncertainty is applied to all samples such that their stratigraphic ordering and relative spacing are not affected. The true age uncertainty of individual datasets may differ from our simplified

approach, however, the lack of a uniform approach to these uncertainties in the literature precludes an individualized approach. Future CO₂ (and really all paleoceanographic) datasets will greatly benefit from projects that provide robust, traceable, and updateable age estimates and uncertainties.

10. Cenozoic CO₂ model

We adapt the Joint Proxy Inversion framework of Bowen et al. (112) to estimate the evolution of Cenozoic CO₂ as constrained by the compiled Category 1 proxy data. The model code has been published (426). This approach uses inversion of a 2-level Bayesian hierarchical model via Markov Chain Monte Carlo sampling (MCMC) to obtain posterior samples of all model parameters, including paleoenvironmental timeseries. In this case, the first (process) model level represents atmospheric CO₂ levels throughout the Cenozoic, and the second (data) model level represents the relationship between the paleo-CO₂ record and the proxy data compiled here.

Our process model simulates natural log-transformed global atmospheric CO₂ concentrations (C) at 500-kyr time steps from 67 Ma to present (see Fig. S8 for the number of data and proxies in each timestep) using an autocorrelated random walk model, where:

$$C(t) = C(t - 1) + \epsilon(t), \text{ and} \quad (\text{Eq. 10.1})$$

$$\epsilon(t) \sim N[\epsilon(t - 1) * \phi, \tau_\epsilon]. \quad (\text{Eq. 10.2})$$

Here, ϵ is the time-dependent error term (change in C between timesteps). This model has four free parameters: the initial conditions $C(1)$ and $\epsilon(1)$ and error autocorrelation (ϕ) and precision (τ_ϵ , where precision = variance⁻¹). We specify prior distributions for each of these parameters as:

$$\phi \sim U[0.01, 0.99], \quad (\text{Eq. 10.3})$$

$$\tau_\epsilon \sim \Gamma[1, 0.1], \quad (\text{Eq. 10.4})$$

$$C(1) \sim U[6, 8], \text{ and} \quad (\text{Eq. 10.5})$$

$$\epsilon(1) \sim N[0, \tau_\epsilon]. \quad (\text{Eq. 10.6})$$

The error autocorrelation term governs the ‘stiffness’ of the CO₂ timeseries, leading to greater smoothing of the reconstruction and emphasizing long-term trends at the expense of high-frequency change. Although the importance of long-term (multi-Myr) forcing related to tectonic and biological change as a driver of Cenozoic CO₂ is generally accepted (427-429), we also expect important short-term (multi-kyr) events to be expressed in the data. As a result, we adopt a minimally-prescriptive uniform distribution as the prior of the autocorrelation parameter ϕ , allowing this parameter to be optimized to fit the proxy estimates. Error precision defines the distribution of possible values for CO₂ change between adjacent timesteps. We use a broad gamma distribution with a mean that corresponds approximately to a standard deviation of 0.5 for the error term but allows for a broad range of possible values for this parameter. After burn-in the model is minimally sensitive to the priors on $C(1)$ and $\epsilon(1)$, and our choices here are

intended to encompass a range of potential values for late Cretaceous CO₂ and possible trajectories for late Cretaceous CO₂ change, respectively.

We incorporate a simple treatment of proxy age uncertainty and local (in space and time) variability to estimate the CO₂ value ‘experienced’ by each proxy record i (C_i). Age uncertainties can be decomposed into two components: uncertainty associated with the absolute age constraints on a given stratigraphic section or drill hole (‘locality’), and those associated with the relative age offset between a sample and the within-section constraints (e.g., due to variations in sediment accumulation rate). Because the age data compiled in our database do not provide a basis for separating these two components, our analysis assumes that the majority of the age uncertainties affecting the samples is associated with the first component and keeps the relative age differences between data from a single locality fixed. We further assume that CO₂ differences between the local, short-term conditions reflected in a given proxy datum and the long-term mean condition modeled by equation 10.1 is drawn from a zero-centered normal distribution with precision τ_i . Thus, for proxy datum i obtained from locality j :

$$C_i \sim N \left[C \left(t(a_i + e_j) \right), \tau_i \right], \text{ where} \quad (\text{Eq. 10.7})$$

$$e_j \sim N[0, s_j], \text{ and} \quad (\text{Eq. 10.8})$$

$$\tau_i \sim \Gamma[2, 0.1]. \quad (\text{Eq. 10.9})$$

Here, a_i is the mean age estimate for the proxy datum and s_j is the average reported age uncertainty (1 standard deviation) for all data associated with locality j . The numeric ages are converted to integers ($t = 1, 2, \dots$) that correspond to the process model timesteps within which the ages fall.

In lieu of formal proxy system modeling, our data model uses the interpreted CO₂ reconstructions (and their associated uncertainties) developed by the proxy system working groups. In most cases and for most proxies the upper and lower error estimates are consistent with a log-normally distributed uncertainty, and all values were transformed to $\ln(\text{CO}_2)$ and used to prescribe a mean estimate (c) and standard deviation (σ , calculated as the half-range of the 5% and 95% confidence intervals / 1.96) for each proxy datum. The likelihood of each observed proxy value c_i is then evaluated relative to the modeled local CO₂ value according to:

$$c_i \sim N[C_i, \sigma_i], \quad (\text{Eq. 10.10})$$

and the joint likelihood of all proxy data can be calculated for any model state.

We conducted Markov Chain Monte Carlo sampling of the model using the JAGS (Just Another Gibbs Sampler) program (430) called from R v4.2.3 (431) using the rjags and R2jags packages (432, 433). A total of 500,000 posterior samples were obtained in each of 4 chains, including a burn-in period of 50,000 samples; the burn-in samples were discarded and the remaining samples were thinned to retain 2,500 samples per chain. Stability and convergence were assessed using trace plots, effective sample size (N_{eff}), and the Gelman and Rubin convergence diagnostic (\hat{R}) (434). Values of $\hat{R} < 1.1$ and $N_{eff} \geq 50$ were achieved for all parameters and CO₂ nodes except for the earliest model time steps (representing ages older than the oldest proxy

data); values of $\hat{R} < 1.03$ and $N_{eff} \geq 100$ were typical for the CO₂ nodes at most time steps, suggesting strong convergence.

We conducted an independent analysis of global mean surface temperature (GMST) estimates from Westerhold et al. (43), calculated after Hansen et al. (44). The model form is identical to that described above with the exception that no age model uncertainty was incorporated and that local deviations from the long-term mean were not treated independently from proxy uncertainty (see below). This lack of consideration of age uncertainties is reasonable given that the data come from a limited number of astronomically-tuned deep sea sediment cores and the age uncertainties of individual data are likely to be trivial relative to the 0.5-Myr model time step. Priors on the model parameters were the same as those shown above, with the exception of the error precision and temperature initial value, which were scaled appropriately for the target variable (GMST, expressed as difference relative to the preindustrial value of 14.15, in °C):

$$\tau_{\epsilon} \sim \Gamma[2,2], \quad (\text{Eq. 10.11})$$

$$GMST(1) \sim U[5,15]. \quad (\text{Eq. 10.12})$$

No quantitative estimate of the uncertainty of the individual proxy temperature estimates was provided by the original authors, and for the purpose of our analysis we adopt a normally distributed (and independent) uncertainty with a standard deviation of 4 °C on all data. This value is about an order of magnitude greater than the uncertainty of the species-specific calibration relationships linking temperature and foraminiferal $\delta^{18}\text{O}$ (435), and is intended to encompass calibration uncertainty, variability in deep-water temperatures over timescales less than the modeled time resolution, and uncertainties in translating the deep-ocean temperatures to GMST. Because the underlying drivers of these uncertainties are generally related to slow and gradual changes in the ocean and climate systems, we suggest that inaccuracies in the corrections are unlikely to substantially affect reconstructed shorter-term (e.g., up to ~10 Myr) changes in GMST, but they may impart some bias to comparisons made across longer time scales. A model that assumes independent errors (such as that used here) cannot account for these potential biases, and our assumed error model is intended only to provide a conservative estimate of the individual temperature estimate generated under the assumptions of the Westerhold et al. (43) analysis.

The temperature model achieved satisfactory convergence with 4 chains of 12,000 samples, including a burn-in of 2,000 samples, and the posterior was thinned to retain 2,500 samples per chain. This produced $\hat{R} < 1.02$ and an effective sample size ≥ 180 for all model parameters and temperature values, with the exception of temperature values at the first several model time steps (prior to the first data) and a single time step at 36.25 Ma which exhibits slightly poorer convergence ($\hat{R} = 1.03$, $N_{eff} = 110$).

10.1. Comparison of data subsets and alternative temporal resolutions

As described and justified here and in the main text, we focus on reconstructing the Cenozoic CO₂ record at a 500-kyr temporal resolution using all available Category 1 data. We also present alternative reconstructions at coarser (1-Myr) and finer (100-kyr) resolutions for comparison with our primary analysis (Fig. S9). The features of these curves are quite similar to those of the 500-kyr curve, but the 1-Myr curve mutes and the 100-kyr curve amplifies the expression of short-

term features. The higher-resolution reconstruction may better capture real and meaningful features in some cases (e.g., the PETM, Eocene-Oligocene, Plio-Pleistocene); whereas it accentuates questionable features driven by anomalous or unevenly distributed data (e.g., late Paleocene).

To evaluate the impact of the relatively sparse terrestrial proxy data on the reconstruction, we generated an alternative reconstruction using only boron and alkenone isotope proxy data (Fig. S10). Comparison with the full reconstruction highlights two points. First, during intervals of the Cenozoic when marine proxy data are sparse (most notably the Paleocene) the non-marine records substantially influence the reconstruction. During the Paleocene in particular, the results of the full analysis suggest a decline in CO₂ that is consistent with reconstructed temperature records but is necessarily absent in the curve generated using only marine proxy data. This is because to date, marine proxy data have only been generated for the K/Pg (234) and PETM (60), and the lack of marine estimates across the Paleocene leads to connecting distant events and erroneously suggesting elevated CO₂ for the duration of the Paleocene (see also 34). Second, throughout most of the Cenozoic the inclusion of terrestrial proxy records only subtly changes the reconstruction, implying broad consistency between proxy types and increasing confidence in the reconstruction. The differences in Fig. S10 underscore the need to fill in data gaps using both terrestrial and marine proxies.

10.2. When was the last time CO₂ was as high as today?

Using the full posterior suite of 10,000 Cenozoic CO₂ curves from this analysis, we compare the reconstructed values to the average atmospheric CO₂ levels measured in 2022 at the Mauna Loa observatory (419 ppm, 3) to determine the most recent time in Earth's history that long-term (500-kyr) average CO₂ levels exceeded the current value (Fig. S11). At each timestep in the reconstruction, the probability that atmospheric CO₂ concentrations had exceeded the current level was calculated as the fraction of the reconstructed curves that exceeded 419 ppm at one or more points between that timestep and the present. Using the calibrated language adopted by the IPCC AR6 (2), we find that it is exceptionally unlikely (<0.1% chance) that 500-kyr mean CO₂ values exceeded the current atmospheric concentration at any point in the past 8 million years. This probability rises to 5% by 9 Ma, but it remains very unlikely (<10% chance) that long-term mean CO₂ levels ever exceeded the modern value since the middle Miocene (14 Ma). Reconstructed paleo-CO₂ decreases sharply between 15 and 14 Ma, such that it is likely (>66% chance) that 500-kyr mean values exceeded the modern value at some time between 15 Ma and present.

Fluctuations in atmospheric CO₂ levels, for example those associated with glacial cycles, may have caused paleo-CO₂ levels to briefly exceed the modern concentration more recently than indicated in Fig. S11. To address this issue, we conducted a second analysis in which we used the ensemble of reconstructed CO₂ curves to assess the probability that the change in CO₂ concentration relative to the curve's modern endpoint (representing the mean of the past 500 kyr) had exceeded the change between pre-industrial (i.e., 280 ppm, 436) and current values (Fig. S12). Because the pre-industrial baseline represents peak interglacial conditions, this analysis should conservatively account for short-term CO₂ variations associated with glacial cycles as long as 1) the amplitude of these cycles in the Miocene and Pliocene did not exceed that of the late

Pleistocene cycles (as suggested, e.g., by proxies for ice volume, 437), and 2) there is no sampling bias towards glacial or interglacial extrema in our proxy records. This analysis suggests that it is exceptionally unlikely that short-term transient CO₂ values exceeded the modern value at any time in the past 4.5 million years, and very unlikely that this situation occurred within the past 7 million years. Short-term CO₂ values exceeding modern remain unlikely (<33% chance) until 9 Ma. However, it is very likely (>90% chance) that transient CO₂ values exceeding the modern value have occurred during the past 14.5 million years.

10.3. Comparison with CO₂ estimates from Hansen et al. (44)

We compare the Paleocene-Eocene reconstruction with estimates of CO₂ generated under the assumption that 1) benthic $\delta^{18}\text{O}$ values reflect global surface temperature change over this interval, and 2) temperature change results entirely from direct and indirect radiative forcing from CO₂ and linearly increasing solar luminosity (44). Throughout most of this interval the proxy-reconstructed values are broadly compatible with the temperature-inferred values estimated using state-dependent climate sensitivity, but the two estimates diverge during the late Eocene (Fig. S13). This is because our proxy estimates suggest that during the cooling leading into the Eocene Oligocene Boundary, CO₂ values declined more slowly than inferred from the temperature proxy data.

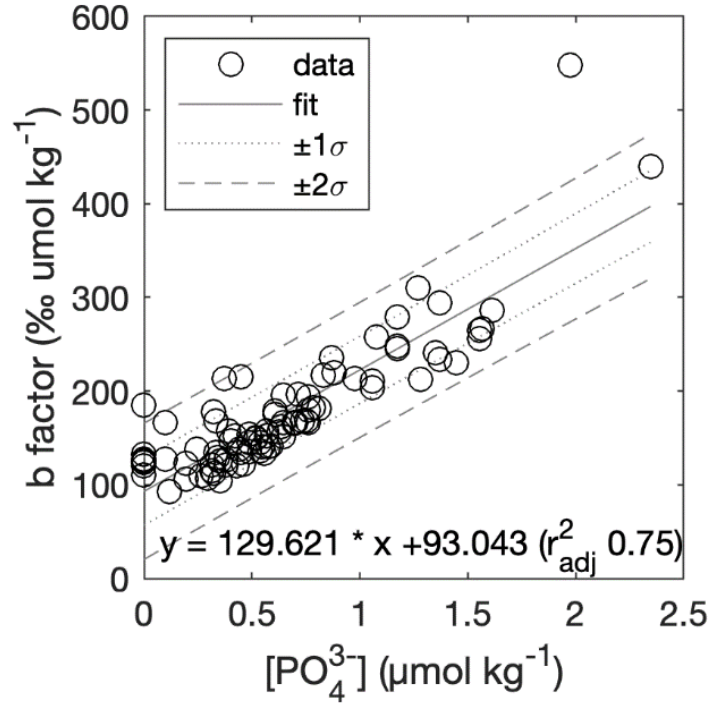


Figure S1: Relationship between phosphate and b in photic zone samples. Data are from the compilation of Hernández-Almeida et al. (144). One- and two-sigma confidence bounds are the prediction uncertainty on b that includes both the parameter uncertainty and the data uncertainty in the regression. Note that phosphate values at zero are from Bidigare et al. (139) where phosphate was measured as zero with a detection limit of $0.03 \mu\text{mol/kg}$.

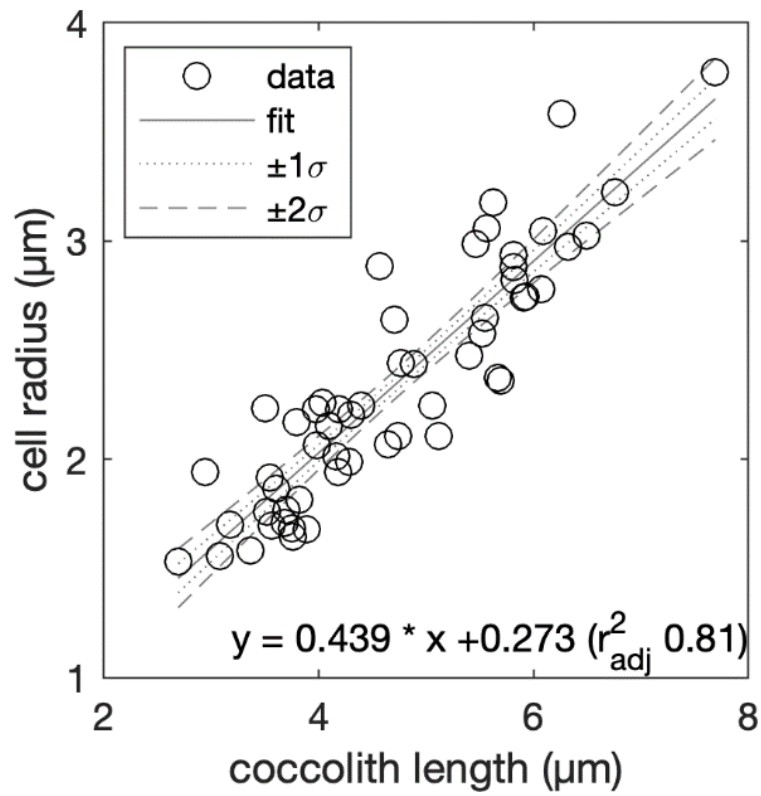


Figure S2: Relationship of coccolith length and cell radius determined from intact individual coccospheres in Cenozoic sediments (after 38). Confidence bounds are the prediction uncertainty on cell radius that includes only the parameter uncertainty.

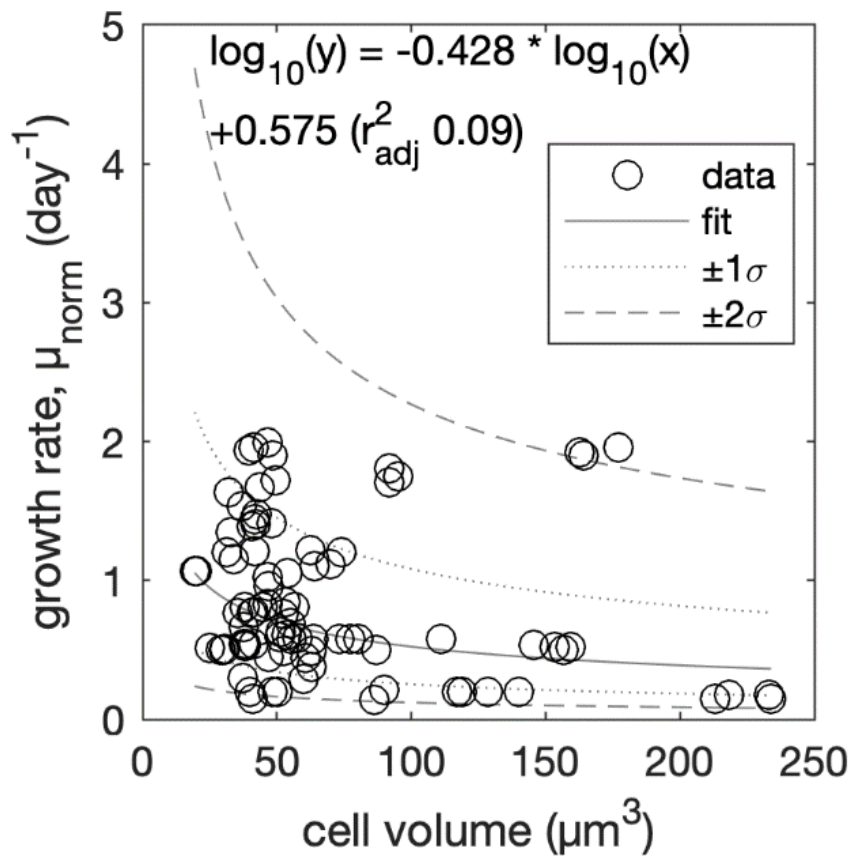


Figure S3: Relationship between cell volume and the logarithm of instantaneous (or normalized) growth rate using data from Aloisi (157) as described in Zhang et al. (41). One- and two-sigma confidence bounds are the prediction uncertainty on growth rate that includes both the parameter uncertainty and the data uncertainty in the regression.

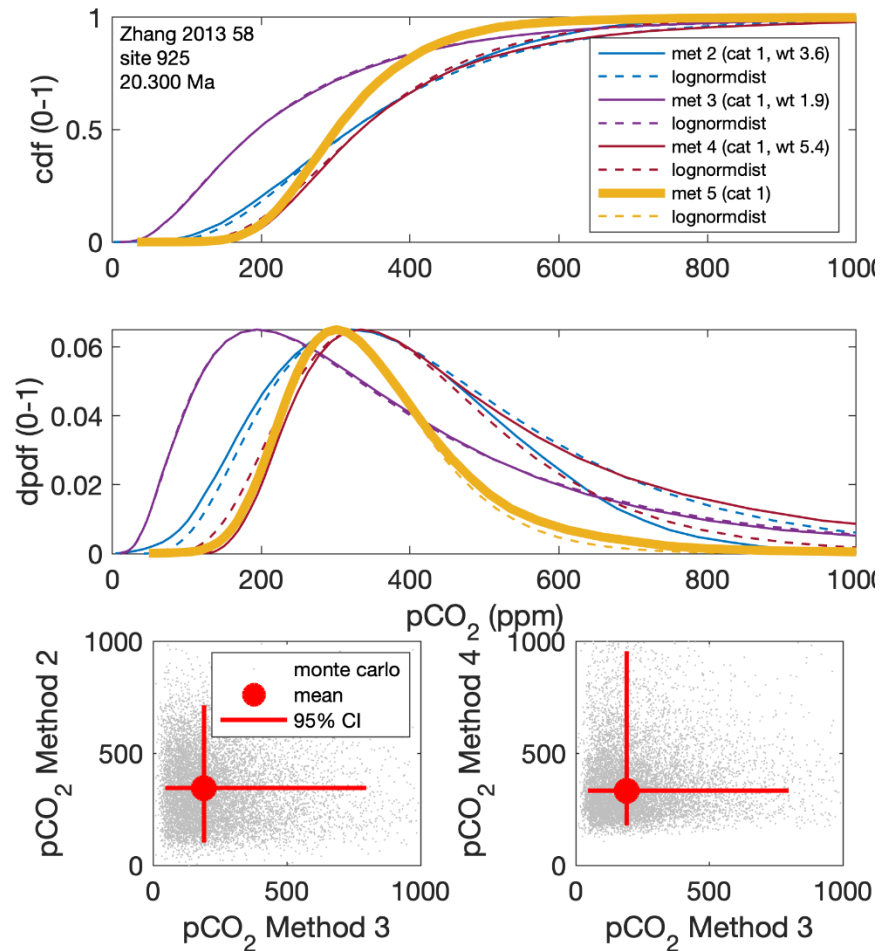


Figure S4: Monte-Carlo pCO_2 distributions from Methods 2 to 4 for a single sample. **Top and middle:** Cumulative and discrete probability distribution functions for a sample from ODP site 925 (108) illustrating the close approximation of a log-normal distribution (dashed lines) to the Monte-Carlo data (solid lines). 'Method 5' is the inverse-weighted mean as described in the text (weights stated in the legend). **Bottom, left and right:** Monte-Carlo estimates from different methods applied to the same sample (gray dots) with the mean and 95% confidence interval for each method shown in red. The scattered relationship of the Monte Carlo estimates indicates that the different methods are largely independent of each other.

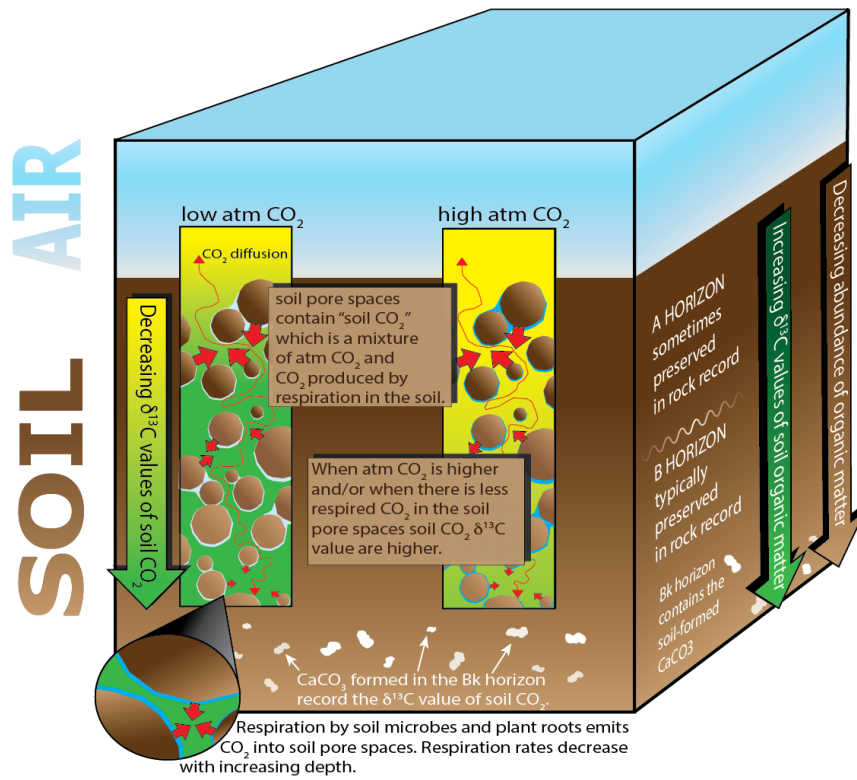


Figure S5: Schematic illustration of processes and gradients relevant to the paleosol carbonate paleo-CO₂ proxy.

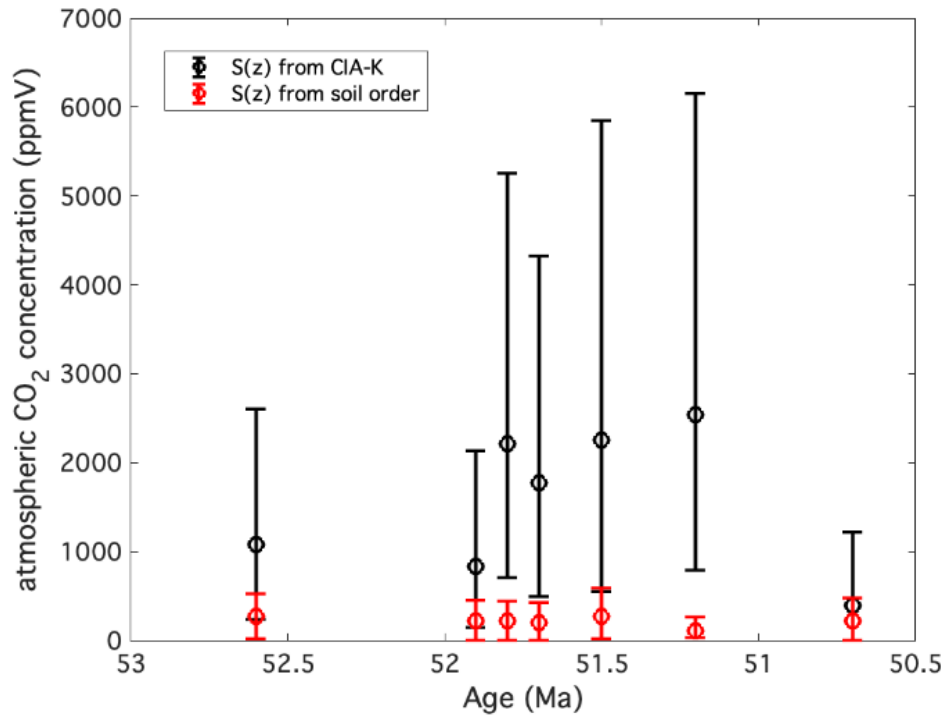


Figure S6:

Comparison of paleo-CO₂ estimates made with the paleosol proxy. The estimates use two different methods to determine $S(z)$ from the same paleosols. The first (black symbols) determines mean annual precipitation (MAP) from CIA-K (413) and then infers $S(z)$ from MAP (398). The second method (red symbols) estimates $S(z)$ from soil order (26, 397). Error bars extend to 2.5 and 97.5 percentiles and were calculated using PBUQ (26). Minimal overlap between estimates from the same soil data suggests that $S(z)$ proxies are not fully quantified, which leads us to categorize most paleosol-based CO₂ estimates as Category 2. Data used for this example are from Hyland and Sheldon (42) and Hyland et al. (37).

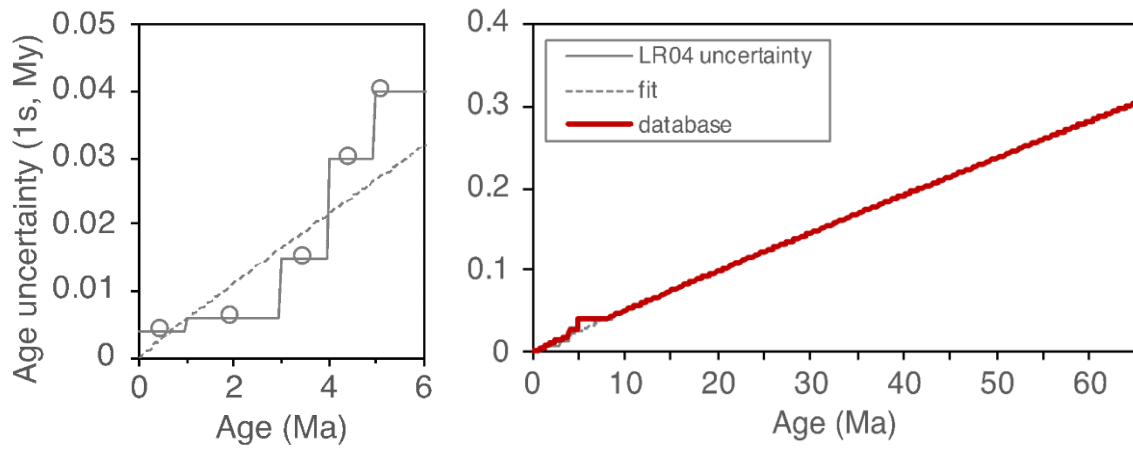


Figure S7: Left: The age uncertainty of the LR04 dataset fit with a power law equation ($y = 5.82E-03x^{9.48E-01}$). **Right:** The uncertainty applied to samples in the database from the larger of the LR04 uncertainty and power law fit.

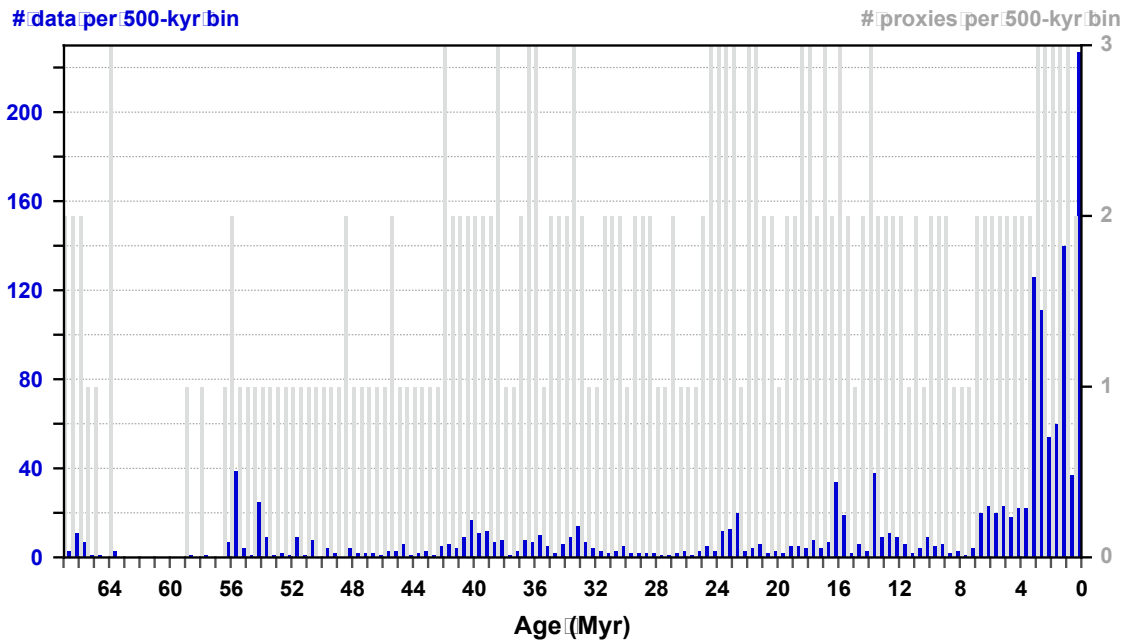


Figure S8: The number of Category-1 paleo-CO₂ estimates (blue) and proxies (grey) in each 500-kyr time step. See Fig. 1a for the proxies applied in each timestep.

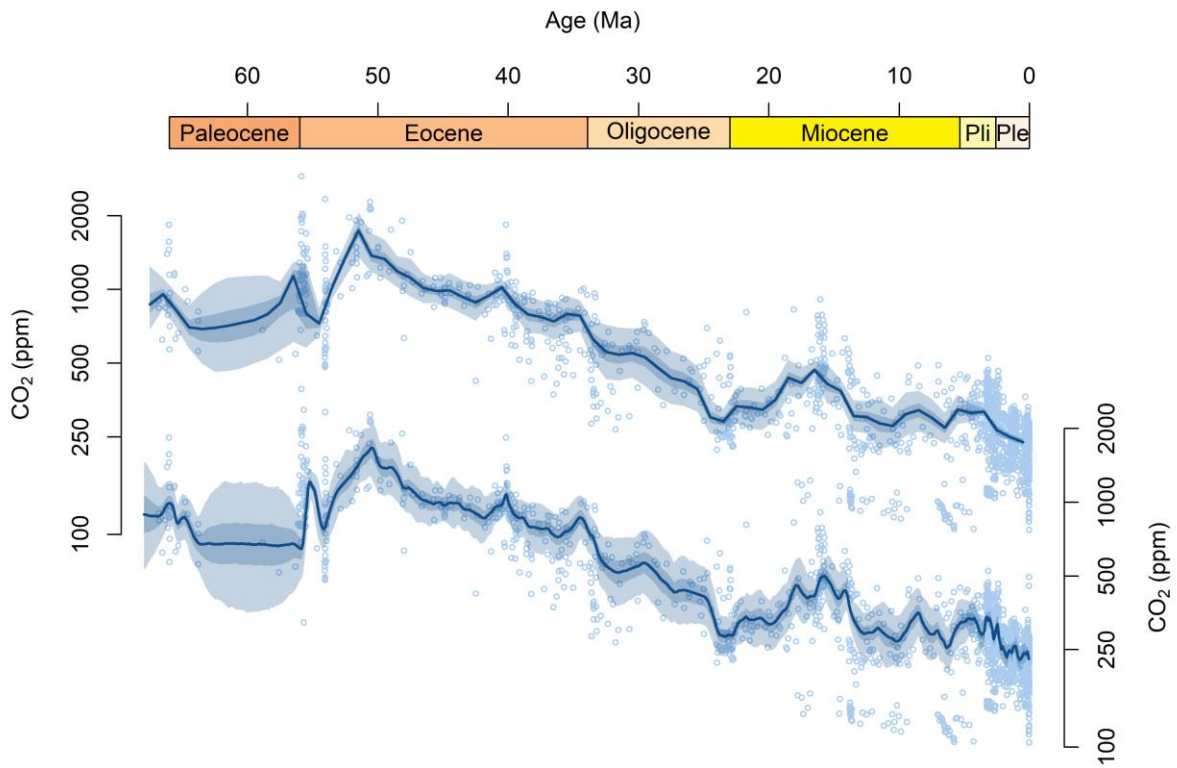


Fig. S9: Alternative Cenozoic CO₂ curves showing reconstructed mean values at 1-Myr (top) and 100-kyr (bottom) intervals.

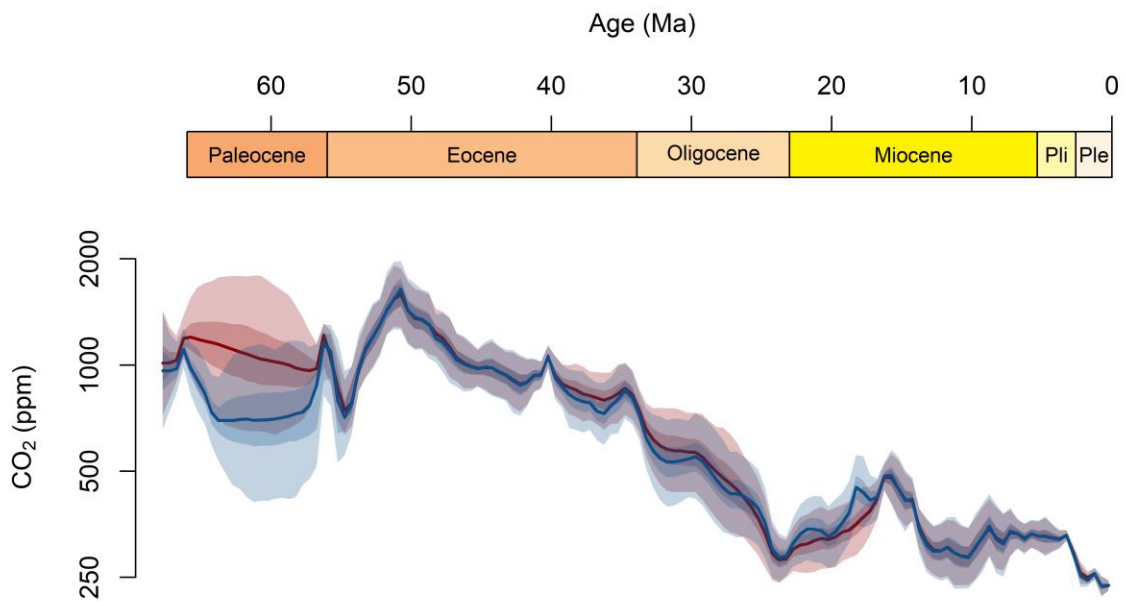


Figure S10: Comparison of 500-kyr average CO₂ reconstructions produced using all proxy data (blue) or only boron and alkenone isotope proxies (red).

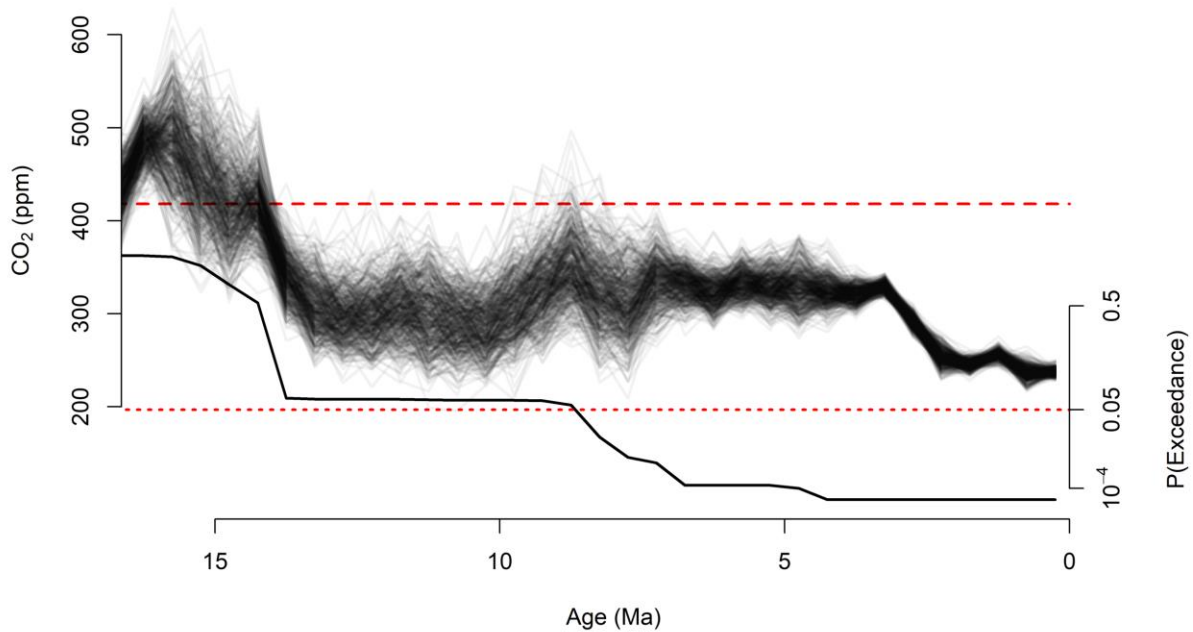


Fig. S11: Comparison of a representative sample of modeled CO₂ curves (thin black lines, top panel) with modern atmospheric CO₂ of 419 ppm (red dashed line, 3). The bottom panel shows the probability of long-term (500-kyr mean) CO₂ having exceeded the modern value at any time between the plotted time point and the modern based on all 10,000 curves retained in the analysis; dotted red line shows a probability of 5%. The last time this probability was greater than 50% was in the 14.5-14 Ma bin. Note the nonlinear probability scale in the bottom panel.

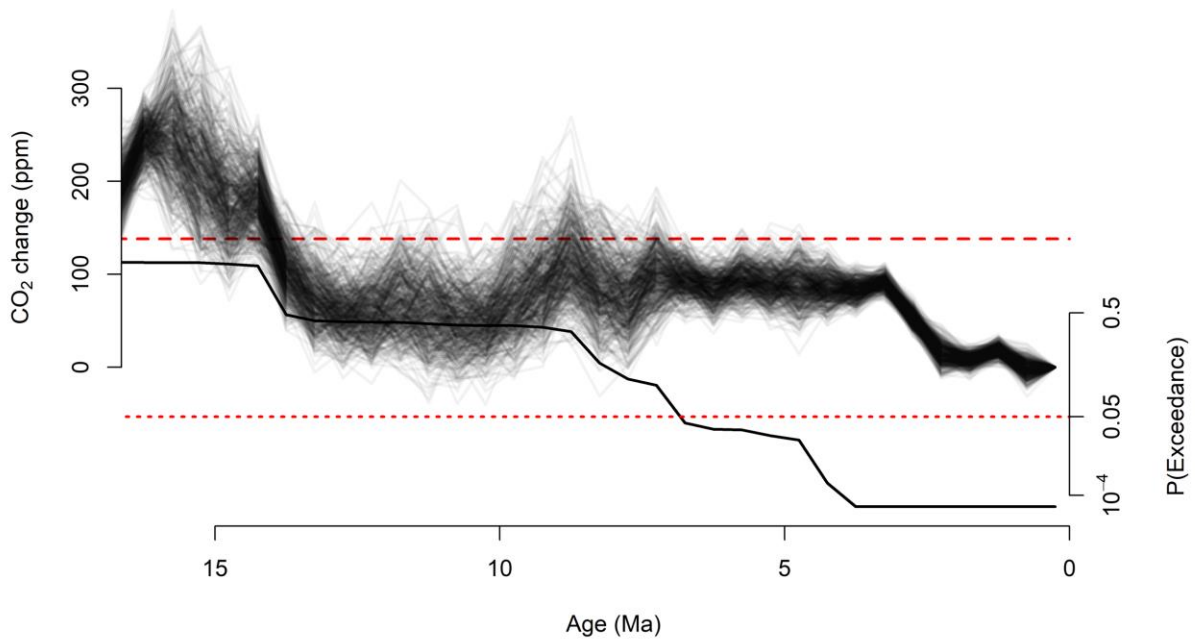


Fig. S12: Comparison of reconstructed CO₂ change relative to the 0.5-0 Ma reference period with CO₂ change between pre-industrial and current values (i.e., 419-280 =139 ppm; red dashed line). The bottom panel shows the probability of long-term (500-kyr mean) CO₂ change having exceeded the post-industrial, anthropogenic change. The thick black line (bottom panel) represents the probability that short-term CO₂ levels exceeded the current value at any time between the plotted time point and the modern, based on all 10,000 curves retained in the analysis. The dotted red line shows a probability of 5%. The last time this probability was greater than 50% was again in the 14.5-14 Ma bin. Note the nonlinear probability scale in the bottom panel.

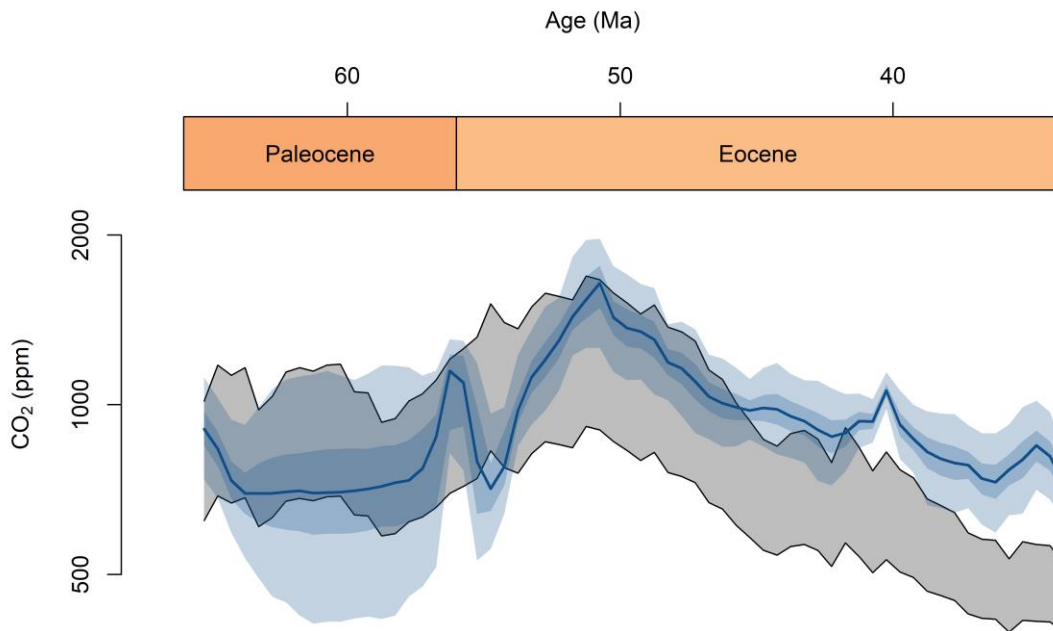


Fig. S13: Paleocene and Eocene CO₂ values from our proxy reconstruction (blue) and from the analysis of Hansen et al. (grey, 44). The grey envelope encompasses estimates made assuming state-dependent sensitivity to CO₂ forcing (full and 2/3 of the sensitivity calculated using the Russell model) and a surface temperature of 28°C during the Early Eocene Climatic Optimum.

Table S1. Proxy-specific vetting criteria for paleo-CO₂ data categorization.

Data Category	Phytoplankton	Boron Proxies	Stomatal Frequencies, Leaf Gas Exchange Proxies, and Liverworts	Land Plant $\delta^{13}\text{C}$	Paleosols	Nahcolite/ Trona
1	All known sources of error have been quantified and/or sensitivity of the CO ₂ estimate to those sources is small.					
2	<p>(1) Samples that include all of the data needed to quantify pCO₂ but [CO₂]_{aq} falls outside the calibration range. That range differs between approaches used to calculate pCO₂. In the approach where b is calculated from PO₄, the range is from the minimum and maximum [CO₂]_{aq} in the b-PO₄ calibration dataset. In the approach where CO₂ is calculated from the relative change in ϵ_p anchored to Pleistocene glacial-interglacial samples, the range is from the minimum and maximum [CO₂]_{aq} values in the laboratory culture experiment that form the calibration dataset. (2) Samples where the organisms contributing to the algal carbon $\delta^{13}\text{C}$ value are unknown (e.g., bulk marine organic carbon or biomarkers that lack taxonomic specificity, such as phytol and phytane).</p>	<p>A record that is fully quantified but where estimation of both pH and the second parameter of the marine carbonate system required for estimating CO₂ are not fully independent because both are based on $\delta^{11}\text{B}_c$.</p>	<p>(1) All single-species records based on <5 cuticle fragments, unless a statistical analysis shows that fewer than 5 is acceptable. (2) All stomatal ratio records. (3) Estimates based on extrapolation beyond the calibrated range. (4) Estimates whose fossils were also used to estimate CO₂ with leaf gas-exchange methods.</p>	<p>A CO₂ record that is fully quantified but where mean annual precipitation and plant species are not known. As estimates of precipitation and associated uncertainties and plant species become available, the CO₂ record can be better quantified.</p>	<p>CO₂ estimates that satisfy the following three criteria: (1) $\delta^{13}\text{C}$ values of paleosol organic matter (or an alternative proxy for local vegetation, e.g., tooth enamel) used to determine $\delta^{13}\text{C}_r$. (2) paleosol carbonate $\delta^{13}\text{C}$ is sensitive to atmospheric CO₂ level (i.e., $0.3 < \text{CO}_2/\text{S}(z) < 1.8$). (3) S(z) is semi-quantitative (e.g., estimated from soil order- and MAP-based proxies).</p>	<p>Estimates that quantify the lower limit of atmospheric CO₂, but do not suggest a best estimate or upper limit.</p>

Table S1 continued.

Data Category	Phytoplankton	Boron Proxies	Stomatal Frequencies, Leaf Gas Exchange Proxies, and Liverworts	Land Plant $\delta^{13}\text{C}$	Paleosols	Nahcolite/Trona
3	<p>(1) Samples that are superseded by newer studies where additional or better information was added. For example, alkenone samples where a subsequent study added coccolith size information or improved SST estimates.</p> <p>(2) Samples where measurements of other input variables have subsequently been shown to be in error.</p>	<p>(1) Records that are superseded by improved calculations.</p> <p>(2) Records that applied inadequate cleaning, or used mixed species or morphotypes and/or mixed size fractions.</p> <p>(3) Records based on erroneous proxy theory.</p> <p>(4) Records with inadequate assessment of signal/noise ratio.</p>	<p>(1) All records based on stomatal density.</p> <p>(2) All records based on measurements from published plates.</p> <p>(3) Any record using a transfer function from an extant species that is different from the fossil species, unless broad equivalency in stomatal response can be demonstrated at the genus or family level.</p> <p>(4) Any record whose uncertainties could not be fully propagated in both the calibration function and the fossil measurements (note: we revised estimates using the Beerling et al. (273) method whenever possible).</p> <p>(5) Records that are superseded by newer calculations.</p>	N/A	<p>(1) CO₂ estimates that do not meet criteria for Category 1 and do not meet one or more of the criteria for Category 2.</p> <p>(2) Records that are superseded by newer calculations.</p>	Records based on trona, because conditions to precipitate trona occur almost throughout the entire Cenozoic and the presence of this mineral therefore has little value for paleo-barometry.

Table S2. Guide to Sections 1-8. Click on hyperlinks to access respective paragraphs.

Proxy & variables ¹ for calculations	Current understanding and recent advances	Data vetting criteria	Calculational methods	Future opportunities
			Key structural uncertainties ²	
Phytoplankton (ϵ_P) T, S, $\delta^{13}C_{DIC}$, $\delta^{13}C_{biomass}$, K_H , $[PO_4^{3-}]$, b , coccolith length (L)	Paragraphs 1.1. ; 1.2.1. – 1.2.4. History of the $\epsilon_P = \epsilon_f - b/[CO_2]$ approach; Methods 1, 2, 3, and 4, detailing different approaches to accommodate physiological factors.	Paragraph 1.3. Details for classifying data into Category 1, 2, or 3 (criteria as described in Table S1).	Paragraph 1.4.1. – 1.4.5. Methods 1, 2, 3, and 4, the approaches to estimate b ; calculation of weighted-mean pCO_2 . Paragraph 1.2.5. Role of diffusion vs. CCMs in algal C budgets; variations in Rubisco ϵ_i ; resulting impact on model structure.	Paragraph Return to Error! Reference source not found. Error! Reference source not found. Table S2. 1.5. See text for details.
Boron Isotopes ($\delta^{11}B$) T, S, P, $\delta^{11}B_{sw}$, K_B , K_0 , K_1 , K_2 , K_{HSO_4} , Alk or [DIC] or $\Omega_{calcite}$, species-specific calibration	Paragraph 2.1. Background and theory for boron isotope and B/Ca proxies.	Paragraph 2.2. Description of the few select cases where data were excluded from Category 1.	Paragraph 2.1. Equations for translating $\delta^{11}B_{CaCO_3}$ to pH. Paragraph 2.1.1. Error propagation; the value of $\delta^{11}B_{sw}$; species-specific calibrations; second parameter of the carbonate system.	Paragraph 2.3. New estimates for $\delta^{11}B_{sw}$; physiological work, cross-calibration, and modeling efforts to better understand vital effects; refined approaches to estimate paleo-alkalinity or DIC.
Stomatal Frequencies T, S, leaf area, epidermal cell density	Paragraph 3.1. Background and definitions of stomatal density, index, and ratio, and their empirical calibration.	Paragraph 3.2. Details for classifying data into Category 2 or 3 (criteria as described in Table S1).	See Table 3 of Beerling and Royer (2002) for examples of the taxon-specific empirical approach. Paragraphs 3.1.1. ; 3.2. Statistical simulation of errors; assumption that fossil taxa have same response as plants in the modern calibration.	Paragraph 3.3. Challenges for calibrating fossils to modern sister groups; cross-comparison with estimates of paleo- CO_2 from another proxy of the same age.
Leaf Gas Exchange A_0 , g_{op}/g_{max} (or ζ or s_4), g_m , g_b , other guard cell scalings (s_1 - s_3); $\delta^{13}C$ of atmospheric CO_2 ; leaf T	Paragraph 4.1. Background and description of the two major models for leaf gas-exchange, the Franks model and the Konrad model.	Paragraph 4.2. A description of why all CO_2 estimates presented in Franks et al. (312) were placed in Category 3.	Paragraph 4.1. Diffusion model for leaf gas exchange. Paragraphs 4.1.1. ; 4.3. Uncertainty in photosynthetic rate at a known CO_2 concentration (A_0); operational vs. maximum stomatal conductance to CO_2 (g_{op}/g_{max}); applicability	Paragraph 4.3. Calibrate photosynthetic rate using vein density, process-based ecosystem modelling, or nearest living relative or ecological equivalent; apply post-hoc phylogenetic correction factor for plant

			to non-Angiosperm taxa with large stomata and passive stomate control (resulting in high c_i/c_a).	$\delta^{13}\text{C}$; use an assemblage-based approach to paleo- CO_2 estimation.
--	--	--	---	--

Proxy & variables ¹ for calculations	Current understanding and recent advances	Data vetting criteria	Calculational methods	Future opportunities
			Key structural uncertainties ²	
Liverworts T, O ₂ , irradiance; δ ¹³ C of atmospheric CO ₂ ; RubisCO V _{max} ; dark respiration (R)	Paragraph 5.1. Diffusional model for CO ₂ uptake through fixed pores.	Paragraph Return to Error! Reference source not found. Paragraph Error! Reference source not found. Table S2. 5.2. Explanation for the rarity of liverwort data.	A photosynthesis model (for details, see Fletcher et al., 2006) that requires inputs such as irradiance. Paragraph 5.3. Scarcity of fossils; irradiance through the canopy; accurate δ ¹³ C of local atmospheric CO ₂ .	Paragraph 5.3. Improvements in estimating forest canopy cover (irradiance) using fossil leaves from vascular plants to determine epidermal cell size and sinuosity; focus on liverworts of unshaded habitats; apply a δ ¹³ C correction based on present-day measurements.
Land Plant δ¹³C Calibration parameters A, B, C; δ ¹³ C _{CO2atm} at time t and time 0; δ ¹³ C _{land plant} at time t and time 0	Paragraph 6.1. Summary of approaches using an independent baseline or a proxy-derived baseline; overview of calibrations.	Paragraph Return to Error! Reference source not found. Paragraph Error! Reference source not found. Table S2. 6.2. Baseline dependence of calculated result justifies inclusion in Category 2.	see Cui and Schubert (365) Paragraph 6.1. Uncertainties in the applicable baseline CO ₂ value (for deep time); different responses between evolutionary groups; very large changes in Δδ ¹³ C can result in negative CO ₂ estimates.	Paragraph Return to Error! Reference source not found. Paragraph Error! Reference source not found. Table S2. 6.3. Additional work needed on moisture effect; cross-group calibrations (pteridophytes, angiosperms and gymnosperms); expanded geographical area for calibrations.
Paleosols S(z); δ ¹³ C _r , soil-respired CO ₂ ; δ ¹³ C _a , atmospheric CO ₂ , in-situ T	Paragraph 7.1. Background on soil carbonate formation from mixed respiratory CO ₂ and atmospheric CO ₂ in soil pore environment.	Paragraph Return to Error! Reference source not found. Paragraph Error! Reference source not found. Table S2. 7.2. Criteria for classification based on estimated CO ₂ /S(z) ratio and on which proxies were used for carbon isotope	Paragraph 7.1. Eq. 7.1, Eq. 7.2; Sensitivity relationship between proxy response and CO ₂ /S(z) ratio. Paragraph 7.3. Largest error is estimation of S(z), the soil respiration contribution and sensitivity of CO ₂ /S(z) ratio to this value; uncertainties also in δ ¹³ C _r and δ ¹³ C _a endmember values.	Paragraph 7.3. Opportunities to use soil organic carbon and/or leaf wax δ ¹³ C to improve δ ¹³ C _r ; develop new soil CO ₂ & pH proxies based on fluid inclusions and boron in soil carbonates; need broader geographical distribution of modern measurements; need more estimates of δ ¹³ C _a from benthic foraminifera (314) to extend back through the Mesozoic and Paleozoic; develop clumped isotope temperatures of shallow paleosol carbonates.

		compositions of respired CO ₂ and S(z); most records placed in Category 2 because common S(z) proxies deemed semiquantitative.		
Nahcolite T, petrographic data	Paragraph 8.1. Explanation of trona-nahcolite-natron equilibria.	Paragraph 8.2. A presence/absence proxy.	Paragraph 8.1. No proxy equation; presence-absence only. Paragraph Return to Error! Reference source not found.Error! Reference source not found.Table S2. 8.3. Requires T to refine mineral phase equilibrium; uncertainties in air-water disequilibrium.	Paragraph Return to Error! Reference source not found.Error! Reference source not found.Table S2. 8.3. Opportunities to develop clumped isotope temperatures for precipitation of Na-carbonates; prospect for new sample locations.

1. Some or all listed variables may be required, depending on calculation approach; see sections 1-8 for details.
2. Specific to the Cenozoic.

Table S3. Values for $\epsilon_{\text{biomass/biomarker}}$.

<i>biomarker</i>	ϵ (‰)	$\pm 1\sigma$	<i>n</i>	<i>references</i>
C _{37:2} methyl ketone (MK37:2) ^(a)	4.80	0.75	21	Popp et al. (148), Riebesell et al. (438)
C _{37:3} methyl ketone (MK37:3) ^(a)	4.97	0.67	21	Popp et al. (148), Riebesell et al. (438)
MK37:3+ MK37:2 ^(a)	4.68	0.78	25	Popp et al. (148), Riebesell et al. (438), Wilkes et al. (439)
phytol ^(b)	3.60	1.44	23	Witkowski et al. (127) and references therein

(a) mean and standard deviation calculated from all measurements.

(b) ϵ values averaged for individual species and then the mean and std deviation calculated across species.

References and Notes

1. S. Arrhenius, XXXI. On the influence of carbonic acid in the air upon the temperature of the ground. *Lond. Edinb. Dublin Philos. Mag. J. Sci.* **41**, 237–276 (1896). [doi:10.1080/14786449608620846](https://doi.org/10.1080/14786449608620846)
2. IPCC, *Climate Change 2021: The Physical Science Basis. Contribution of Working Group I to the Sixth Assessment Report of the Intergovernmental Panel on Climate Change*, V. Masson-Delmotte *et al.*, Eds. (Cambridge Univ. Press, 2021).
3. P. Tans, R. Keeling, “Carbon cycle greenhouse gases: Trends in atmospheric carbon dioxide” (National Oceanic and Atmospheric Administration, Earth System Research Laboratories, Global Monitoring Laboratory, 2023); <http://www.esrl.noaa.gov/gmd/ccgg/trends/>.
4. K. E. Taylor, R. J. Stouffer, G. A. Meehl, An overview of CMIP5 and the experiment design. *Bull. Am. Meteorol. Soc.* **93**, 485–498 (2011). [doi:10.1175/BAMS-D-11-00094.1](https://doi.org/10.1175/BAMS-D-11-00094.1)
5. R. Caballero, M. Huber, State-dependent climate sensitivity in past warm climates and its implications for future climate projections. *Proc. Natl. Acad. Sci. U.S.A.* **110**, 14162–14167 (2013). [doi:10.1073/pnas.1303365110](https://doi.org/10.1073/pnas.1303365110) [Medline](#)
6. J. Zhu, C. J. Poulsen, On the increase of climate sensitivity and cloud feedback with warming in the community atmosphere models. *Geophys. Res. Lett.* **47**, e2020GL089143 (2020). [doi:10.1029/2020GL089143](https://doi.org/10.1029/2020GL089143)
7. J. Zhu, C. J. Poulsen, B. L. Otto-Bliesner, High climate sensitivity in CMIP6 model not supported by paleoclimate. *Nat. Clim. Chang.* **10**, 378–379 (2020). [doi:10.1038/s41558-020-0764-6](https://doi.org/10.1038/s41558-020-0764-6)
8. E. J. Judd, J. E. Tierney, B. T. Huber, S. L. Wing, D. J. Lunt, H. L. Ford, G. N. Inglis, E. L. McClymont, C. L. O’Brien, R. Rattanasriampaipong, W. Si, M. L. Staitis, K. Thirumalai, E. Anagnostou, M. J. Cramwinckel, R. R. Dawson, D. Evans, W. R. Gray, E. L. Grossman, M. J. Henahan, B. N. Hupp, K. G. MacLeod, L. K. O’Connor, M. L. Sánchez Montes, H. Song, Y. G. Zhang, The PhanSST global database of Phanerozoic sea surface temperature proxy data. *Sci. Data* **9**, 753 (2022). [doi:10.1038/s41597-022-01826-0](https://doi.org/10.1038/s41597-022-01826-0) [Medline](#)
9. R. J. Delmas, J.-M. Ascencio, M. Legrand, Polar ice evidence that atmospheric CO₂ 20,000 yr BP was 50% of present. *Nature* **284**, 155–157 (1980). [doi:10.1038/284155a0](https://doi.org/10.1038/284155a0)
10. A. Neftel, H. Oeschger, J. Schwander, B. Stauffer, R. Zimbrunn, Ice core sample measurements give atmospheric CO₂ content during the past 40,000 yr. *Nature* **295**, 220–223 (1982). [doi:10.1038/295220a0](https://doi.org/10.1038/295220a0)
11. B. Bereiter, S. Eggleston, J. Schmitt, C. Nehrbass-Ahles, T. F. Stocker, H. Fischer, S. Kipfstuhl, J. Chappellaz, Revision of the EPICA Dome C CO₂ record from 800 to 600 kyr before present. *Geophys. Res. Lett.* **42**, 542–549 (2015). [doi:10.1002/2014GL061957](https://doi.org/10.1002/2014GL061957)
12. Y. Yan, M. L. Bender, E. J. Brook, H. M. Clifford, P. C. Kemeny, A. V. Kurbatov, S. Mackay, P. A. Mayewski, J. Ng, J. P. Severinghaus, J. A. Higgins, Two-million-year-old snapshots of atmospheric gases from Antarctic ice. *Nature* **574**, 663–666 (2019). [doi:10.1038/s41586-019-1692-3](https://doi.org/10.1038/s41586-019-1692-3) [Medline](#)

13. J. A. Higgins, A. V. Kurbatov, N. E. Spaulding, E. Brook, D. S. Introne, L. M. Chimiak, Y. Yan, P. A. Mayewski, M. L. Bender, Atmospheric composition 1 million years ago from blue ice in the Allan Hills, Antarctica. *Proc. Natl. Acad. Sci. U.S.A.* **112**, 6887–6891 (2015). [doi:10.1073/pnas.1420232112](https://doi.org/10.1073/pnas.1420232112) [Medline](#)
14. C. Nehrbass-Ahles, J. Shin, J. Schmitt, B. Bereiter, F. Joos, A. Schilt, L. Schmidely, L. Silva, G. Teste, R. Grilli, J. Chappellaz, D. Hodell, H. Fischer, T. F. Stocker, Abrupt CO₂ release to the atmosphere under glacial and early interglacial climate conditions. *Science* **369**, 1000–1005 (2020). [doi:10.1126/science.aay8178](https://doi.org/10.1126/science.aay8178) [Medline](#)
15. C. Le Quéré, M. R. Raupach, J. G. Canadell, G. Marland, L. Bopp, P. Ciais, T. J. Conway, S. C. Doney, R. A. Feely, P. Foster, P. Friedlingstein, K. Gurney, R. A. Houghton, J. I. House, C. Huntingford, P. E. Levy, M. R. Lomas, J. Majkut, N. Metzl, J. P. Ometto, G. P. Peters, I. C. Prentice, J. T. Randerson, S. W. Running, J. L. Sarmiento, U. Schuster, S. Sitch, T. Takahashi, N. Viovy, G. R. van der Werf, F. I. Woodward, Trends in the sources and sinks of carbon dioxide. *Nat. Geosci.* **2**, 831–836 (2009). [doi:10.1038/ngeo689](https://doi.org/10.1038/ngeo689)
16. P. Friedlingstein, M. O’Sullivan, M. W. Jones, R. M. Andrew, L. Gregor, J. Hauck, C. Le Quéré, I. T. Lujckx, A. Olsen, G. P. Peters, W. Peters, J. Pongratz, C. Schwingshackl, S. Sitch, J. G. Canadell, P. Ciais, R. B. Jackson, S. R. Alin, R. Alkama, A. Arneeth, V. K. Arora, N. R. Bates, M. Becker, N. Bellouin, H. C. Bittig, L. Bopp, F. Chevallier, L. P. Chini, M. Cronin, W. Evans, S. Falk, R. A. Feely, T. Gasser, M. Gehlen, T. Gkritzalis, L. Gloege, G. Grassi, N. Gruber, Ö. Gürses, I. Harris, M. Hefner, R. A. Houghton, G. C. Hurtt, Y. Iida, T. Ilyina, A. K. Jain, A. Jersild, K. Kadono, E. Kato, D. Kennedy, K. Klein Goldewijk, J. Knauer, J. I. Korsbakken, P. Landschützer, N. Lefèvre, K. Lindsay, J. Liu, Z. Liu, G. Marland, N. Mayot, M. J. McGrath, N. Metzl, N. M. Monacci, D. R. Munro, S.-I. Nakaoka, Y. Niwa, K. O’Brien, T. Ono, P. I. Palmer, N. Pan, D. Pierrot, K. Pockock, B. Poulter, L. Resplandy, E. Robertson, C. Rödenbeck, C. Rodriguez, T. M. Rosan, J. Schwinger, R. Séférian, J. D. Shutler, I. Skjelvan, T. Steinhoff, Q. Sun, A. J. Sutton, C. Sweeney, S. Takao, T. Tanhua, P. P. Tans, X. Tian, H. Tian, B. Tilbrook, H. Tsujino, F. Tubiello, G. R. van der Werf, A. P. Walker, R. Wanninkhof, C. Whitehead, A. Willstrand Wranne, R. Wright, W. Yuan, C. Yue, X. Yue, S. Zaehle, J. Zeng, B. Zheng, Global carbon budget 2022. *Earth Syst. Sci. Data* **14**, 4811–4900 (2022). [doi:10.5194/essd-14-4811-2022](https://doi.org/10.5194/essd-14-4811-2022)
17. P. Valdes, Built for stability. *Nat. Geosci.* **4**, 414–416 (2011). [doi:10.1038/ngeo1200](https://doi.org/10.1038/ngeo1200)
18. W. Kiessling, M. Aberhan, L. Villier, Phanerozoic trends in skeletal mineralogy driven by mass extinctions. *Nat. Geosci.* **1**, 527–530 (2008). [doi:10.1038/ngeo251](https://doi.org/10.1038/ngeo251)
19. J. L. Payne, A. M. Bush, N. A. Heim, M. L. Knope, D. J. McCauley, Ecological selectivity of the emerging mass extinction in the oceans. *Science* **353**, 1284–1286 (2016). [doi:10.1126/science.aaf2416](https://doi.org/10.1126/science.aaf2416) [Medline](#)
20. E. J. Edwards, C. P. Osborne, C. A. E. Strömberg, S. A. Smith, W. J. Bond, P.-A. Christin, A. B. Cousins, M. R. Duvall, D. L. Fox, R. P. Freckleton, O. Ghannoum, J. Hartwell, Y. Huang, C. M. Janis, J. E. Keeley, E. A. Kellogg, A. K. Knapp, A. D. B. Leakey, D. M. Nelson, J. M. Saarela, R. F. Sage, O. E. Sala, N. Salamin, C. J. Still, B. Tipler; C4

- Grasses Consortium, The origins of C₄ grasslands: Integrating evolutionary and ecosystem science. *Science* **328**, 587–591 (2010). [doi:10.1126/science.1177216](https://doi.org/10.1126/science.1177216) [Medline](#)
21. F. A. McInerney, S. L. Wing, The Paleocene-Eocene Thermal Maximum: A perturbation of carbon cycle, climate, and biosphere with implications for the future. *Annu. Rev. Earth Planet. Sci.* **39**, 489–516 (2011). [doi:10.1146/annurev-earth-040610-133431](https://doi.org/10.1146/annurev-earth-040610-133431)
 22. W. Konrad, D. L. Royer, P. J. Franks, A. Roth-Nebelsick, Quantitative critique of leaf-based paleo-CO₂ proxies: Consequences for their reliability and applicability. *Geol. J.* **56**, 886–902 (2020). [doi:10.1002/gj.3807](https://doi.org/10.1002/gj.3807)
 23. J. C. McElwain, M. Steinthorsdottir, Paleoecology, ploidy, paleoatmospheric composition, and developmental biology: A review of the multiple uses of fossil stomata. *Plant Physiol.* **174**, 650–664 (2017). [doi:10.1104/pp.17.00204](https://doi.org/10.1104/pp.17.00204) [Medline](#)
 24. B. A. Schubert, A. H. Jahren, The effect of atmospheric CO₂ concentration on carbon isotope fractionation in C₃ land plants. *Geochim. Cosmochim. Acta* **96**, 29–43 (2012). [doi:10.1016/j.gca.2012.08.003](https://doi.org/10.1016/j.gca.2012.08.003)
 25. T. E. Cerling, Carbon dioxide in the atmosphere; evidence from Cenozoic and Mesozoic Paleosols. *Am. J. Sci.* **291**, 377–400 (1991). [doi:10.2475/ajs.291.4.377](https://doi.org/10.2475/ajs.291.4.377)
 26. D. O. Breecker, Quantifying and understanding the uncertainty of atmospheric CO₂ concentrations determined from calcic paleosols. *Geochem. Geophys. Geosyst.* **14**, 3210–3220 (2013). [doi:10.1002/ggge.20189](https://doi.org/10.1002/ggge.20189)
 27. E. A. Jagniecki, T. K. Lowenstein, D. M. Jenkins, R. V. Demicco, Eocene atmospheric CO₂ from the nahcolite proxy. *Geology* **43**, 1075–1078 (2015).
 28. T. K. Lowenstein, R. V. Demicco, Elevated Eocene atmospheric CO₂ and its subsequent decline. *Science* **313**, 1928 (2006). [doi:10.1126/science.1129555](https://doi.org/10.1126/science.1129555) [Medline](#)
 29. M. Pagani, “12.13 - Biomarker-based inferences of past climate: The alkenone pCO₂ proxy” in *Treatise on Geochemistry*, vol. 12, H. D. Holland, K. K. Turekian, Eds. (Elsevier, ed. 2, 2014), pp. 361–378.
 30. B. Hönisch, S. M. Eggins, L. L. Haynes, K. A. Allen, K. Holland, K. Lorbacher, *Boron Proxies in Paleooceanography and Paleoclimatology*, Analytical Methods in Earth and Environmental Science Series (John Wiley & Sons, Ltd., 2019).
 31. J. W. B. Rae, “Boron isotopes in foraminifera: Systematics, biomineralisation, and CO₂ reconstruction” in *Boron Isotopes: The Fifth Element*, H. Marschall, G. Foster, Eds. (Springer International Publishing, 2018), pp. 107–143.
 32. D. J. Beerling, D. L. Royer, Convergent Cenozoic CO₂ history. *Nat. Geosci.* **4**, 418–420 (2011). [doi:10.1038/ngeo1186](https://doi.org/10.1038/ngeo1186)
 33. G. L. Foster, D. L. Royer, D. J. Lunt, Future climate forcing potentially without precedent in the last 420 million years. *Nat. Commun.* **8**, 14845 (2017). [doi:10.1038/ncomms14845](https://doi.org/10.1038/ncomms14845) [Medline](#)
 34. J. W. B. Rae, Y. G. Zhang, X. Liu, G. L. Foster, H. M. Stoll, R. D. M. Whiteford, Atmospheric CO₂ over the past 66 million years from marine archives. *Annu. Rev. Earth Planet. Sci.* **49**, 609–641 (2021). [doi:10.1146/annurev-earth-082420-063026](https://doi.org/10.1146/annurev-earth-082420-063026)

35. S. Ji, J. Nie, A. Lechler, K. W. Huntington, E. O. Heitmann, D. O. Breecker, A symmetrical CO₂ peak and asymmetrical climate change during the middle Miocene. *Earth Planet. Sci. Lett.* **499**, 134–144 (2018). [doi:10.1016/j.epsl.2018.07.011](https://doi.org/10.1016/j.epsl.2018.07.011)
36. J. Da, Y. G. Zhang, G. Li, X. Meng, J. Ji, Low CO₂ levels of the entire Pleistocene epoch. *Nat. Commun.* **10**, 4342 (2019). [doi:10.1038/s41467-019-12357-5](https://doi.org/10.1038/s41467-019-12357-5) [Medline](#)
37. E. Hyland, N. D. Sheldon, M. Fan, Terrestrial paleoenvironmental reconstructions indicate transient peak warming during the early Eocene climatic optimum. *Geol. Soc. Am. Bull.* **125**, 1338–1348 (2013). [doi:10.1130/B30761.1](https://doi.org/10.1130/B30761.1)
38. J. Henderiks, M. Pagani, Refining ancient carbon dioxide estimates: Significance of coccolithophore cell size for alkenone-based pCO₂ records. *Paleoceanography* **22**, PA3202 (2007). [doi:10.1029/2006PA001399](https://doi.org/10.1029/2006PA001399)
39. S. R. Phelps, G. M. M. Hennon, S. T. Dyrman, M. D. Hernández Limón, O. M. Williamson, P. J. Polissar, Carbon isotope fractionation in Noelaerhabdaceae algae in culture and a critical evaluation of the alkenone paleobarometer. *Geochem. Geophys. Geosyst.* **22**, e2021GC009657 (2021). [doi:10.1029/2021GC009657](https://doi.org/10.1029/2021GC009657)
40. H. M. Stoll, J. Guitian, I. Hernandez-Almeida, L. M. Mejia, S. Phelps, P. Polissar, Y. Rosenthal, H. Zhang, P. Ziveri, Upregulation of phytoplankton carbon concentrating mechanisms during low CO₂ glacial periods and implications for the phytoplankton pCO₂ proxy. *Quat. Sci. Rev.* **208**, 1–20 (2019). [doi:10.1016/j.quascirev.2019.01.012](https://doi.org/10.1016/j.quascirev.2019.01.012)
41. Y. G. Zhang, J. Henderiks, X. Liu, Refining the alkenone-pCO₂ method II: Towards resolving the physiological parameter ‘b’. *Geochim. Cosmochim. Acta* **281**, 118–134 (2020). [doi:10.1016/j.gca.2020.05.002](https://doi.org/10.1016/j.gca.2020.05.002)
42. E. G. Hyland, N. D. Sheldon, Coupled CO₂-climate response during the Early Eocene Climatic Optimum. *Palaeogeogr. Palaeoclimatol. Palaeoecol.* **369**, 125–135 (2013). [doi:10.1016/j.palaeo.2012.10.011](https://doi.org/10.1016/j.palaeo.2012.10.011)
43. T. Westerhold, N. Marwan, A. J. Drury, D. Liebrand, C. Agnini, E. Anagnostou, J. S. K. Barnett, S. M. Bohaty, D. De Vleeschouwer, F. Florindo, T. Frederichs, D. A. Hodell, A. E. Holbourn, D. Kroon, V. Laurentano, K. Littler, L. J. Lourens, M. Lyle, H. Pälike, U. Röhl, J. Tian, R. H. Wilkens, P. A. Wilson, J. C. Zachos, An astronomically dated record of Earth’s climate and its predictability over the last 66 million years. *Science* **369**, 1383–1387 (2020). [doi:10.1126/science.aba6853](https://doi.org/10.1126/science.aba6853) [Medline](#)
44. J. Hansen, M. Sato, G. Russell, P. Kharecha, Climate sensitivity, sea level and atmospheric carbon dioxide. *Philos. Trans. A Math. Phys. Eng. Sci.* **371**, 20120294 (2013). [doi:10.1098/rsta.2012.0294](https://doi.org/10.1098/rsta.2012.0294) [Medline](#)
45. S. J. Ring, S. G. Mutz, T. A. Ehlers, Cenozoic proxy constraints on earth system sensitivity to greenhouse gases. *Paleoceanogr. Paleoclimatol.* **37**, e2021PA004364 (2022). [doi:10.1029/2021PA004364](https://doi.org/10.1029/2021PA004364)
46. T. D. Herbert, K. T. Lawrence, A. Tzanova, L. C. Peterson, R. Caballero-Gill, C. S. Kelly, Late Miocene global cooling and the rise of modern ecosystems. *Nat. Geosci.* **9**, 843–847 (2016). [doi:10.1038/ngeo2813](https://doi.org/10.1038/ngeo2813)

47. D. E. Gaskell, M. Huber, C. L. O'Brien, G. N. Inglis, R. P. Acosta, C. J. Poulsen, P. M. Hull, The latitudinal temperature gradient and its climate dependence as inferred from foraminiferal $\delta^{18}\text{O}$ over the past 95 million years. *Proc. Natl. Acad. Sci. U.S.A.* **119**, e2111332119 (2022). [doi:10.1073/pnas.2111332119](https://doi.org/10.1073/pnas.2111332119) [Medline](#)
48. C. L. O'Brien, M. Huber, E. Thomas, M. Pagani, J. R. Super, L. E. Elder, P. M. Hull, The enigma of Oligocene climate and global surface temperature evolution. *Proc. Natl. Acad. Sci. U.S.A.* **117**, 25302–25309 (2020). [doi:10.1073/pnas.2003914117](https://doi.org/10.1073/pnas.2003914117) [Medline](#)
49. D. J. Lunt, A. Farnsworth, C. Loptson, G. L. Foster, P. Markwick, C. L. O'Brien, R. D. Pancost, S. A. Robinson, N. Wrobel, Palaeogeographic controls on climate and proxy interpretation. *Clim. Past* **12**, 1181–1198 (2016). [doi:10.5194/cp-12-1181-2016](https://doi.org/10.5194/cp-12-1181-2016)
50. A. N. Meckler, P. F. Sexton, A. M. Piasecki, T. J. Leutert, J. Marquardt, M. Ziegler, T. Agterhuis, L. J. Lourens, J. W. B. Rae, J. Barnet, A. Tripathi, S. M. Bernasconi, Cenozoic evolution of deep ocean temperature from clumped isotope thermometry. *Science* **377**, 86–90 (2022). [doi:10.1126/science.abk0604](https://doi.org/10.1126/science.abk0604) [Medline](#)
51. PALAEOSENS Project Members, Making sense of palaeoclimate sensitivity. *Nature* **491**, 683–691 (2012). [doi:10.1038/nature11574](https://doi.org/10.1038/nature11574) [Medline](#)
52. A. Tripathi, D. Darby, Evidence for ephemeral middle Eocene to early Oligocene Greenland glacial ice and pan-Arctic sea ice. *Nat. Commun.* **9**, 1038 (2018). [doi:10.1038/s41467-018-03180-5](https://doi.org/10.1038/s41467-018-03180-5) [Medline](#)
53. H. D. Scher, S. M. Bohaty, B. W. Smith, G. H. Munn, Isotopic interrogation of a suspected late Eocene glaciation. *Paleoceanography* **29**, 628–644 (2014). [doi:10.1002/2014PA002648](https://doi.org/10.1002/2014PA002648)
54. I. Sauermilch, J. M. Whittaker, A. Klockner, D. R. Munday, K. Hochmuth, P. K. Bijl, J. H. LaCasce, Gateway-driven weakening of ocean gyres leads to Southern Ocean cooling. *Nat. Commun.* **12**, 6465 (2021). [doi:10.1038/s41467-021-26658-1](https://doi.org/10.1038/s41467-021-26658-1) [Medline](#)
55. D. L. Royer, Climate sensitivity in the geologic past. *Annu. Rev. Earth Planet. Sci.* **44**, 277–293 (2016). [doi:10.1146/annurev-earth-100815-024150](https://doi.org/10.1146/annurev-earth-100815-024150)
56. R. M. Brown, T. B. Chalk, A. J. Crocker, P. A. Wilson, G. L. Foster, Late Miocene cooling coupled to carbon dioxide with Pleistocene-like climate sensitivity. *Nat. Geosci.* **15**, 664–670 (2022). [doi:10.1038/s41561-022-00982-7](https://doi.org/10.1038/s41561-022-00982-7)
57. T. E. Wong, Y. Cui, D. L. Royer, K. Keller, A tighter constraint on Earth-system sensitivity from long-term temperature and carbon-cycle observations. *Nat. Commun.* **12**, 3173 (2021). [doi:10.1038/s41467-021-23543-9](https://doi.org/10.1038/s41467-021-23543-9) [Medline](#)
58. D. L. Royer, M. Pagani, D. J. Beerling, Geobiological constraints on Earth system sensitivity to CO_2 during the Cretaceous and Cenozoic. *Geobiology* **10**, 298–310 (2012). [doi:10.1111/j.1472-4669.2012.00320.x](https://doi.org/10.1111/j.1472-4669.2012.00320.x) [Medline](#)
59. J. E. Tierney, J. Zhu, M. Li, A. Ridgwell, G. J. Hakim, C. J. Poulsen, R. D. M. Whiteford, J. W. B. Rae, L. R. Kump, Spatial patterns of climate change across the Paleocene-Eocene Thermal Maximum. *Proc. Natl. Acad. Sci. U.S.A.* **119**, e2205326119 (2022). [doi:10.1073/pnas.2205326119](https://doi.org/10.1073/pnas.2205326119) [Medline](#)

60. E. Anagnostou, E. H. John, T. L. Babila, P. F. Sexton, A. Ridgwell, D. J. Lunt, P. N. Pearson, T. B. Chalk, R. D. Pancost, G. L. Foster, Proxy evidence for state-dependence of climate sensitivity in the Eocene greenhouse. *Nat. Commun.* **11**, 4436 (2020). [doi:10.1038/s41467-020-17887-x](https://doi.org/10.1038/s41467-020-17887-x) [Medline](#)
61. J. Hansen, M. Sato, P. Kharecha, D. Beerling, R. Berner, V. Masson-Delmotte, M. Pagani, M. Raymo, D. L. Royer, J. C. Zachos, Target atmospheric CO₂: Where should humanity aim? *Open Atmos. Sci. J.* **2**, 217–231 (2008). [doi:10.2174/1874282300802010217](https://doi.org/10.2174/1874282300802010217)
62. J. T. Kiehl, C. A. Shields, Sensitivity of the Palaeocene-Eocene Thermal Maximum climate to cloud properties. *Philos. Trans. A Math. Phys. Eng. Sci.* **371**, 20130093 (2013). [doi:10.1098/rsta.2013.0093](https://doi.org/10.1098/rsta.2013.0093) [Medline](#)
63. J. Zhu, C. J. Poulsen, J. E. Tierney, Simulation of Eocene extreme warmth and high climate sensitivity through cloud feedbacks. *Sci. Adv.* **5**, eaax1874 (2019). [doi:10.1126/sciadv.aax1874](https://doi.org/10.1126/sciadv.aax1874) [Medline](#)
64. D. J. Beerling, A. Fox, D. S. Stevenson, P. J. Valdes, Enhanced chemistry-climate feedbacks in past greenhouse worlds. *Proc. Natl. Acad. Sci. U.S.A.* **108**, 9770–9775 (2011). [doi:10.1073/pnas.1102409108](https://doi.org/10.1073/pnas.1102409108) [Medline](#)
65. T. Schneider, C. M. Kaul, K. G. Pressel, Possible climate transitions from breakup of stratocumulus decks under greenhouse warming. *Nat. Geosci.* **12**, 163–167 (2019). [doi:10.1038/s41561-019-0310-1](https://doi.org/10.1038/s41561-019-0310-1)
66. K. G. Miller, J. V. Browning, W. J. Schmelz, R. E. Kopp, G. S. Mountain, J. D. Wright, Cenozoic sea-level and cryospheric evolution from deep-sea geochemical and continental margin records. *Sci. Adv.* **6**, eaaz1346 (2020). [doi:10.1126/sciadv.aaz1346](https://doi.org/10.1126/sciadv.aaz1346) [Medline](#)
67. E. J. Rohling, J. Yu, D. Heslop, G. L. Foster, B. Opdyke, A. P. Roberts, Sea level and deep-sea temperature reconstructions suggest quasi-stable states and critical transitions over the past 40 million years. *Sci. Adv.* **7**, eabf5326 (2021). [doi:10.1126/sciadv.abf5326](https://doi.org/10.1126/sciadv.abf5326) [Medline](#)
68. M. J. Henahan, K. M. Edgar, G. L. Foster, D. E. Penman, P. M. Hull, R. Greenop, E. Anagnostou, P. N. Pearson, Revisiting the Middle Eocene Climatic Optimum “carbon cycle conundrum” with new estimates of atmospheric pCO₂ from boron isotopes. *Paleoceanogr. Paleoclimatol.* **35**, e2019PA003713 (2020). [doi:10.1029/2019PA003713](https://doi.org/10.1029/2019PA003713)
69. E. Gasson, D. J. Lunt, R. DeConto, A. Goldner, M. Heinemann, M. Huber, A. N. LeGrande, D. Pollard, N. Sahoo, M. Siddall, A. Winguth, P. J. Valdes, Uncertainties in the modelled CO₂ threshold for Antarctic glaciation. *Clim. Past* **10**, 451–466 (2014). [doi:10.5194/cp-10-451-2014](https://doi.org/10.5194/cp-10-451-2014)
70. R. M. DeConto, D. Pollard, P. A. Wilson, H. Pälike, C. H. Lear, M. Pagani, Thresholds for Cenozoic bipolar glaciation. *Nature* **455**, 652–656 (2008). [doi:10.1038/nature07337](https://doi.org/10.1038/nature07337) [Medline](#)
71. R. M. DeConto, D. Pollard, Rapid Cenozoic glaciation of Antarctica induced by declining atmospheric CO₂. *Nature* **421**, 245–249 (2003). [doi:10.1038/nature01290](https://doi.org/10.1038/nature01290) [Medline](#)

72. E. Gasson, R. M. DeConto, D. Pollard, R. H. Levy, Dynamic Antarctic ice sheet during the early to mid-Miocene. *Proc. Natl. Acad. Sci. U.S.A.* **113**, 3459–3464 (2016). [doi:10.1073/pnas.1516130113](https://doi.org/10.1073/pnas.1516130113) [Medline](#)
73. D. Pollard, R. M. DeConto, Hysteresis in Cenozoic Antarctic ice-sheet variations. *Global Planet. Change* **45**, 9–21 (2005). [doi:10.1016/j.gloplacha.2004.09.011](https://doi.org/10.1016/j.gloplacha.2004.09.011)
74. G. J. G. Paxman, E. G. W. Gasson, S. S. R. Jamieson, M. J. Bentley, F. Ferraccioli, Long-term increase in Antarctic Ice Sheet vulnerability driven by bed topography evolution. *Geophys. Res. Lett.* **47**, e2020GL090003 (2020). [doi:10.1029/2020GL090003](https://doi.org/10.1029/2020GL090003)
75. J. J. Fürst, G. Durand, F. Gillet-Chaulet, L. Tavard, M. Rankl, M. Braun, O. Gagliardini, The safety band of Antarctic ice shelves. *Nat. Clim. Chang.* **6**, 479–482 (2016). [doi:10.1038/nclimate2912](https://doi.org/10.1038/nclimate2912)
76. J. C. McElwain, Paleobotany and global change: Important lessons for species to biomes from vegetation responses to past global change. *Annu. Rev. Plant Biol.* **69**, 761–787 (2018). [doi:10.1146/annurev-arplant-042817-040405](https://doi.org/10.1146/annurev-arplant-042817-040405) [Medline](#)
77. S.-M. Popescu, J.-P. Suc, S. Fauquette, M. Bessedik, G. Jiménez-Moreno, C. Robin, L. Labrousse, Mangrove distribution and diversity during three Cenozoic thermal maxima in the Northern Hemisphere (pollen records from the Arctic–North Atlantic–Mediterranean regions). *J. Biogeogr.* **48**, 2771–2784 (2021). [doi:10.1111/jbi.14238](https://doi.org/10.1111/jbi.14238)
78. C. Jaramillo, M. J. Rueda, G. Mora, Cenozoic plant diversity in the neotropics. *Science* **311**, 1893–1896 (2006). [doi:10.1126/science.1121380](https://doi.org/10.1126/science.1121380) [Medline](#)
79. J. Y. Lim, H. Huang, A. Farnsworth, D. J. Lunt, W. J. Baker, R. J. Morley, W. D. Kissling, C. Hoorn, The Cenozoic history of palms: Global diversification, biogeography and the decline of megathermal forests. *Glob. Ecol. Biogeogr.* **31**, 425–439 (2022). [doi:10.1111/geb.13436](https://doi.org/10.1111/geb.13436)
80. A. Graham, The age and diversification of terrestrial New World ecosystems through Cretaceous and Cenozoic time. *Am. J. Bot.* **98**, 336–351 (2011). [doi:10.3732/ajb.1000353](https://doi.org/10.3732/ajb.1000353) [Medline](#)
81. J. R. Ehleringer, R. K. Monson, Evolutionary and ecological aspects of photosynthetic pathway variation. *Annu. Rev. Ecol. Syst.* **24**, 411–439 (1993). [doi:10.1146/annurev.es.24.110193.002211](https://doi.org/10.1146/annurev.es.24.110193.002211)
82. H. Griffiths, “Carbon dioxide concentrating mechanisms and the evolution of CAM in vascular epiphytes” in *Vascular Plants as Epiphytes: Evolution and Ecophysiology*, U. Lüttge, Ed. (Springer, 1989), pp. 42–86.
83. C. J. Still, J. A. Berry, G. J. Collatz, R. S. DeFries, Global distribution of C₃ and C₄ vegetation: Carbon cycle implications. *Global Biogeochem. Cycles* **17**, 1006 (2003). [doi:10.1029/2001GB001807](https://doi.org/10.1029/2001GB001807)
84. P.-A. Christin, G. Besnard, E. Samaritani, M. R. Duvall, T. R. Hodkinson, V. Savolainen, N. Salamin, Oligocene CO₂ decline promoted C₄ photosynthesis in grasses. *Curr. Biol.* **18**, 37–43 (2008). [doi:10.1016/j.cub.2007.11.058](https://doi.org/10.1016/j.cub.2007.11.058) [Medline](#)

85. A. Vicentini, J. C. Barber, S. S. Aliscioni, L. M. Giussani, E. A. Kellogg, The age of the grasses and clusters of origins of C₄ photosynthesis. *Glob. Change Biol.* **14**, 2963–2977 (2008). [doi:10.1111/j.1365-2486.2008.01688.x](https://doi.org/10.1111/j.1365-2486.2008.01688.x)
86. P. J. Polissar, C. Rose, K. T. Uno, S. R. Phelps, P. deMenocal, Synchronous rise of African C₄ ecosystems 10 million years ago in the absence of aridification. *Nat. Geosci.* **12**, 657–660 (2019). [doi:10.1038/s41561-019-0399-2](https://doi.org/10.1038/s41561-019-0399-2)
87. L. Tauxe, S. J. Feakins, A reassessment of the chronostratigraphy of late Miocene C₃–C₄ transitions. *Paleoceanogr. Paleoclimatol.* **35**, e2020PA003857 (2020). [doi:10.1029/2020PA003857](https://doi.org/10.1029/2020PA003857)
88. T. E. Cerling, J. M. Harris, B. J. MacFadden, M. G. Leakey, J. Quade, V. Eisenmann, J. R. Ehleringer, Global vegetation change through the Miocene/Pliocene boundary. *Nature* **389**, 153–158 (1997). [doi:10.1038/38229](https://doi.org/10.1038/38229)
89. M. Arakaki, P.-A. Christin, R. Nyffeler, A. Lendel, U. Eggli, R. M. Ogburn, E. Spriggs, M. J. Moore, E. J. Edwards, Contemporaneous and recent radiations of the world’s major succulent plant lineages. *Proc. Natl. Acad. Sci. U.S.A.* **108**, 8379–8384 (2011). [doi:10.1073/pnas.1100628108](https://doi.org/10.1073/pnas.1100628108) [Medline](#)
90. T. J. Givnish, D. Spalink, M. Ames, S. P. Lyon, S. J. Hunter, A. Zuluaga, W. J. D. Iles, M. A. Clements, M. T. K. Arroyo, J. Leebens-Mack, L. Endara, R. Kriebel, K. M. Neubig, W. M. Whitten, N. H. Williams, K. M. Cameron, Orchid phylogenomics and multiple drivers of their extraordinary diversification. *Proc. Biol. Sci.* **282**, 20151553 (2015). [doi:10.1098/rspb.2015.1553](https://doi.org/10.1098/rspb.2015.1553) [Medline](#)
91. E. J. Edwards, Evolutionary trajectories, accessibility and other metaphors: The case of C₄ and CAM photosynthesis. *New Phytol.* **223**, 1742–1755 (2019). [doi:10.1111/nph.15851](https://doi.org/10.1111/nph.15851) [Medline](#)
92. J. R. Ehleringer, T. E. Cerling, B. R. Helliker, C₄ photosynthesis, atmospheric CO₂, and climate. *Oecologia* **112**, 285–299 (1997). [doi:10.1007/s004420050311](https://doi.org/10.1007/s004420050311) [Medline](#)
93. H. Zhou, B. R. Helliker, M. Huber, A. Dicks, E. Akçay, C₄ photosynthesis and climate through the lens of optimality. *Proc. Natl. Acad. Sci. U.S.A.* **115**, 12057–12062 (2018). [doi:10.1073/pnas.1718988115](https://doi.org/10.1073/pnas.1718988115) [Medline](#)
94. C. E. R. Lehmann, S. A. Archibald, W. A. Hoffmann, W. J. Bond, Deciphering the distribution of the savanna biome. *New Phytol.* **191**, 197–209 (2011). [doi:10.1111/j.1469-8137.2011.03689.x](https://doi.org/10.1111/j.1469-8137.2011.03689.x) [Medline](#)
95. W. M. Kürschner, Z. Kvacek, D. L. Dilcher, The impact of Miocene atmospheric carbon dioxide fluctuations on climate and the evolution of terrestrial ecosystems. *Proc. Natl. Acad. Sci. U.S.A.* **105**, 449–453 (2008). [doi:10.1073/pnas.0708588105](https://doi.org/10.1073/pnas.0708588105) [Medline](#)
96. C. A. E. Strömberg, Evolution of grasses and grassland ecosystems. *Annu. Rev. Earth Planet. Sci.* **39**, 517–544 (2011). [doi:10.1146/annurev-earth-040809-152402](https://doi.org/10.1146/annurev-earth-040809-152402)
97. A. T. Karp, K. T. Uno, P. J. Polissar, K. H. Freeman, Late Miocene C₄ grassland fire feedbacks on the Indian subcontinent. *Paleoceanogr. Paleoclimatol.* **36**, e2020PA004106 (2021). [doi:10.1029/2020PA004106](https://doi.org/10.1029/2020PA004106)

98. T. Kukla, J. K. C. Rugenstein, D. E. Ibarra, M. J. Winnick, C. A. E. Strömberg, C. P. Chamberlain, Drier winters drove Cenozoic open habitat expansion in North America. *AGU Adv.* **3**, e2021AV000566 (2022). [doi:10.1029/2021AV000566](https://doi.org/10.1029/2021AV000566)
99. M. Fortelius, J. T. Eronen, F. Kaya, H. Tang, P. Raia, K. Puolamäki, Evolution of Neogene mammals in Eurasia: Environmental forcing and biotic interactions. *Annu. Rev. Earth Planet. Sci.* **42**, 579–604 (2014). [doi:10.1146/annurev-earth-050212-124030](https://doi.org/10.1146/annurev-earth-050212-124030)
100. F. Kaya, F. Bibi, I. Žliobaitė, J. T. Eronen, T. Hui, M. Fortelius, The rise and fall of the Old World savannah fauna and the origins of the African savannah biome. *Nat. Ecol. Evol.* **2**, 241–246 (2018). [doi:10.1038/s41559-017-0414-1](https://doi.org/10.1038/s41559-017-0414-1) [Medline](#)
101. C. M. Janis, J. Damuth, J. M. Theodor, Miocene ungulates and terrestrial primary productivity: Where have all the browsers gone? *Proc. Natl. Acad. Sci. U.S.A.* **97**, 7899–7904 (2000). [doi:10.1073/pnas.97.14.7899](https://doi.org/10.1073/pnas.97.14.7899) [Medline](#)
102. M. Fortelius, N. Solounias, Functional characterization of ungulate molars using the abrasion–attrition wear gradient: A new method for reconstructing paleodiets. *Am. Mus. Novit.* **3301**, 1–36 (2000). [doi:10.1206/0003-0082\(2000\)301<0001:FCOUMU>2.0.CO;2](https://doi.org/10.1206/0003-0082(2000)301<0001:FCOUMU>2.0.CO;2)
103. M. C. Muhlbachler, F. Rivals, N. Solounias, G. M. Semperebon, Dietary change and evolution of horses in North America. *Science* **331**, 1178–1181 (2011). [doi:10.1126/science.1196166](https://doi.org/10.1126/science.1196166) [Medline](#)
104. C. A. E. Strömberg, Evolution of hypsodonty in equids: Testing a hypothesis of adaptation. *Paleobiology* **32**, 236–258 (2006). [doi:10.1666/0094-8373\(2006\)32\[236:EOHIET\]2.0.CO;2](https://doi.org/10.1666/0094-8373(2006)32[236:EOHIET]2.0.CO;2)
105. C. M. Janis, M. Fortelius, On the means whereby mammals achieve increased functional durability of their dentitions, with special reference to limiting factors. *Biol. Rev. Camb. Philos. Soc.* **63**, 197–230 (1988). [doi:10.1111/j.1469-185X.1988.tb00630.x](https://doi.org/10.1111/j.1469-185X.1988.tb00630.x) [Medline](#)
106. M. R. Badger, D. Hanson, G. D. Price, Evolution and diversity of CO₂ concentrating mechanisms in cyanobacteria. *Funct. Plant Biol.* **29**, 161–173 (2002). [doi:10.1071/PP01213](https://doi.org/10.1071/PP01213) [Medline](#)
107. M. P. S. Badger, Alkenone isotopes show evidence of active carbon concentrating mechanisms in coccolithophores as aqueous carbon dioxide concentrations fall below 7 μmol L⁻¹. *Biogeosciences* **18**, 1149–1160 (2021). [doi:10.5194/bg-18-1149-2021](https://doi.org/10.5194/bg-18-1149-2021)
108. Y. G. Zhang, M. Pagani, Z. Liu, S. M. Bohaty, R. Deconto, A 40-million-year history of atmospheric CO₂. *Philos. Trans. A Math. Phys. Eng. Sci.* **371**, 20130096 (2013). [doi:10.1098/rsta.2013.0096](https://doi.org/10.1098/rsta.2013.0096) [Medline](#)
109. P. D. Tortell, Evolutionary and ecological perspectives on carbon acquisition in phytoplankton. *Limnol. Oceanogr.* **45**, 744–750 (2000). [doi:10.4319/lo.2000.45.3.0744](https://doi.org/10.4319/lo.2000.45.3.0744)
110. C. T. Bolton, H. M. Stoll, Late Miocene threshold response of marine algae to carbon dioxide limitation. *Nature* **500**, 558–562 (2013). [doi:10.1038/nature12448](https://doi.org/10.1038/nature12448) [Medline](#)
111. M. N. Evans, S. E. Tolwinski-Ward, D. M. Thompson, K. J. Anchukaitis, Applications of proxy system modeling in high resolution paleoclimatology. *Quat. Sci. Rev.* **76**, 16–28 (2013). [doi:10.1016/j.quascirev.2013.05.024](https://doi.org/10.1016/j.quascirev.2013.05.024)

112. G. J. Bowen, B. Fischer-Femal, G. J. Reichart, A. Sluijs, C. H. Lear, Joint inversion of proxy system models to reconstruct paleoenvironmental time series from heterogeneous data. *Clim. Past* **16**, 65–78 (2020). [doi:10.5194/cp-16-65-2020](https://doi.org/10.5194/cp-16-65-2020)
113. M. B. Osman, J. E. Tierney, J. Zhu, R. Tardif, G. J. Hakim, J. King, C. J. Poulsen, Globally resolved surface temperatures since the Last Glacial Maximum. *Nature* **599**, 239–244 (2021). [doi:10.1038/s41586-021-03984-4](https://doi.org/10.1038/s41586-021-03984-4) [Medline](#)
114. C. Godbillot, F. Minoletti, F. Bassinot, M. Hermoso, Parallel between the isotopic composition of coccolith calcite and carbon levels across Termination II: developing a new paleo-CO₂ probe. *Clim. Past* **18**, 449–464 (2022). [doi:10.5194/cp-18-449-2022](https://doi.org/10.5194/cp-18-449-2022)
115. A. Pack, A. Gehler, A. Süssenberger, Exploring the usability of isotopically anomalous oxygen in bones and teeth as paleo-CO₂-barometer. *Geochim. Cosmochim. Acta* **102**, 306–317 (2013). [doi:10.1016/j.gca.2012.10.017](https://doi.org/10.1016/j.gca.2012.10.017)
116. C. R. Scotese, An atlas of Phanerozoic paleogeographic maps: the seas come in and the seas go out. *Annu. Rev. Earth Planet. Sci.* **49**, 679–728 (2021). [doi:10.1146/annurev-earth-081320-064052](https://doi.org/10.1146/annurev-earth-081320-064052)
117. P. A. Christin, C. P. Osborne, R. F. Sage, M. Arakaki, E. J. Edwards, C₄ eudicots are not younger than C₄ monocots. *J. Exp. Bot.* **62**, 3171–3181 (2011). [doi:10.1093/jxb/err041](https://doi.org/10.1093/jxb/err041) [Medline](#)
118. J. P. Jasper, J. M. Hayes, A carbon isotope record of CO₂ levels during the late Quaternary. *Nature* **347**, 462–464 (1990). [doi:10.1038/347462a0](https://doi.org/10.1038/347462a0) [Medline](#)
119. K. H. Freeman, J. M. Hayes, Fractionation of carbon isotopes by phytoplankton and estimates of ancient CO₂ levels. *Global Biogeochem. Cycles* **6**, 185–198 (1992). [doi:10.1029/92GB00190](https://doi.org/10.1029/92GB00190) [Medline](#)
120. B. N. Popp, R. Takigiku, J. M. Hayes, J. W. Louda, E. W. Baker, The post-Paleozoic chronology and mechanism of ¹³C depletion in primary marine organic matter. *Am. J. Sci.* **289**, 436–454 (1989). [doi:10.2475/ajs.289.4.436](https://doi.org/10.2475/ajs.289.4.436) [Medline](#)
121. E. A. Laws, B. N. Popp, R. R. Bidigare, M. C. Kennicutt, S. A. Macko, Dependence of phytoplankton carbon isotopic composition on growth rate and [CO₂]_{aq}: Theoretical considerations and experimental results. *Geochim. Cosmochim. Acta* **59**, 1131–1138 (1995). [doi:10.1016/0016-7037\(95\)00030-4](https://doi.org/10.1016/0016-7037(95)00030-4)
122. R. François, M. A. Altabet, R. Goericke, D. C. McCorkle, C. Brunet, A. Poisson, Changes in the δ¹³C of surface water particulate organic matter across the subtropical convergence in the SW Indian Ocean. *Global Biogeochem. Cycles* **7**, 627–644 (1993). [doi:10.1029/93GB01277](https://doi.org/10.1029/93GB01277)
123. M. Pagani, K. H. Freeman, N. Ohkouchi, K. Caldeira, Comparison of water column [CO_{2aq}] with sedimentary alkenone-based estimates: A test of the alkenone-CO₂ proxy. *Paleoceanography* **17**, 1069 (2002). [doi:10.1029/2002PA000756](https://doi.org/10.1029/2002PA000756)
124. G. H. Rau, T. Takahashi, D. J. Des Marais, D. J. Repeta, J. H. Martin, The relationship between δ¹³C of organic matter and [CO₂(aq)] in ocean surface water: Data from a JGOFS site in the northeast Atlantic Ocean and a model. *Geochim. Cosmochim. Acta* **56**, 1413–1419 (1992). [doi:10.1016/0016-7037\(92\)90073-R](https://doi.org/10.1016/0016-7037(92)90073-R) [Medline](#)

125. G. H. Rau, T. Takahashi, D. J. Des Marais, Latitudinal variations in plankton $\delta^{13}\text{C}$: Implications for CO_2 and productivity in past oceans. *Nature* **341**, 516–518 (1989). [doi:10.1038/341516a0](https://doi.org/10.1038/341516a0) [Medline](#)
126. M. Pagani, J. C. Zachos, K. H. Freeman, B. Tipple, S. Bohaty, Marked decline in atmospheric carbon dioxide concentrations during the Paleogene. *Science* **309**, 600–603 (2005). [doi:10.1126/science.1110063](https://doi.org/10.1126/science.1110063) [Medline](#)
127. C. R. Witkowski, J. W. H. Weijers, B. Blais, S. Schouten, J. S. Sinninghe Damsté, Molecular fossils from phytoplankton reveal secular P_{CO_2} trend over the Phanerozoic. *Sci. Adv.* **4**, eaat4556 (2018). [doi:10.1126/sciadv.aat4556](https://doi.org/10.1126/sciadv.aat4556) [Medline](#)
128. R. Goericke, J. P. Montoya, B. Fry, “Physiology of isotopic fractionation in algae and cyanobacteria” in *Stable Isotopes in Ecology and Environmental Science*, K. Lajtha, R. H. Michener, Eds. (Blackwell Scientific Publications, 1994), pp.187–221.
129. G. G. B. Tcherkez, G. D. Farquhar, T. J. Andrews, Despite slow catalysis and confused substrate specificity, all ribulose biphosphate carboxylases may be nearly perfectly optimized. *Proc. Natl. Acad. Sci. U.S.A.* **103**, 7246–7251 (2006). [doi:10.1073/pnas.0600605103](https://doi.org/10.1073/pnas.0600605103) [Medline](#)
130. P. G. Falkowski, J. A. Raven, *Aquatic Photosynthesis* (Princeton Univ. Press, ed. 2, 2007).
131. A. J. Boller, P. J. Thomas, C. M. Cavanaugh, K. M. Scott, Low stable carbon isotope fractionation by coccolithophore RubisCO. *Geochim. Cosmochim. Acta* **75**, 7200–7207 (2011). [doi:10.1016/j.gca.2011.08.031](https://doi.org/10.1016/j.gca.2011.08.031)
132. A. J. Boller, P. J. Thomas, C. M. Cavanaugh, K. M. Scott, Isotopic discrimination and kinetic parameters of RubisCO from the marine bloom-forming diatom, *Skeletonema costatum*. *Geobiology* **13**, 33–43 (2015). [doi:10.1111/gbi.12112](https://doi.org/10.1111/gbi.12112) [Medline](#)
133. S. Burkhardt, U. Riebesell, I. Zondervan, Effects of growth rate, CO_2 concentration, and cell size on the stable carbon isotope fractionation in marine phytoplankton. *Geochim. Cosmochim. Acta* **63**, 3729–3741 (1999). [doi:10.1016/S0016-7037\(99\)00217-3](https://doi.org/10.1016/S0016-7037(99)00217-3)
134. U. Riebesell, S. Burkhardt, A. Dauelsberg, B. Kroon, Carbon isotope fractionation by a marine diatom: dependence on the growth-rate-limiting resource. *Mar. Ecol. Prog. Ser.* **193**, 295–303 (2000). [doi:10.3354/meps193295](https://doi.org/10.3354/meps193295)
135. B. Rost, I. Zondervan, U. Riebesell, Light-dependent carbon isotope fractionation in the coccolithophorid *Emiliana huxleyi*. *Limnol. Oceanogr.* **47**, 120–128 (2002). [doi:10.4319/lo.2002.47.1.0120](https://doi.org/10.4319/lo.2002.47.1.0120)
136. P. A. Thompson, S. E. Calvert, Carbon isotope fractionation by *Emiliana huxleyi*. *Limnol. Oceanogr.* **40**, 673–679 (1995). [doi:10.4319/lo.1995.40.4.0673](https://doi.org/10.4319/lo.1995.40.4.0673)
137. S. C. Brassell, G. Eglinton, I. T. Marlowe, U. Pflaumann, M. Sarnthein, Molecular stratigraphy: A new tool for climatic assessment. *Nature* **320**, 129–133 (1986). [doi:10.1038/320129a0](https://doi.org/10.1038/320129a0)
138. L. M. Mejía, A. Méndez-Vicente, L. Abrevaya, K. T. Lawrence, C. Ladlow, C. Bolton, I. Cacho, H. Stoll, A diatom record of CO_2 decline since the late Miocene. *Earth Planet. Sci. Lett.* **479**, 18–33 (2017). [doi:10.1016/j.epsl.2017.08.034](https://doi.org/10.1016/j.epsl.2017.08.034)

139. R. R. Bidigare, A. Fluegge, K. H. Freeman, K. L. Hanson, J. M. Hayes, D. Hollander, J. P. Jasper, L. L. King, E. A. Laws, J. Milder, F. J. Millero, R. Pancost, B. N. Popp, P. A. Steinberg, S. G. Wakeham, Consistent fractionation of ^{13}C in nature and in the laboratory: Growth-rate effects in some haptophyte algae. *Global Biogeochem. Cycles* **11**, 279–292 (1997). [doi:10.1029/96GB03939](https://doi.org/10.1029/96GB03939) [Medline](#)
140. M. Pagani, M. Huber, Z. Liu, S. M. Bohaty, J. Henderiks, W. Sijp, S. Krishnan, R. M. DeConto, The role of carbon dioxide during the onset of Antarctic glaciation. *Science* **334**, 1261–1264 (2011). [doi:10.1126/science.1203909](https://doi.org/10.1126/science.1203909) [Medline](#)
141. M. Pagani, M. A. Arthur, K. H. Freeman, Miocene evolution of atmospheric carbon dioxide. *Paleoceanography* **14**, 273–292 (1999). [doi:10.1029/1999PA900006](https://doi.org/10.1029/1999PA900006)
142. B. D. A. Naafs, J. M. Castro, G. A. De Gea, M. L. Quijano, D. N. Schmidt, R. D. Pancost, Gradual and sustained carbon dioxide release during Aptian Oceanic Anoxic Event 1a. *Nat. Geosci.* **9**, 135–139 (2016). [doi:10.1038/ngeo2627](https://doi.org/10.1038/ngeo2627)
143. R. F. Weiss, Carbon dioxide in water and seawater: The solubility of a non-ideal gas. *Mar. Chem.* **2**, 203–215 (1974). [doi:10.1016/0304-4203\(74\)90015-2](https://doi.org/10.1016/0304-4203(74)90015-2)
144. I. Hernández-Almeida, K. M. Krumhardt, H. Zhang, H. M. Stoll, Estimation of physiological factors controlling carbon isotope fractionation in coccolithophores in photic zone and core-top samples. *Geochem. Geophys. Geosyst.* **21**, e2020GC009272 (2020). [doi:10.1029/2020GC009272](https://doi.org/10.1029/2020GC009272)
145. G. H. Rau, U. Riebesell, D. Wolf-Gladrow, A model of photosynthetic ^{13}C fractionation by marine phytoplankton based on diffusive molecular CO_2 uptake. *Mar. Ecol. Prog. Ser.* **133**, 275–285 (1996). [doi:10.3354/meps133275](https://doi.org/10.3354/meps133275)
146. H. L. O. McClelland, J. Bruggeman, M. Hermoso, R. E. M. Rickaby, The origin of carbon isotope vital effects in coccolith calcite. *Nat. Commun.* **8**, 14511 (2017). [doi:10.1038/ncomms14511](https://doi.org/10.1038/ncomms14511) [Medline](#)
147. M. H. O’Leary, Measurement of the isotope fractionation associated with diffusion of carbon dioxide in aqueous solution. *J. Phys. Chem.* **88**, 823–825 (1984). [doi:10.1021/j150648a041](https://doi.org/10.1021/j150648a041)
148. B. N. Popp, E. A. Laws, R. R. Bidigare, J. E. Dore, K. L. Hanson, S. G. Wakeham, Effect of phytoplankton cell geometry on carbon isotopic fractionation. *Geochim. Cosmochim. Acta* **62**, 69–77 (1998). [doi:10.1016/S0016-7037\(97\)00333-5](https://doi.org/10.1016/S0016-7037(97)00333-5)
149. C. T. Bolton, M. T. Hernández-Sánchez, M.-Á. Fuertes, S. González-Lemos, L. Abrevaya, A. Mendez-Vicente, J.-A. Flores, I. Probert, L. Giosan, J. Johnson, H. M. Stoll, Decrease in coccolithophore calcification and CO_2 since the middle Miocene. *Nat. Commun.* **7**, 10284 (2016). [doi:10.1038/ncomms10284](https://doi.org/10.1038/ncomms10284) [Medline](#)
150. M. P. S. Badger, T. B. Chalk, G. L. Foster, P. R. Bown, S. J. Gibbs, P. F. Sexton, D. N. Schmidt, H. Pälike, A. Mackensen, R. D. Pancost, Insensitivity of alkenone carbon isotopes to atmospheric CO_2 at low to moderate CO_2 levels. *Clim. Past* **15**, 539–554 (2019). [doi:10.5194/cp-15-539-2019](https://doi.org/10.5194/cp-15-539-2019)

151. Y. G. Zhang, A. Pearson, A. Benthien, L. Dong, P. Huybers, X. Liu, M. Pagani, Refining the alkenone- $p\text{CO}_2$ method I: Lessons from the Quaternary glacial cycles. *Geochim. Cosmochim. Acta* **260**, 177–191 (2019). [doi:10.1016/j.gca.2019.06.032](https://doi.org/10.1016/j.gca.2019.06.032)
152. S. R. Phelps, H. M. Stoll, C. T. Bolton, L. Beaufort, P. J. Polissar, Controls on alkenone carbon isotope fractionation in the modern ocean. *Geochem. Geophys. Geosyst.* **22**, e2021GC009658 (2021). [doi:10.1029/2021GC009658](https://doi.org/10.1029/2021GC009658)
153. J. Henderiks, M. Pagani, Coccolithophore cell size and the Paleogene decline in atmospheric CO_2 . *Earth Planet. Sci. Lett.* **269**, 576–584 (2008). [doi:10.1016/j.epsl.2008.03.016](https://doi.org/10.1016/j.epsl.2008.03.016)
154. Y. G. Zhang, M. Pagani, J. Henderiks, H. Ren, A long history of equatorial deep-water upwelling in the Pacific Ocean. *Earth Planet. Sci. Lett.* **467**, 1–9 (2017). [doi:10.1016/j.epsl.2017.03.016](https://doi.org/10.1016/j.epsl.2017.03.016)
155. P. K. Bijl, A. J. P. Houben, S. Schouten, S. M. Bohaty, A. Sluijs, G.-J. Reichart, J. S. Sinninghe Damsté, H. Brinkhuis, Transient Middle Eocene atmospheric CO_2 and temperature variations. *Science* **330**, 819–821 (2010). [doi:10.1126/science.1193654](https://doi.org/10.1126/science.1193654) [Medline](#)
156. O. Seki, G. L. Foster, D. N. Schmidt, A. Mackensen, K. Kawamura, R. D. Pancost, Alkenone and boron-based Pliocene $p\text{CO}_2$ records. *Earth Planet. Sci. Lett.* **292**, 201–211 (2010). [doi:10.1016/j.epsl.2010.01.037](https://doi.org/10.1016/j.epsl.2010.01.037)
157. G. Aloisi, Covariation of metabolic rates and cell size in coccolithophores. *Biogeosciences* **12**, 4665–4692 (2015). [doi:10.5194/bg-12-4665-2015](https://doi.org/10.5194/bg-12-4665-2015)
158. S. Blanco-Ameijeiras, H. M. Stoll, H. Zhang, B. M. Hopkinson, Influence of temperature and CO_2 on plasma-membrane permeability to CO_2 and HCO_3^- in the marine haptophytes *Emiliania huxleyi* and *Calcidiscus leptoporus* (Prymnesiophyceae). *J. Phycol.* **56**, 1283–1294 (2020). [doi:10.1111/jpy.13017](https://doi.org/10.1111/jpy.13017) [Medline](#)
159. G. D. Farquhar, T. D. Sharkey, Stomatal conductance and photosynthesis. *Annu. Rev. Plant Physiol.* **33**, 317–345 (1982). [doi:10.1146/annurev.pp.33.060182.001533](https://doi.org/10.1146/annurev.pp.33.060182.001533)
160. C. Roeske, M. H. O’Leary, Carbon isotope effects on enzyme-catalyzed carboxylation of ribulose biphosphate. *Biochemistry* **23**, 6275–6284 (1984). [doi:10.1021/bi00320a058](https://doi.org/10.1021/bi00320a058)
161. E. B. Wilkes, A. Pearson, A general model for carbon isotopes in red-lineage phytoplankton: Interplay between unidirectional processes and fractionation by RubisCO. *Geochim. Cosmochim. Acta* **265**, 163–181 (2019). [doi:10.1016/j.gca.2019.08.043](https://doi.org/10.1016/j.gca.2019.08.043)
162. E. A. Laws, R. R. Bidigare, B. N. Popp, Effect of growth rate and CO_2 concentration on carbon isotopic fractionation by the marine diatom *Phaeodactylum tricornutum*. *Limnol. Oceanogr.* **42**, 1552–1560 (1997). [doi:10.4319/lo.1997.42.7.1552](https://doi.org/10.4319/lo.1997.42.7.1552)
163. N. Andersen, P. J. Müller, G. Kirst, R. R. Schneider, “Alkenone $\delta^{13}\text{C}$ as a proxy for past $p\text{CO}_2$ in surface waters: Results from the late Quaternary Angola current” in *Use of Proxies in Paleoceanography: Examples from the South Atlantic*, G. Fischer, G. Wefer, Eds. (Springer, 1999), pp. 469–488.

164. M. P. S. Badger, C. H. Lear, R. D. Pancost, G. L. Foster, T. R. Bailey, M. J. Leng, H. A. Abels, CO₂ drawdown following the middle Miocene expansion of the Antarctic Ice Sheet. *Paleoceanography* **28**, 42–53 (2013). [doi:10.1002/palo.20015](https://doi.org/10.1002/palo.20015)
165. M. P. S. Badger, D. N. Schmidt, A. Mackensen, R. D. Pancost, High-resolution alkenone palaeobarometry indicates relatively stable *p*CO₂ during the Pliocene (3.3–2.8 Ma). *Philos. Trans. A Math. Phys. Eng. Sci.* **371**, 20130094 (2013). [doi:10.1098/rsta.2013.0094](https://doi.org/10.1098/rsta.2013.0094) [Medline](#)
166. S. W. Bae, K. E. Lee, K. Kim, Use of carbon isotopic composition of alkenone as a CO₂ proxy in the East Sea/Japan Sea. *Cont. Shelf Res.* **107**, 24–32 (2015). [doi:10.1016/j.csr.2015.07.010](https://doi.org/10.1016/j.csr.2015.07.010)
167. J. P. Jasper, J. M. Hayes, A. C. Mix, F. G. Prahl, Photosynthetic fractionation of ¹³C and concentrations of dissolved CO₂ in the central equatorial Pacific during the last 255,000 years. *Paleoceanography* **9**, 781–798 (1994). [doi:10.1029/94PA02116](https://doi.org/10.1029/94PA02116) [Medline](#)
168. M. Pagani, K. H. Freeman, M. A. Arthur, Late miocene atmospheric CO₂ concentrations and the expansion of C₄ grasses. *Science* **285**, 876–879 (1999). [doi:10.1126/science.285.5429.876](https://doi.org/10.1126/science.285.5429.876) [Medline](#)
169. M. Pagani, Z. Liu, J. LaRiviere, A. C. Ravelo, High Earth-system climate sensitivity determined from Pliocene carbon dioxide concentrations. *Nat. Geosci.* **3**, 27–30 (2010). [doi:10.1038/ngeo724](https://doi.org/10.1038/ngeo724)
170. M. Pagani, M. A. Arthur, K. H. Freeman, Variations in Miocene phytoplankton growth rates in the southwest Atlantic: Evidence for changes in ocean circulation. *Paleoceanography* **15**, 486–496 (2000). [doi:10.1029/1999PA000484](https://doi.org/10.1029/1999PA000484)
171. M. R. Palmer, G. J. Brummer, M. J. Cooper, H. Elderfield, M. J. Greaves, G. J. Reichart, S. Schouten, J. M. Yu, Multi-proxy reconstruction of surface water *p*CO₂ in the northern Arabian Sea since 29ka. *Earth Planet. Sci. Lett.* **295**, 49–57 (2010). [doi:10.1016/j.epsl.2010.03.023](https://doi.org/10.1016/j.epsl.2010.03.023)
172. J. R. Super, E. Thomas, M. Pagani, M. Huber, C. L. O'Brien, P. M. Hull, North Atlantic temperature and *p*CO₂ coupling in the early-middle Miocene. *Geology* **46**, 519–522 (2018). [doi:10.1130/G40228.1](https://doi.org/10.1130/G40228.1)
173. P. J. Müller, G. Kirst, G. Ruhland, I. von Storch, A. Rosell-Mele, Calibration of the alkenone paleotemperature index U_{37^K} based on core-tops from the eastern South Atlantic and the global ocean (60°N–60°S). *Geochim. Cosmochim. Acta* **62**, 1757–1772 (1998). [doi:10.1016/S0016-7037\(98\)00097-0](https://doi.org/10.1016/S0016-7037(98)00097-0)
174. J. E. Tierney, M. P. Tingley, A TEX₈₆ surface sediment database and extended Bayesian calibration. *Sci. Data* **2**, 150029 (2015). [doi:10.1038/sdata.2015.29](https://doi.org/10.1038/sdata.2015.29) [Medline](#)
175. Y. Rosenthal, S. Bova, X. Zhou, A user guide for choosing planktic foraminiferal Mg/Ca-temperature calibrations. *Paleoceanogr. Paleoclimatol.* **37**, e2022PA004413 (2022). [doi:10.1029/2022PA004413](https://doi.org/10.1029/2022PA004413)
176. W. G. Mook, J. C. Bommerson, W. H. Staverman, Carbon isotope fractionation between dissolved bicarbonate and gaseous carbon dioxide. *Earth Planet. Sci. Lett.* **22**, 169–176 (1974). [doi:10.1016/0012-821X\(74\)90078-8](https://doi.org/10.1016/0012-821X(74)90078-8)

177. C. S. Romanek, E. L. Grossman, J. W. Morse, Carbon isotopic fractionation in synthetic aragonite and calcite: Effects of temperature and precipitation rate. *Geochim. Cosmochim. Acta* **56**, 419–430 (1992). [doi:10.1016/0016-7037\(92\)90142-6](https://doi.org/10.1016/0016-7037(92)90142-6)
178. L. Beaufort, N. Barbarin, Y. Gally, Optical measurements to determine the thickness of calcite crystals and the mass of thin carbonate particles such as coccoliths. *Nat. Protoc.* **9**, 633–642 (2014). [doi:10.1038/nprot.2014.028](https://doi.org/10.1038/nprot.2014.028) [Medline](#)
179. L. Beaufort, M. Couapel, N. Buchet, H. Claustre, C. Goyet, Calcite production by coccolithophores in the south east Pacific Ocean. *Biogeosciences* **5**, 1101–1117 (2008). [doi:10.5194/bg-5-1101-2008](https://doi.org/10.5194/bg-5-1101-2008)
180. E. B. Wilkes, S. J. Carter, A. Pearson, CO₂-dependent carbon isotope fractionation in the dinoflagellate *Alexandrium tamarense*. *Geochim. Cosmochim. Acta* **212**, 48–61 (2017). [doi:10.1016/j.gca.2017.05.037](https://doi.org/10.1016/j.gca.2017.05.037)
181. B. Rost, U. Riebesell, S. Burkhardt, D. Sültemeyer, Carbon acquisition of bloom-forming marine phytoplankton. *Limnol. Oceanogr.* **48**, 55–67 (2003). [doi:10.4319/lo.2003.48.1.0055](https://doi.org/10.4319/lo.2003.48.1.0055)
182. L. T. Bach, L. C. M. Mackinder, K. G. Schulz, G. Wheeler, D. C. Schroeder, C. Brownlee, U. Riebesell, Dissecting the impact of CO₂ and pH on the mechanisms of photosynthesis and calcification in the coccolithophore *Emiliana huxleyi*. *New Phytol.* **199**, 121–134 (2013). [doi:10.1111/nph.12225](https://doi.org/10.1111/nph.12225) [Medline](#)
183. K. Isensee, J. Erez, H. M. Stoll, Detection of a variable intracellular acid-labile carbon pool in *Thalassiosira weissflogii* (Heterokontophyta) and *Emiliana huxleyi* (Haptophyta) in response to changes in the seawater carbon system. *Physiol. Plant.* **150**, 321–338 (2014). [doi:10.1111/ppl.12096](https://doi.org/10.1111/ppl.12096) [Medline](#)
184. H. M. Stoll, P. Ziveri, N. Shimizu, M. Conte, S. Theroux, Relationship between coccolith Sr/Ca ratios and coccolithophore production and export in the Arabian Sea and Sargasso Sea. *Deep Sea Res. Part II Top. Stud. Oceanogr.* **54**, 581–600 (2007). [doi:10.1016/j.dsr2.2007.01.003](https://doi.org/10.1016/j.dsr2.2007.01.003)
185. M. Hermoso, Y. Candelier, T. J. Browning, F. Minoletti, Environmental control of the isotopic composition of subfossil coccolith calcite: Are laboratory culture data transferable to the natural environment? *GeoResJ* **7**, 35–42 (2015). [doi:10.1016/j.grj.2015.05.002](https://doi.org/10.1016/j.grj.2015.05.002)
186. A. G. Dickson, Thermodynamics of the dissociation of boric acid in synthetic seawater from 273.15 to 318.15 K. *Deep Sea Res. A* **37**, 755–766 (1990). [doi:10.1016/0198-0149\(90\)90004-F](https://doi.org/10.1016/0198-0149(90)90004-F)
187. A. Vengosh, Y. Kolodny, A. Starinsky, A. R. Chivas, M. T. McCulloch, Coprecipitation and isotopic fractionation of boron in modern biogenic carbonates. *Geochim. Cosmochim. Acta* **55**, 2901–2910 (1991). [doi:10.1016/0016-7037\(91\)90455-E](https://doi.org/10.1016/0016-7037(91)90455-E)
188. N. G. Hemming, G. N. Hanson, Boron isotopic composition and concentration in modern marine carbonates. *Geochim. Cosmochim. Acta* **56**, 537–543 (1992). [doi:10.1016/0016-7037\(92\)90151-8](https://doi.org/10.1016/0016-7037(92)90151-8)

189. K. A. Allen, B. Hönisch, S. M. Eggins, Y. Rosenthal, Environmental controls on B/Ca in calcite tests of the tropical planktic foraminifer species *Globigerinoides ruber* and *Globigerinoides sacculifer*. *Earth Planet. Sci. Lett.* **351-352**, 270–280 (2012). [doi:10.1016/j.epsl.2012.07.004](https://doi.org/10.1016/j.epsl.2012.07.004)
190. K. A. Allen, B. Hönisch, S. M. Eggins, J. M. Yu, H. J. Spero, H. Elderfield, Controls on boron incorporation in cultured tests of the planktic foraminifer *Orbulina universa*. *Earth Planet. Sci. Lett.* **309**, 291–301 (2011). [doi:10.1016/j.epsl.2011.07.010](https://doi.org/10.1016/j.epsl.2011.07.010)
191. M. J. Henehan, J. W. B. Rae, G. L. Foster, J. Erez, K. C. Prentice, M. Kucera, H. C. Bostock, M. A. Martínez-Botí, J. A. Milton, P. A. Wilson, B. J. Marshall, T. Elliott, Calibration of the boron isotope proxy in the planktonic foraminifera *Globigerinoides ruber* for use in palaeo-CO₂ reconstruction. *Earth Planet. Sci. Lett.* **364**, 111–122 (2013). [doi:10.1016/j.epsl.2012.12.029](https://doi.org/10.1016/j.epsl.2012.12.029)
192. L. L. Haynes, B. Hönisch, K. A. Dyez, K. Holland, Y. Rosenthal, C. R. Fish, A. V. Subhas, J. W. B. Rae, Calibration of the B/Ca proxy in the planktic foraminifer *Orbulina universa* to Paleocene seawater conditions. *Paleoceanography* **32**, 580–599 (2017). [doi:10.1002/2016PA003069](https://doi.org/10.1002/2016PA003069)
193. E. L. Howes, K. Kaczmarek, M. Raitzsch, A. Mewes, N. Bijma, I. Horn, S. Misra, J.-P. Gattuso, J. Bijma, Decoupled carbonate chemistry controls on the incorporation of boron into *Orbulina universa*. *Biogeosciences* **14**, 415–430 (2017). [doi:10.5194/bg-14-415-2017](https://doi.org/10.5194/bg-14-415-2017)
194. L. L. Haynes, B. Hönisch, K. Holland, Y. Rosenthal, S. M. Eggins, Evaluating the planktic foraminiferal B/Ca proxy for application to deep time paleoceanography. *Earth Planet. Sci. Lett.* **528**, 115824 (2019). [doi:10.1016/j.epsl.2019.115824](https://doi.org/10.1016/j.epsl.2019.115824)
195. M. J. Henehan, G. L. Foster, J. W. B. Rae, K. C. Prentice, J. Erez, H. C. Bostock, B. J. Marshall, P. A. Wilson, Evaluating the utility of B/Ca ratios in planktic foraminifera as a proxy for the carbonate system: A case study of *Globigerinoides ruber*. *Geochem. Geophys. Geosyst.* **16**, 1052–1069 (2015). [doi:10.1002/2014GC005514](https://doi.org/10.1002/2014GC005514)
196. T. L. Babila, Y. Rosenthal, M. H. Conte, Evaluation of the biogeochemical controls on B/Ca of *Globigerinoides ruber* white from the Oceanic Flux Program, Bermuda. *Earth Planet. Sci. Lett.* **404**, 67–76 (2014). [doi:10.1016/j.epsl.2014.05.053](https://doi.org/10.1016/j.epsl.2014.05.053)
197. N. B. Quintana Krupinski, A. D. Russell, D. K. Pak, A. Paytan, Core-top calibration of B/Ca in Pacific Ocean *Neogloboquadrina incompta* and *Globigerina bulloides* as a surface water carbonate system proxy. *Earth Planet. Sci. Lett.* **466**, 139–151 (2017). [doi:10.1016/j.epsl.2017.03.007](https://doi.org/10.1016/j.epsl.2017.03.007)
198. K. H. Salmon, P. Anand, P. F. Sexton, M. Conte, Calcification and growth processes in planktonic foraminifera complicate the use of B/Ca and U/Ca as carbonate chemistry proxies. *Earth Planet. Sci. Lett.* **449**, 372–381 (2016). [doi:10.1016/j.epsl.2016.05.016](https://doi.org/10.1016/j.epsl.2016.05.016)
199. L. L. Haynes, B. Hönisch, The seawater carbon inventory at the Paleocene-Eocene Thermal Maximum. *Proc. Natl. Acad. Sci. U.S.A.* **117**, 24088–24095 (2020). [doi:10.1073/pnas.2003197117](https://doi.org/10.1073/pnas.2003197117) [Medline](#)

200. S. M. Sosdian, T. L. Babila, R. Greenop, G. L. Foster, C. H. Lear, Ocean carbon storage across the middle Miocene: A new interpretation for the Monterey Event. *Nat. Commun.* **11**, 134 (2020). [doi:10.1038/s41467-019-13792-0](https://doi.org/10.1038/s41467-019-13792-0) [Medline](#)
201. T. L. Babila, D. E. Penman, B. Hönisch, D. C. Kelly, T. J. Bralower, Y. Rosenthal, J. C. Zachos, Capturing the global signature of surface ocean acidification during the Palaeocene-Eocene Thermal Maximum. *Philos. Trans. A Math. Phys. Eng. Sci.* **376**, 20170072 (2018). [doi:10.1098/rsta.2017.0072](https://doi.org/10.1098/rsta.2017.0072) [Medline](#)
202. D. T. Harper, B. Hönisch, R. E. Zeebe, G. Shaffer, L. L. Haynes, E. Thomas, J. C. Zachos, The magnitude of surface ocean acidification and carbon release during Eocene Thermal Maximum 2 (ETM-2) and the Paleocene-Eocene Thermal Maximum (PETM). *Paleoceanogr. Paleoclimatol.* **35**, e2019PA003699 (2020). [doi:10.1029/2019PA003699](https://doi.org/10.1029/2019PA003699)
203. D. E. Penman, B. Hönisch, R. E. Zeebe, E. Thomas, J. C. Zachos, Rapid and sustained surface ocean acidification during the Paleocene-Eocene Thermal Maximum. *Paleoceanography* **29**, 357–369 (2014). [doi:10.1002/2014PA002621](https://doi.org/10.1002/2014PA002621)
204. A. Sanyal, N. G. Hemming, G. N. Hanson, W. S. Broecker, Evidence for a higher pH in the glacial ocean from boron isotopes in foraminifera. *Nature* **373**, 234–236 (1995). [doi:10.1038/373234a0](https://doi.org/10.1038/373234a0)
205. P. N. Pearson, M. R. Palmer, Atmospheric carbon dioxide concentrations over the past 60 million years. *Nature* **406**, 695–699 (2000). [doi:10.1038/35021000](https://doi.org/10.1038/35021000) [Medline](#)
206. F. J. Millero, Thermodynamics of the carbon dioxide system in the oceans. *Geochim. Cosmochim. Acta* **59**, 661–677 (1995). [doi:10.1016/0016-7037\(94\)00354-O](https://doi.org/10.1016/0016-7037(94)00354-O)
207. K. Klochko, A. J. Kaufman, W. Yao, R. H. Byrne, J. A. Tossell, Experimental measurement of boron isotope fractionation in seawater. *Earth Planet. Sci. Lett.* **248**, 276–285 (2006). [doi:10.1016/j.epsl.2006.05.034](https://doi.org/10.1016/j.epsl.2006.05.034)
208. O. Nir, A. Vengosh, J. S. Harkness, G. S. Dwyer, O. Lahav, Direct measurement of the boron isotope fractionation factor: Reducing the uncertainty in reconstructing ocean paleo-pH. *Earth Planet. Sci. Lett.* **414**, 1–5 (2015). [doi:10.1016/j.epsl.2015.01.006](https://doi.org/10.1016/j.epsl.2015.01.006)
209. M. P. Hain, G. L. Foster, T. Chalk, Robust constraints on past CO₂ climate forcing from the boron isotope proxy. *Paleoceanogr. Paleoclimatol.* **33**, 1099–1115 (2018). [doi:10.1029/2018PA003362](https://doi.org/10.1029/2018PA003362)
210. M. P. Hain, D. M. Sigman, J. A. Higgins, G. H. Haug, The effects of secular calcium and magnesium concentration changes on the thermodynamics of seawater acid/base chemistry: Implications for Eocene and Cretaceous ocean carbon chemistry and buffering. *Global Biogeochem. Cycles* **29**, 517–533 (2015). [doi:10.1002/2014GB004986](https://doi.org/10.1002/2014GB004986)
211. R. E. Zeebe, T. Tyrrell, History of carbonate ion concentration over the last 100 million years II: Revised calculations and new data. *Geochim. Cosmochim. Acta* **257**, 373–392 (2019). [doi:10.1016/j.gca.2019.02.041](https://doi.org/10.1016/j.gca.2019.02.041)
212. E. Anagnostou, E. H. John, K. M. Edgar, G. L. Foster, A. Ridgwell, G. N. Inglis, R. D. Pancost, D. J. Lunt, P. N. Pearson, Changing atmospheric CO₂ concentration was the primary driver of early Cenozoic climate. *Nature* **533**, 380–384 (2016). [doi:10.1038/nature17423](https://doi.org/10.1038/nature17423) [Medline](#)

213. B. Hönisch, N. G. Hemming, Ground-truthing the boron isotope-paleo-pH proxy in planktonic foraminifera shells: Partial dissolution and shell size effects. *Paleoceanography* **19**, 2004PA001026 (2004). [doi:10.1029/2004PA001026](https://doi.org/10.1029/2004PA001026)
214. A. Sanyal, J. Bijma, H. J. Spero, D. W. Lea, Empirical relationship between pH and the boron isotopic composition of *Globigerinoides sacculifer*: Implications for the boron isotope paleo-pH proxy. *Paleoceanography* **16**, 515–519 (2001). [doi:10.1029/2000PA000547](https://doi.org/10.1029/2000PA000547)
215. G. L. Foster, Seawater pH, pCO₂ and [CO²⁻₃] variations in the Caribbean Sea over the last 130 kyr: A boron isotope and B/Ca study of planktic foraminifera. *Earth Planet. Sci. Lett.* **271**, 254–266 (2008). [doi:10.1016/j.epsl.2008.04.015](https://doi.org/10.1016/j.epsl.2008.04.015)
216. M. Guillermic, S. Misra, R. Eagle, A. Villa, F. Chang, A. Tripathi, Seawater pH reconstruction using boron isotopes in multiple planktonic foraminifera species with different depth habitats and their potential to constrain pH and pCO₂ gradients. *Biogeosciences* **17**, 3487–3510 (2020). [doi:10.5194/bg-17-3487-2020](https://doi.org/10.5194/bg-17-3487-2020)
217. M. J. Henehan, G. L. Foster, H. C. Bostock, R. Greenop, B. J. Marshall, P. A. Wilson, A new boron isotope-pH calibration for *Orbulina universa*, with implications for understanding and accounting for ‘vital effects’. *Earth Planet. Sci. Lett.* **454**, 282–292 (2016). [doi:10.1016/j.epsl.2016.09.024](https://doi.org/10.1016/j.epsl.2016.09.024)
218. B. Hönisch, J. Bijma, A. D. Russell, H. J. Spero, M. R. Palmer, R. E. Zeebe, A. Eisenhauer, The influence of symbiont photosynthesis on the boron isotopic composition of foraminifera shells. *Mar. Micropaleontol.* **49**, 87–96 (2003). [doi:10.1016/S0377-8398\(03\)00030-6](https://doi.org/10.1016/S0377-8398(03)00030-6)
219. M. A. Martínez-Botí, G. Marino, G. L. Foster, P. Ziveri, M. J. Henehan, J. W. B. Rae, P. G. Mortyn, D. Vance, Boron isotope evidence for oceanic carbon dioxide leakage during the last deglaciation. *Nature* **518**, 219–222 (2015). [doi:10.1038/nature14155](https://doi.org/10.1038/nature14155) [Medline](#)
220. M. Raitzsch, J. Bijma, A. Benthien, K.-U. Richter, G. Steinhofel, M. Kučera, Boron isotope-based seasonal paleo-pH reconstruction for the Southeast Atlantic – A multispecies approach using habitat preference of planktonic foraminifera. *Earth Planet. Sci. Lett.* **487**, 138–150 (2018). [doi:10.1016/j.epsl.2018.02.002](https://doi.org/10.1016/j.epsl.2018.02.002)
221. J. Yu, D. J. R. Thornalley, J. W. B. Rae, N. I. McCave, Calibration and application of B/Ca, Cd/Ca, and δ¹¹B in *Neogloboquadrina pachyderma* (sinistral) to constrain CO₂ uptake in the subpolar North Atlantic during the last deglaciation. *Paleoceanography* **28**, 237–252 (2013). [doi:10.1002/palo.20024](https://doi.org/10.1002/palo.20024)
222. R. E. Zeebe, D. A. Wolf-Gladrow, J. Bijma, B. Hönisch, Vital effects in foraminifera do not compromise the use of δ¹¹B as a paleo-pH indicator: Evidence from modeling. *Paleoceanography* **18**, 1043 (2003). [doi:10.1029/2003PA000881](https://doi.org/10.1029/2003PA000881)
223. B. Hönisch, C. R. Fish, S. R. Phelps, L. L. Haynes, K. Dyez, K. Holland, J. Fehrenbacher, K. A. Allen, S. M. Eggins, J. I. Goes, Symbiont photosynthesis and its effect on boron proxies in planktic foraminifera. *Paleoceanogr. Paleoclimatol.* **36**, e2020PA004022 (2021). [doi:10.1029/2020PA004022](https://doi.org/10.1029/2020PA004022)

224. B. Hönlisch, N. G. Hemming, Surface ocean pH response to variations in pCO₂ through two full glacial cycles. *Earth Planet. Sci. Lett.* **236**, 305–314 (2005).
[doi:10.1016/j.epsl.2005.04.027](https://doi.org/10.1016/j.epsl.2005.04.027)
225. K. A. Dyez, B. Hönlisch, G. A. Schmidt, Early Pleistocene obliquity-scale pCO₂ variability at ~1.5 million years ago. *Paleoceanogr. Paleoclimatol.* **33**, 1270–1291 (2018).
[doi:10.1029/2018PA003349](https://doi.org/10.1029/2018PA003349) [Medline](#)
226. R. Greenop, S. M. Sosdian, M. J. Henehan, P. A. Wilson, C. H. Lear, G. L. Foster, Orbital forcing, ice volume, and CO₂ across the Oligocene-Miocene Transition. *Paleoceanogr. Paleoclimatol.* **34**, 316–328 (2019). [doi:10.1029/2018PA003420](https://doi.org/10.1029/2018PA003420)
227. T. B. Chalk, G. L. Foster, P. A. Wilson, Dynamic storage of glacial CO₂ in the Atlantic Ocean revealed by boron [CO₃²⁻] and pH records. *Earth Planet. Sci. Lett.* **510**, 1–11 (2019). [doi:10.1016/j.epsl.2018.12.022](https://doi.org/10.1016/j.epsl.2018.12.022)
228. A. K. Tripathi, C. D. Roberts, R. A. Eagle, Coupling of CO₂ and ice sheet stability over major climate transitions of the last 20 million years. *Science* **326**, 1394–1397 (2009).
[doi:10.1126/science.1178296](https://doi.org/10.1126/science.1178296) [Medline](#)
229. G. Bartoli, B. Hönlisch, R. E. Zeebe, Atmospheric CO₂ decline during the Pliocene intensification of Northern Hemisphere glaciations. *Paleoceanography* **26**, PA4213 (2011). [doi:10.1029/2010PA002055](https://doi.org/10.1029/2010PA002055)
230. T. B. Chalk, M. P. Hain, G. L. Foster, E. J. Rohling, P. F. Sexton, M. P. S. Badger, S. G. Cherry, A. P. Hasenfratz, G. H. Haug, S. L. Jaccard, A. Martínez-García, H. Pälike, R. D. Pancost, P. A. Wilson, Causes of ice age intensification across the Mid-Pleistocene Transition. *Proc. Natl. Acad. Sci. U.S.A.* **114**, 13114–13119 (2017).
[doi:10.1073/pnas.1702143114](https://doi.org/10.1073/pnas.1702143114) [Medline](#)
231. E. de la Vega, T. B. Chalk, P. A. Wilson, R. P. Bysani, G. L. Foster, Atmospheric CO₂ during the Mid-Piacenzian Warm Period and the M2 glaciation. *Sci. Rep.* **10**, 11002 (2020). [doi:10.1038/s41598-020-67154-8](https://doi.org/10.1038/s41598-020-67154-8) [Medline](#)
232. G. L. Foster, C. H. Lear, J. W. B. Rae, The evolution of pCO₂, ice volume and climate during the middle Miocene. *Earth Planet. Sci. Lett.* **341-344**, 243–254 (2012).
[doi:10.1016/j.epsl.2012.06.007](https://doi.org/10.1016/j.epsl.2012.06.007)
233. R. Greenop, G. L. Foster, P. A. Wilson, C. H. Lear, Middle Miocene climate instability associated with high-amplitude CO₂ variability. *Paleoceanography* **29**, 845–853 (2014).
[doi:10.1002/2014PA002653](https://doi.org/10.1002/2014PA002653)
234. M. J. Henehan, A. Ridgwell, E. Thomas, S. Zhang, L. Alegret, D. N. Schmidt, J. W. B. Rae, J. D. Witts, N. H. Landman, S. E. Greene, B. T. Huber, J. R. Super, N. J. Planavsky, P. M. Hull, Rapid ocean acidification and protracted Earth system recovery followed the end-Cretaceous Chicxulub impact. *Proc. Natl. Acad. Sci. U.S.A.* **116**, 22500–22504 (2019). [doi:10.1073/pnas.1905989116](https://doi.org/10.1073/pnas.1905989116) [Medline](#)
235. B. Hönlisch, N. G. Hemming, D. Archer, M. Siddall, J. F. McManus, Atmospheric carbon dioxide concentration across the mid-Pleistocene transition. *Science* **324**, 1551–1554 (2009). [doi:10.1126/science.1171477](https://doi.org/10.1126/science.1171477) [Medline](#)

236. M. A. Martínez-Botí, G. L. Foster, T. B. Chalk, E. J. Rohling, P. F. Sexton, D. J. Lunt, R. D. Pancost, M. P. S. Badger, D. N. Schmidt, Plio-Pleistocene climate sensitivity evaluated using high-resolution CO₂ records. *Nature* **518**, 49–54 (2015). [doi:10.1038/nature14145](https://doi.org/10.1038/nature14145) [Medline](#)
237. P. N. Pearson, G. L. Foster, B. S. Wade, Atmospheric carbon dioxide through the Eocene-Oligocene climate transition. *Nature* **461**, 1110–1113 (2009). [doi:10.1038/nature08447](https://doi.org/10.1038/nature08447) [Medline](#)
238. M. Raitzsch, J. Bijma, T. Bickert, M. Schulz, A. Holbourn, M. Kučera, Atmospheric carbon dioxide variations across the middle Miocene climate transition. *Clim. Past* **17**, 703–719 (2021). [doi:10.5194/cp-17-703-2021](https://doi.org/10.5194/cp-17-703-2021)
239. S. M. Sosdian, R. Greenop, M. P. Hain, G. L. Foster, P. N. Pearson, C. H. Lear, Constraining the evolution of Neogene ocean carbonate chemistry using the boron isotope pH proxy. *Earth Planet. Sci. Lett.* **498**, 362–376 (2018). [doi:10.1016/j.epsl.2018.06.017](https://doi.org/10.1016/j.epsl.2018.06.017)
240. L. B. Stap, B. de Boer, M. Ziegler, R. Bintanja, L. J. Lourens, R. S. W. van de Wal, CO₂ over the past 5 million years: Continuous simulation and new $\delta^{11}\text{B}$ -based proxy data. *Earth Planet. Sci. Lett.* **439**, 1–10 (2016). [doi:10.1016/j.epsl.2016.01.022](https://doi.org/10.1016/j.epsl.2016.01.022)
241. K. A. Allen, B. Hönisch, The planktic foraminiferal B/Ca proxy for seawater carbonate chemistry: A critical evaluation. *Earth Planet. Sci. Lett.* **345-348**, 203–211 (2012). [doi:10.1016/j.epsl.2012.06.012](https://doi.org/10.1016/j.epsl.2012.06.012)
242. M. Guillermic, S. Misra, R. Eagle, A. Tripathi, Atmospheric CO₂ estimates for the Miocene to Pleistocene based on foraminiferal $\delta^{11}\text{B}$ at Ocean Drilling Program Sites 806 and 807 in the Western Equatorial Pacific. *Clim. Past* **18**, 183–207 (2022). [doi:10.5194/cp-18-183-2022](https://doi.org/10.5194/cp-18-183-2022)
243. S. T. Brennan, T. K. Lowenstein, D. I. Cendón, The major-ion composition of Cenozoic seawater: The past 36 million years from fluid inclusions in marine halite. *Am. J. Sci.* **313**, 713–775 (2013). [doi:10.2475/08.2013.01](https://doi.org/10.2475/08.2013.01)
244. J. Horita, H. Zimmermann, H. D. Holland, Chemical evolution of seawater during the Phanerozoic. *Geochim. Cosmochim. Acta* **66**, 3733–3756 (2002). [doi:10.1016/S0016-7037\(01\)00884-5](https://doi.org/10.1016/S0016-7037(01)00884-5)
245. H. Pälike, M. W. Lyle, H. Nishi, I. Raffi, A. Ridgwell, K. Gamage, A. Klaus, G. Acton, L. Anderson, J. Backman, J. Baldauf, C. Beltran, S. M. Bohaty, P. Bown, W. Busch, J. E. T. Channell, C. O. J. Chun, M. Delaney, P. Dewangan, T. Dunkley Jones, K. M. Edgar, H. Evans, P. Fitch, G. L. Foster, N. Gussone, H. Hasegawa, E. C. Hathorne, H. Hayashi, J. O. Herrle, A. Holbourn, S. Hovan, K. Hyeong, K. Iijima, T. Ito, S. Kamikuri, K. Kimoto, J. Kuroda, L. Leon-Rodriguez, A. Malinverno, T. C. Moore Jr., B. H. Murphy, D. P. Murphy, H. Nakamura, K. Ogane, C. Ohneiser, C. Richter, R. Robinson, E. J. Rohling, O. Romero, K. Sawada, H. Scher, L. Schneider, A. Sluijs, H. Takata, J. Tian, A. Tsujimoto, B. S. Wade, T. Westerhold, R. Wilkens, T. Williams, P. A. Wilson, Y. Yamamoto, S. Yamamoto, T. Yamazaki, R. E. Zeebe, A Cenozoic record of the equatorial Pacific carbonate compensation depth. *Nature* **488**, 609–614 (2012). [doi:10.1038/nature11360](https://doi.org/10.1038/nature11360) [Medline](#)

246. R. Greenop, M. P. Hain, S. M. Sosdian, K. I. C. Oliver, P. Goodwin, T. B. Chalk, C. H. Lear, P. A. Wilson, G. L. Foster, A record of Neogene seawater $\delta^{11}\text{B}$ reconstructed from paired $\delta^{11}\text{B}$ analyses on benthic and planktic foraminifera. *Clim. Past* **13**, 149–170 (2017). [doi:10.5194/cp-13-149-2017](https://doi.org/10.5194/cp-13-149-2017)
247. S. Spezzaferri, R. K. Olsson, C. Hemleben, Taxonomy, biostratigraphy, and phylogeny of Oligocene to lower Miocene *Globigerinoides* and *Trilobatus*. *Cushman Found. Foraminifer. Res. Spec. Pub.* **46**, 269–306 (2018).
248. D. E. Gaskell, P. M. Hull, Symbiont arrangement and metabolism can explain high $\delta^{13}\text{C}$ in Eocene planktonic foraminifera. *Geology* **47**, 1156–1160 (2019). [doi:10.1130/G46304.1](https://doi.org/10.1130/G46304.1)
249. H. Takagi, K. Kimoto, T. Fujiki, A. Kurasawa, K. Moriya, H. Hirano, Ontogenetic dynamics of photosymbiosis in cultured planktic foraminifera revealed by fast repetition rate fluorometry. *Mar. Micropaleontol.* **122**, 44–52 (2016). [doi:10.1016/j.marmicro.2015.10.003](https://doi.org/10.1016/j.marmicro.2015.10.003)
250. H. Takagi, K. Kimoto, T. Fujiki, H. Saito, C. Schmidt, M. Kucera, K. Moriya, Characterizing photosymbiosis in modern planktonic foraminifera. *Biogeosciences* **16**, 3377–3396 (2019). [doi:10.5194/bg-16-3377-2019](https://doi.org/10.5194/bg-16-3377-2019)
251. J. E. Burke, W. Renema, M. J. Hennehan, L. E. Elder, C. V. Davis, A. E. Maas, G. L. Foster, R. Schiebel, P. M. Hull, Factors influencing test porosity in planktonic foraminifera. *Biogeosciences* **15**, 6607–6619 (2018). [doi:10.5194/bg-15-6607-2018](https://doi.org/10.5194/bg-15-6607-2018)
252. P. N. Pearson, M. R. Palmer, Middle Eocene seawater pH and atmospheric carbon dioxide concentrations. *Science* **284**, 1824–1826 (1999). [doi:10.1126/science.284.5421.1824](https://doi.org/10.1126/science.284.5421.1824) [Medline](#)
253. M. Raitzsch, B. Hönisch, Cenozoic boron isotope variations in benthic foraminifera. *Geology* **41**, 591–594 (2013). [doi:10.1130/G34031.1](https://doi.org/10.1130/G34031.1)
254. G. Paris, J. Gaillardet, P. Louvat, Geological evolution of seawater boron isotopic composition recorded in evaporites. *Geology* **38**, 1035–1038 (2010). [doi:10.1130/G31321.1](https://doi.org/10.1130/G31321.1)
255. D. Lemarchand, J. Gaillardet, E. Lewin, C. J. Allègre, The influence of rivers on marine boron isotopes and implications for reconstructing past ocean pH. *Nature* **408**, 951–954 (2000). [doi:10.1038/35050058](https://doi.org/10.1038/35050058) [Medline](#)
256. D. Lemarchand, J. Gaillardet, E. Lewin, C. J. Allegre, Boron isotope systematics in large rivers: Implications for the marine boron budget and paleo-pH reconstruction over the Cenozoic. *Chem. Geol.* **190**, 123–140 (2002). [doi:10.1016/S0009-2541\(02\)00114-6](https://doi.org/10.1016/S0009-2541(02)00114-6)
257. L. Simon, C. Lécuyer, C. Maréchal, N. Coltice, Modelling the geochemical cycle of boron: Implications for the long-term $\delta^{11}\text{B}$ evolution of seawater and oceanic crust. *Chem. Geol.* **225**, 61–76 (2006). [doi:10.1016/j.chemgeo.2005.08.011](https://doi.org/10.1016/j.chemgeo.2005.08.011)
258. T. K. Lowenstein, B. Kendall, A. D. Anbar, “8.21 - The geologic history of seawater” in *Treatise on Geochemistry*, vol. 8, H. D. Holland, K. K. Turekian, Eds. (Elsevier, ed. 2, 2014), pp. 569–622.

259. A. Ridgwell, R. E. Zeebe, The role of the global carbonate cycle in the regulation and evolution of the Earth system. *Earth Planet. Sci. Lett.* **234**, 299–315 (2005). [doi:10.1016/j.epsl.2005.03.006](https://doi.org/10.1016/j.epsl.2005.03.006)
260. R. E. Zeebe, P. Westbroek, A simple model for the CaCO₃ saturation state of the ocean: The “Strangelove,” the “Neritan,” and the “Cretan” Ocean. *Geochem. Geophys. Geosyst.* **4**, 1104 (2003). [doi:10.1029/2003GC000538](https://doi.org/10.1029/2003GC000538)
261. N. S. Lloyd, A. Y. Sadekov, S. Misra, Application of 10¹³ ohm Faraday cup current amplifiers for boron isotopic analyses by solution mode and laser ablation multicollector inductively coupled plasma mass spectrometry. *Rapid Commun. Mass Spectrom.* **32**, 9–18 (2018). [doi:10.1002/rcm.8009](https://doi.org/10.1002/rcm.8009) [Medline](#)
262. A. Sadekov, N. S. Lloyd, S. Misra, J. Trotter, J. D’Olivo, M. McCulloch, Accurate and precise microscale measurements of boron isotope ratios in calcium carbonates using laser ablation multicollector-ICPMS. *J. Anal. At. Spectrom.* **34**, 550–560 (2019). [doi:10.1039/C8JA00444G](https://doi.org/10.1039/C8JA00444G)
263. C. D. Standish, T. B. Chalk, T. L. Babila, J. A. Milton, M. R. Palmer, G. L. Foster, The effect of matrix interferences on *in situ* boron isotope analysis by laser ablation multicollector inductively coupled plasma mass spectrometry. *Rapid Commun. Mass Spectrom.* **33**, 959–968 (2019). [doi:10.1002/rcm.8432](https://doi.org/10.1002/rcm.8432) [Medline](#)
264. D. Evans, A. Gerdes, D. Coenen, H. R. Marschall, W. Müller, Accurate correction for the matrix interference on laser ablation MC-ICPMS boron isotope measurements in CaCO₃ and silicate matrices. *J. Anal. At. Spectrom.* **36**, 1607–1617 (2021). [doi:10.1039/D1JA00073J](https://doi.org/10.1039/D1JA00073J)
265. A. S. Porter, C. E. Evans-FitzGerald, C. Yiotis, I. P. Montañez, J. C. McElwain, Testing the accuracy of new paleoatmospheric CO₂ proxies based on plant stable carbon isotopic composition and stomatal traits in a range of simulated paleoatmospheric O₂:CO₂ ratios. *Geochim. Cosmochim. Acta* **259**, 69–90 (2019). [doi:10.1016/j.gca.2019.05.037](https://doi.org/10.1016/j.gca.2019.05.037)
266. R. S. Barclay, J. C. McElwain, B. B. Sageman, Carbon sequestration activated by a volcanic CO₂ pulse during Ocean Anoxic Event 2. *Nat. Geosci.* **3**, 205–208 (2010). [doi:10.1038/ngeo757](https://doi.org/10.1038/ngeo757)
267. M. Steinthorsdottir, A. J. Jeram, J. C. McElwain, Extremely elevated CO₂ concentrations at the Triassic/Jurassic boundary. *Palaeogeogr. Palaeoclimatol. Palaeoecol.* **308**, 418–432 (2011). [doi:10.1016/j.palaeo.2011.05.050](https://doi.org/10.1016/j.palaeo.2011.05.050)
268. J. C. McElwain, F. E. Mayle, D. J. Beerling, Stomatal evidence for a decline in atmospheric CO₂ concentration during the Younger Dryas stadial: A comparison with Antarctic ice core records. *J. Quaternary Sci.* **17**, 21–29 (2002). [doi:10.1002/jqs.664](https://doi.org/10.1002/jqs.664)
269. M. Steinthorsdottir, H. K. Coxall, A. M. de Boer, M. Huber, N. Barbolini, C. D. Bradshaw, N. J. Burls, S. J. Feakins, E. Gasson, J. Henderiks, A. E. Holbourn, S. Kiel, M. J. Kohn, G. Knorr, W. M. Kürschner, C. H. Lear, D. Liebrand, D. J. Lunt, T. Mörs, P. N. Pearson, M. J. Pound, H. Stoll, C. A. E. Strömberg, The Miocene: The future of the past. *Paleoceanogr. Paleoclimatol.* **36**, e2020PA004037 (2021). [doi:10.1029/2020PA004037](https://doi.org/10.1029/2020PA004037)
270. M. Haworth, C. Elliott-Kingston, J. C. McElwain, Stomatal control as a driver of plant evolution. *J. Exp. Bot.* **62**, 2419–2423 (2011). [doi:10.1093/jxb/err086](https://doi.org/10.1093/jxb/err086) [Medline](#)

271. M. Haworth, J. Heath, J. C. McElwain, Differences in the response sensitivity of stomatal index to atmospheric CO₂ among four genera of Cupressaceae conifers. *Ann. Bot.* **105**, 411–418 (2010). [doi:10.1093/aob/mcp309](https://doi.org/10.1093/aob/mcp309) [Medline](#)
272. M. Haworth, D. Killi, A. Materassi, A. Raschi, Coordination of stomatal physiological behavior and morphology with carbon dioxide determines stomatal control. *Am. J. Bot.* **102**, 677–688 (2015). [doi:10.3732/ajb.1400508](https://doi.org/10.3732/ajb.1400508) [Medline](#)
273. D. J. Beerling, A. Fox, C. W. Anderson, Quantitative uncertainty analyses of ancient atmospheric CO₂ estimates from fossil leaves. *Am. J. Sci.* **309**, 775–787 (2009). [doi:10.2475/09.2009.01](https://doi.org/10.2475/09.2009.01)
274. J.-Q. Liang, Q. Leng, D. F. Höfig, G. Niu, L. Wang, D. L. Royer, K. Burke, L. Xiao, Y. G. Zhang, H. Yang, Constraining conifer physiological parameters in leaf gas-exchange models for ancient CO₂ reconstruction. *Global Planet. Change* **209**, 103737 (2022). [doi:10.1016/j.gloplacha.2022.103737](https://doi.org/10.1016/j.gloplacha.2022.103737)
275. J. Liang, Q. Leng, L. Xiao, D. F. Höfig, D. L. Royer, Y. G. Zhang, H. Yang, Early Miocene redwood fossils from Inner Mongolia: CO₂ reconstructions and paleoclimate effects of a low Mongolian plateau. *Rev. Palaeobot. Palynol.* **305**, 104743 (2022). [doi:10.1016/j.revpalbo.2022.104743](https://doi.org/10.1016/j.revpalbo.2022.104743)
276. D. Stults, F. Wagner-Cremer, B. Axsmith, Atmospheric paleo-CO₂ estimates based on *Taxodium distichum* (Cupressaceae) fossils from the Miocene and Pliocene of Eastern North America. *Palaeogeogr. Palaeoclimatol. Palaeoecol.* **309**, 327–332 (2011). [doi:10.1016/j.palaeo.2011.06.017](https://doi.org/10.1016/j.palaeo.2011.06.017)
277. R. S. Barclay, S. L. Wing, Improving the *Ginkgo* CO₂ barometer: Implications for the early Cenozoic atmosphere. *Earth Planet. Sci. Lett.* **439**, 158–171 (2016). [doi:10.1016/j.epsl.2016.01.012](https://doi.org/10.1016/j.epsl.2016.01.012)
278. D. J. Beerling, B. H. Lomax, D. L. Royer, G. R. Upchurch Jr., L. R. Kump, An atmospheric pCO₂ reconstruction across the Cretaceous-Tertiary boundary from leaf megafossils. *Proc. Natl. Acad. Sci. U.S.A.* **99**, 7836–7840 (2002). [doi:10.1073/pnas.122573099](https://doi.org/10.1073/pnas.122573099) [Medline](#)
279. D. J. Beerling, Low atmospheric CO₂ levels during the Permo-Carboniferous glaciation inferred from fossil lycopsids. *Proc. Natl. Acad. Sci. U.S.A.* **99**, 12567–12571 (2002). [doi:10.1073/pnas.202304999](https://doi.org/10.1073/pnas.202304999) [Medline](#)
280. G. Doria, D. L. Royer, A. P. Wolfe, A. Fox, J. A. Westgate, D. J. Beerling, Declining atmospheric CO₂ during the late Middle Eocene climate transition. *Am. J. Sci.* **311**, 63–75 (2011). [doi:10.2475/01.2011.03](https://doi.org/10.2475/01.2011.03)
281. D. R. Greenwood, M. J. Scarr, D. C. Christophel, Leaf stomatal frequency in the Australian tropical rainforest tree *Neolitsea dealbata* (Lauraceae) as a proxy measure of atmospheric pCO₂. *Palaeogeogr. Palaeoclimatol. Palaeoecol.* **196**, 375–393 (2003). [doi:10.1016/S0031-0182\(03\)00465-6](https://doi.org/10.1016/S0031-0182(03)00465-6)
282. J. B. Kowalczyk, D. L. Royer, I. M. Miller, C. W. Anderson, D. J. Beerling, P. J. Franks, M. Grein, W. Konrad, A. Roth-Nebelsick, S. A. Bowring, K. R. Johnson, J. Ramezani, Multiple proxy estimates of atmospheric CO₂ from an early Paleocene rainforest. *Paleoceanogr. Paleoclimatol.* **33**, 1427–1438 (2018). [doi:10.1029/2018PA003356](https://doi.org/10.1029/2018PA003356)

283. W. M. Kürschner, F. Wagner, D. L. Dilcher, H. Visscher, “Using fossil leaves for the reconstruction of Cenozoic paleoatmospheric CO₂ concentrations” in *Geological Perspectives of Global Climate Change*, L. C. Gerhard, W. E. Harrison, B. M. Hanson, Eds., vol. 47 of *APPG Studies in Geology* (The American Association of Petroleum Geologists, 2001), pp. 169–189.
284. D. P. Maxbauer, D. L. Royer, B. A. LePage, High Arctic forests during the middle Eocene supported by moderate levels of atmospheric CO₂. *Geology* **42**, 1027–1030 (2014). [doi:10.1130/G36014.1](https://doi.org/10.1130/G36014.1)
285. G. J. Retallack, Greenhouse crises of the past 300 million years. *Geol. Soc. Am. Bull.* **121**, 1441–1455 (2009). [doi:10.1130/B26341.1](https://doi.org/10.1130/B26341.1)
286. D. L. Royer, R. A. Berner, D. J. Beerling, Phanerozoic atmospheric CO₂ change: Evaluating geochemical and paleobiological approaches. *Earth Sci. Rev.* **54**, 349–392 (2001). [doi:10.1016/S0012-8252\(00\)00042-8](https://doi.org/10.1016/S0012-8252(00)00042-8)
287. D. L. Royer, “Estimating latest Cretaceous and Tertiary atmospheric CO₂ from stomatal indices” in *Causes and Consequences of Globally Warm Climates in the Early Paleogene*, S. L. Wing, P. D. Gingerich, B. Schmitz, E. Thomas, Eds., vol. 369 of *GSA Special Papers* (Geological Society of America, 2003), pp. 79–93.
288. R. Y. Smith, D. R. Greenwood, J. F. Basinger, Estimating paleoatmospheric *p*CO₂ during the Early Eocene Climatic Optimum from stomatal frequency of *Ginkgo*, Okanagan Highlands, British Columbia, Canada. *Palaeogeogr. Palaeoclimatol. Palaeoecol.* **293**, 120–131 (2010). [doi:10.1016/j.palaeo.2010.05.006](https://doi.org/10.1016/j.palaeo.2010.05.006)
289. M. Steinthorsdottir, A. S. Porter, A. Holohan, L. Kunzmann, M. Collinson, J. C. McElwain, Fossil plant stomata indicate decreasing atmospheric CO₂ prior to the Eocene–Oligocene boundary. *Clim. Past* **12**, 439–454 (2016). [doi:10.5194/cp-12-439-2016](https://doi.org/10.5194/cp-12-439-2016)
290. M. Steinthorsdottir, V. Vajda, M. Pole, Global trends of *p*CO₂ across the Cretaceous–Paleogene boundary supported by the first Southern Hemisphere stomatal proxy-based *p*CO₂ reconstruction. *Palaeogeogr. Palaeoclimatol. Palaeoecol.* **464**, 143–152 (2016). [doi:10.1016/j.palaeo.2016.04.033](https://doi.org/10.1016/j.palaeo.2016.04.033)
291. M. Steinthorsdottir, V. Vajda, M. Pole, Significant transient *p*CO₂ perturbation at the New Zealand Oligocene–Miocene transition recorded by fossil plant stomata. *Palaeogeogr. Palaeoclimatol. Palaeoecol.* **515**, 152–161 (2019). [doi:10.1016/j.palaeo.2018.01.039](https://doi.org/10.1016/j.palaeo.2018.01.039)
292. M. Steinthorsdottir, V. Vajda, M. Pole, G. Holdgate, Moderate levels of Eocene *p*CO₂ indicated by Southern Hemisphere fossil plant stomata. *Geology* **47**, 914–918 (2019). [doi:10.1130/G46274.1](https://doi.org/10.1130/G46274.1)
293. M. Steinthorsdottir, P. E. Jardine, W. C. Rember, Near-future *p*CO₂ during the hot Miocene climatic optimum. *Paleoceanogr. Paleoclimatol.* **36**, e2020PA003900 (2021). [doi:10.1029/2020PA003900](https://doi.org/10.1029/2020PA003900)
294. J. Van Der Burgh, H. Visscher, D. L. Dilcher, W. M. Kürschner, Paleoatmospheric signatures in Neogene fossil leaves. *Science* **260**, 1788–1790 (1993). [doi:10.1126/science.260.5115.1788](https://doi.org/10.1126/science.260.5115.1788) [Medline](#)

295. Y. Wang, A. Momohara, L. Wang, J. Lebreton-Anberrée, Z. Zhou, Evolutionary history of atmospheric CO₂ during the late Cenozoic from fossilized *Metasequoia* needles. *PLOS ONE* **10**, e0130941 (2015). [doi:10.1371/journal.pone.0130941](https://doi.org/10.1371/journal.pone.0130941) [Medline](#)
296. Y. Wang, L. Wang, A. Momohara, Q. Leng, Y.-J. Huang, The Paleogene atmospheric CO₂ concentrations reconstructed using stomatal analysis of fossil *Metasequoia* needles. *Palaeoworld* **29**, 744–751 (2020). [doi:10.1016/j.palwor.2020.03.002](https://doi.org/10.1016/j.palwor.2020.03.002)
297. X. Y. Liu, Q. Gao, M. Han, J. H. Jin, Estimates of late middle Eocene pCO₂ based on stomatal density of modern and fossil *Nageia* leaves. *Clim. Past* **12**, 241–253 (2016). [doi:10.5194/cp-12-241-2016](https://doi.org/10.5194/cp-12-241-2016)
298. J. C. McElwain, Do fossil plants signal palaeoatmospheric carbon dioxide concentration in the geological past? *Philos. Trans. R. Soc. Lond. B Biol. Sci.* **353**, 83–96 (1998). [doi:10.1098/rstb.1998.0193](https://doi.org/10.1098/rstb.1998.0193)
299. B.-N. Sun, S.-T. Ding, J.-Y. Wu, C. Dong, S. Xie, Z.-C. Lin, Carbon isotope and stomatal data of Late Pliocene Betulaceae leaves from SW China: Implications for palaeoatmospheric CO₂-levels. *Turk. J. Earth Sci.* **21**, 237–250 (2012). [doi:10.3906/yer-1003-42](https://doi.org/10.3906/yer-1003-42)
300. D. L. Royer, Stomatal density and stomatal index as indicators of paleoatmospheric CO₂ concentration. *Rev. Palaeobot. Palynol.* **114**, 1–28 (2001). [doi:10.1016/S0034-6667\(00\)00074-9](https://doi.org/10.1016/S0034-6667(00)00074-9) [Medline](#)
301. D. J. Beerling, “Evolutionary responses of land plants to atmospheric CO₂” in *A History of Atmospheric CO₂ and Its Effects on Plants, Animals, and Ecosystems*, J. R. Ehleringer, T. E. Cerling, M. D. Dearing, Eds., vol. 177 of *Ecological Studies* (Springer, 2005), pp. 114–132.
302. F. Wagner, L. L. R. Kouwenberg, T. B. van Hoof, H. Visscher, Reproducibility of Holocene atmospheric CO₂ records based on stomatal frequency. *Quat. Sci. Rev.* **23**, 1947–1954 (2004). [doi:10.1016/j.quascirev.2004.04.003](https://doi.org/10.1016/j.quascirev.2004.04.003)
303. M. Rundgren, S. Björck, Late-glacial and early Holocene variations in atmospheric CO₂ concentration indicated by high-resolution stomatal index data. *Earth Planet. Sci. Lett.* **213**, 191–204 (2003). [doi:10.1016/S0012-821X\(03\)00324-8](https://doi.org/10.1016/S0012-821X(03)00324-8)
304. W. M. Kürschner, J. van der Burgh, H. Visscher, D. L. Dilcher, Oak leaves as biosensors of late Neogene and early Pleistocene paleoatmospheric CO₂ concentrations. *Mar. Micropaleontol.* **27**, 299–312 (1996). [doi:10.1016/0377-8398\(95\)00067-4](https://doi.org/10.1016/0377-8398(95)00067-4)
305. D. L. Royer, K. M. Moynihan, M. L. McKee, L. Londoño, P. J. Franks, Sensitivity of a leaf gas-exchange model for estimating paleoatmospheric CO₂ concentration. *Clim. Past* **15**, 795–809 (2019). [doi:10.5194/cp-15-795-2019](https://doi.org/10.5194/cp-15-795-2019)
306. W. G. Chaloner, J. McElwain, The fossil plant record and global climatic change. *Rev. Palaeobot. Palynol.* **95**, 73–82 (1997). [doi:10.1016/S0034-6667\(96\)00028-0](https://doi.org/10.1016/S0034-6667(96)00028-0)
307. D. J. Beerling, D. L. Royer, Fossil plants as indicators of the Phanerozoic global carbon cycle. *Annu. Rev. Earth Planet. Sci.* **30**, 527–556 (2002). [doi:10.1146/annurev.earth.30.091201.141413](https://doi.org/10.1146/annurev.earth.30.091201.141413)

308. M. Slodownik, V. Vajda, M. Steinhorsdottir, Fossil seed fern *Lepidopteris ottonis* from Sweden records increasing CO₂ concentration during the end-Triassic extinction event. *Palaeogeogr. Palaeoclimatol. Palaeoecol.* **564**, 110157 (2021). [doi:10.1016/j.palaeo.2020.110157](https://doi.org/10.1016/j.palaeo.2020.110157)
309. I. P. Montañez, J. C. McElwain, C. J. Poulsen, J. D. White, W. A. DiMichele, J. P. Wilson, G. Griggs, M. T. Hren, Climate, *p*CO₂ and terrestrial carbon cycle linkages during late Palaeozoic glacial–interglacial cycles. *Nat. Geosci.* **9**, 824–828 (2016). [doi:10.1038/ngeo2822](https://doi.org/10.1038/ngeo2822)
310. M. Huber, R. Caballero, The early Eocene equable climate problem revisited. *Clim. Past* **7**, 603–633 (2011). [doi:10.5194/cp-7-603-2011](https://doi.org/10.5194/cp-7-603-2011)
311. C. Elliott-Kingston, M. Haworth, J. M. Yearsley, S. P. Batke, T. Lawson, J. C. McElwain, Does size matter? Atmospheric CO₂ may be a stronger driver of stomatal closing rate than stomatal size in taxa that diversified under low CO₂. *Front. Plant Sci.* **7**, 1253 (2016). [doi:10.3389/fpls.2016.01253](https://doi.org/10.3389/fpls.2016.01253) [Medline](#)
312. P. J. Franks, D. L. Royer, D. J. Beerling, P. K. Van de Water, D. J. Cantrill, M. M. Barbour, J. A. Berry, New constraints on atmospheric CO₂ concentration for the Phanerozoic. *Geophys. Res. Lett.* **41**, 4685–4694 (2014). [doi:10.1002/2014GL060457](https://doi.org/10.1002/2014GL060457)
313. W. Konrad, A. Roth-Nebelsick, M. Grein, Modelling of stomatal density response to atmospheric CO₂. *J. Theor. Biol.* **253**, 638–658 (2008). [doi:10.1016/j.jtbi.2008.03.032](https://doi.org/10.1016/j.jtbi.2008.03.032) [Medline](#)
314. B. J. Tipple, S. R. Meyers, M. Pagani, Carbon isotope ratio of Cenozoic CO₂ : A comparative evaluation of available geochemical proxies. *Paleoceanography* **25**, PA3202 (2010). [doi:10.1029/2009PA001851](https://doi.org/10.1029/2009PA001851)
315. P. J. Franks, M. A. Adams, J. S. Amthor, M. M. Barbour, J. A. Berry, D. S. Ellsworth, G. D. Farquhar, O. Ghannoum, J. Lloyd, N. McDowell, R. J. Norby, D. T. Tissue, S. von Caemmerer, Sensitivity of plants to changing atmospheric CO₂ concentration: From the geological past to the next century. *New Phytol.* **197**, 1077–1094 (2013). [doi:10.1111/nph.12104](https://doi.org/10.1111/nph.12104) [Medline](#)
316. W. Konrad, G. Katul, A. Roth-Nebelsick, M. Grein, A reduced order model to analytically infer atmospheric CO₂ concentration from stomatal and climate data. *Adv. Water Resour.* **104**, 145–157 (2017). [doi:10.1016/j.advwatres.2017.03.018](https://doi.org/10.1016/j.advwatres.2017.03.018)
317. J. N. Milligan, D. L. Royer, P. J. Franks, G. R. Upchurch, M. L. McKee, No evidence for a large atmospheric CO₂ spike across the Cretaceous–Paleogene boundary. *Geophys. Res. Lett.* **46**, 3462–3472 (2019). [doi:10.1029/2018GL081215](https://doi.org/10.1029/2018GL081215)
318. J. N. Milligan, A. G. Flynn, J. B. Kowalczyk, R. S. Barclay, J. Geng, D. L. Royer, D. J. Peppe, Moderate to elevated atmospheric CO₂ during the early Paleocene recorded by *Platanites* leaves of the San Juan Basin, New Mexico. *Paleoceanogr. Paleoclimatol.* **37**, e2021PA004408 (2022). [doi:10.1029/2021PA004408](https://doi.org/10.1029/2021PA004408)
319. T. Reichgelt, W. J. D’Andrea, B. Fox, Abrupt plant physiological changes in southern New Zealand at the termination of the Mi-1 event reflect shifts in hydroclimate and *p*CO₂. *Earth Planet. Sci. Lett.* **455**, 115–124 (2016). [doi:10.1016/j.epsl.2016.09.026](https://doi.org/10.1016/j.epsl.2016.09.026)

320. T. Reichgelt, W. J. D'Andrea, A. C. Valdivia-McCarthy, B. R. S. Fox, J. M. Bannister, J. G. Conran, W. G. Lee, D. E. Lee, Elevated CO₂, increased leaf-level productivity, and water-use efficiency during the early Miocene. *Clim. Past* **16**, 1509–1521 (2020). [doi:10.5194/cp-16-1509-2020](https://doi.org/10.5194/cp-16-1509-2020)
321. T. Tesfamichael, B. Jacobs, N. Tabor, L. Michel, E. Currano, M. Feseha, R. Barclay, J. Kappelman, M. Schmitz, Settling the issue of “decoupling” between atmospheric carbon dioxide and global temperature: [CO₂]_{atm} reconstructions across the warming Paleogene-Neogene divide. *Geology* **45**, 999–1002 (2017). [doi:10.1130/G39048.1](https://doi.org/10.1130/G39048.1)
322. B. Erdei, T. Utescher, L. Hably, J. Tamás, A. Roth-Nebelsick, M. Grein, Early Oligocene continental climate of the Palaeogene basin (Hungary and Slovenia) and the surrounding area. *Turk. J. Earth Sci.* **21**, 153–186 (2012). [doi:10.3906/yer-1005-29](https://doi.org/10.3906/yer-1005-29)
323. M. Grein, W. Konrad, V. Wilde, T. Utescher, A. Roth-Nebelsick, Reconstruction of atmospheric CO₂ during the early middle Eocene by application of a gas exchange model to fossil plants from the Messel Formation, Germany. *Palaeogeogr. Palaeoclimatol. Palaeoecol.* **309**, 383–391 (2011). [doi:10.1016/j.palaeo.2011.07.008](https://doi.org/10.1016/j.palaeo.2011.07.008)
324. K. Moraweck, M. Grein, W. Konrad, J. Kvaček, J. Kova-Eder, C. Neinhuis, C. Traiser, L. Kunzmann, Leaf traits of long-ranging Paleogene species and their relationship with depositional facies, climate and atmospheric CO₂ level. *Palaeontographica Abt. B Paläophytol. Palaeobot. Palaeophytol.* **298**, 93–172 (2019). [doi:10.1127/palb/2019/0062](https://doi.org/10.1127/palb/2019/0062)
325. A. Roth-Nebelsick, C. Oehm, M. Grein, T. Utescher, L. Kunzmann, J.-P. Friedrich, W. Konrad, Stomatal density and index data of *Platanus neptuni* leaf fossils and their evaluation as a CO₂ proxy for the Oligocene. *Rev. Palaeobot. Palynol.* **206**, 1–9 (2014). [doi:10.1016/j.revpalbo.2014.03.001](https://doi.org/10.1016/j.revpalbo.2014.03.001)
326. B.-N. Sun, Q.-J. Wang, W. Konrad, F.-J. Ma, J.-L. Dong, Z.-X. Wang, Reconstruction of atmospheric CO₂ during the Oligocene based on leaf fossils from the Ningming Formation in Guangxi, China. *Palaeogeogr. Palaeoclimatol. Palaeoecol.* **467**, 5–15 (2017). [doi:10.1016/j.palaeo.2016.09.015](https://doi.org/10.1016/j.palaeo.2016.09.015)
327. A. P. Wolfe, A. V. Reyes, D. L. Royer, D. R. Greenwood, G. Doria, M. H. Gagen, P. A. Siver, J. A. Westgate, Middle Eocene CO₂ and climate reconstructed from the sediment fill of a subarctic kimberlite maar. *Geology* **45**, 619–622 (2017). [doi:10.1130/G39002.1](https://doi.org/10.1130/G39002.1)
328. L. Londoño, D. L. Royer, C. Jaramillo, J. Escobar, D. A. Foster, A. L. Cárdenas-Rozo, A. Wood, Early Miocene CO₂ estimates from a Neotropical fossil leaf assemblage exceed 400 ppm. *Am. J. Bot.* **105**, 1929–1937 (2018). [doi:10.1002/ajb2.1187](https://doi.org/10.1002/ajb2.1187) [Medline](#)
329. J. C. McElwain, I. Montañez, J. D. White, J. P. Wilson, C. Yiotis, Was atmospheric CO₂ capped at 1000 ppm over the past 300 million years? *Palaeogeogr. Palaeoclimatol. Palaeoecol.* **441**, 653–658 (2016). [doi:10.1016/j.palaeo.2015.10.017](https://doi.org/10.1016/j.palaeo.2015.10.017)
330. M. Murray, W. K. Soh, C. Yiotis, R. A. Spicer, T. Lawson, J. C. McElwain, Consistent relationship between field-measured stomatal conductance and theoretical maximum stomatal conductance in C₃ woody angiosperms in four major biomes. *Int. J. Plant Sci.* **181**, 142–154 (2020). [doi:10.1086/706260](https://doi.org/10.1086/706260)
331. T. Reichgelt, W. J. D'Andrea, Plant carbon assimilation rates in atmospheric CO₂ reconstructions. *New Phytol.* **223**, 1844–1855 (2019). [doi:10.1111/nph.15914](https://doi.org/10.1111/nph.15914) [Medline](#)

332. B. J. Fletcher, S. J. Brentnall, W. P. Quick, D. J. Beerling, BRYOCARB: A process-based model of thallose liverwort carbon isotope fractionation in response to CO₂, O₂, light and temperature. *Geochim. Cosmochim. Acta* **70**, 5676–5691 (2006). [doi:10.1016/j.gca.2006.01.031](https://doi.org/10.1016/j.gca.2006.01.031)
333. B. J. Fletcher, S. J. Brentnall, C. W. Anderson, R. A. Berner, D. J. Beerling, Atmospheric carbon dioxide linked with Mesozoic and early Cenozoic climate change. *Nat. Geosci.* **1**, 43–48 (2008). [doi:10.1038/ngeo.2007.29](https://doi.org/10.1038/ngeo.2007.29)
334. P. K. Van de Water, S. W. Leavitt, J. L. Betancourt, Trends in stomatal density and ¹³C/¹²C ratios of *Pinus flexilis* needles during last glacial-interglacial cycle. *Science* **264**, 239–243 (1994). [doi:10.1126/science.264.5156.239](https://doi.org/10.1126/science.264.5156.239) [Medline](#)
335. X. Feng, S. Epstein, Carbon isotopes of trees from arid environments and implications for reconstructing atmospheric CO₂ concentration. *Geochim. Cosmochim. Acta* **59**, 2599–2608 (1995). [doi:10.1016/0016-7037\(95\)00152-2](https://doi.org/10.1016/0016-7037(95)00152-2)
336. R. F. Keeling, H. D. Graven, L. R. Welp, L. Resplandy, J. Bi, S. C. Piper, Y. Sun, A. Bollenbacher, H. A. J. Meijer, Atmospheric evidence for a global secular increase in carbon isotopic discrimination of land photosynthesis. *Proc. Natl. Acad. Sci. U.S.A.* **114**, 10361–10366 (2017). [doi:10.1073/pnas.1619240114](https://doi.org/10.1073/pnas.1619240114) [Medline](#)
337. B. A. Schubert, A. H. Jahren, Incorporating the effects of photorespiration into terrestrial paleoclimate reconstruction. *Earth Sci. Rev.* **177**, 637–642 (2018). [doi:10.1016/j.earscirev.2017.12.008](https://doi.org/10.1016/j.earscirev.2017.12.008)
338. A. Wingler, P. J. Lea, W. P. Quick, R. C. Leegood, Photorespiration: Metabolic pathways and their role in stress protection. *Philos. Trans. R. Soc. Lond. B Biol. Sci.* **355**, 1517–1529 (2000). [doi:10.1098/rstb.2000.0712](https://doi.org/10.1098/rstb.2000.0712) [Medline](#)
339. S. Rachmilevitch, A. B. Cousins, A. J. Bloom, Nitrate assimilation in plant shoots depends on photorespiration. *Proc. Natl. Acad. Sci. U.S.A.* **101**, 11506–11510 (2004). [doi:10.1073/pnas.0404388101](https://doi.org/10.1073/pnas.0404388101) [Medline](#)
340. J. Jiao, B. Grodzinski, The effect of leaf temperature and photorespiratory conditions on export of sugars during steady-state photosynthesis in *Salvia splendens*. *Plant Physiol.* **111**, 169–178 (1996). [doi:10.1104/pp.111.1.169](https://doi.org/10.1104/pp.111.1.169) [Medline](#)
341. B. A. Schubert, A. H. Jahren, Global increase in plant carbon isotope fractionation following the Last Glacial Maximum caused by increase in atmospheric pCO₂. *Geology* **43**, 435–438 (2015). [doi:10.1130/G36467.1](https://doi.org/10.1130/G36467.1)
342. A. F. Diefendorf, K. H. Freeman, S. L. Wing, E. D. Currano, K. E. Mueller, Paleogene plants fractionated carbon isotopes similar to modern plants. *Earth Planet. Sci. Lett.* **429**, 33–44 (2015). [doi:10.1016/j.epsl.2015.07.029](https://doi.org/10.1016/j.epsl.2015.07.029)
343. V. J. Hare, E. Loftus, A. Jeffrey, C. B. Ramsey, Atmospheric CO₂ effect on stable carbon isotope composition of terrestrial fossil archives. *Nat. Commun.* **9**, 252 (2018). [doi:10.1038/s41467-017-02691-x](https://doi.org/10.1038/s41467-017-02691-x) [Medline](#)
344. K. Schlanser, A. F. Diefendorf, D. R. Greenwood, K. E. Mueller, C. K. West, A. J. Lowe, J. F. Basinger, E. D. Currano, A. G. Flynn, H. C. Fricke, J. Geng, H. W. Meyer, D. J. Peppe, On geologic timescales, plant carbon isotope fractionation responds to

- precipitation similarly to modern plants and has a small negative correlation with $p\text{CO}_2$. *Geochim. Cosmochim. Acta* **270**, 264–281 (2020). [doi:10.1016/j.gca.2019.11.023](https://doi.org/10.1016/j.gca.2019.11.023)
345. M. J. Kohn, Carbon isotope discrimination in C3 land plants is independent of natural variations in $p\text{CO}_2$. *Geochem. Perspect. Lett.* **2**, 35–43 (2016). [doi:10.7185/geochemlet.1604](https://doi.org/10.7185/geochemlet.1604)
346. Y. Cui, B. A. Schubert, A. H. Jahren, A 23 m.y. record of low atmospheric CO_2 . *Geology* **48**, 888–892 (2020). [doi:10.1130/G47681.1](https://doi.org/10.1130/G47681.1)
347. V. J. Hare, A. Lavergne, Differences in carbon isotope discrimination between angiosperm and gymnosperm woody plants, and their geological significance. *Geochim. Cosmochim. Acta* **300**, 215–230 (2021). [doi:10.1016/j.gca.2021.02.029](https://doi.org/10.1016/j.gca.2021.02.029)
348. Y. Cui, B. A. Schubert, Towards determination of the source and magnitude of atmospheric $p\text{CO}_2$ change across the early Paleogene hyperthermals. *Global Planet. Change* **170**, 120–125 (2018). [doi:10.1016/j.gloplacha.2018.08.011](https://doi.org/10.1016/j.gloplacha.2018.08.011)
349. P. L. Koch, J. C. Zachos, P. D. Gingerich, Correlation between isotope records in marine and continental carbon reservoirs near the Palaeocene/Eocene boundary. *Nature* **358**, 319–322 (1992). [doi:10.1038/358319a0](https://doi.org/10.1038/358319a0)
350. A. Sinha, L. D. Stott, New atmospheric $p\text{CO}_2$ estimates from palesols during the late Paleocene/early Eocene global warming interval. *Global Planet. Change* **9**, 297–307 (1994). [doi:10.1016/0921-8181\(94\)00010-7](https://doi.org/10.1016/0921-8181(94)00010-7)
351. Y. Cui, B. A. Schubert, Atmospheric $p\text{CO}_2$ reconstructed across five early Eocene global warming events. *Earth Planet. Sci. Lett.* **478**, 225–233 (2017). [doi:10.1016/j.epsl.2017.08.038](https://doi.org/10.1016/j.epsl.2017.08.038)
352. B. H. Lomax, J. A. Lake, M. J. Leng, P. E. Jardine, An experimental evaluation of the use of $\Delta^{13}\text{C}$ as a proxy for palaeoatmospheric CO_2 . *Geochim. Cosmochim. Acta* **247**, 162–174 (2019). [doi:10.1016/j.gca.2018.12.026](https://doi.org/10.1016/j.gca.2018.12.026)
353. A. S. Porter, C. Yiotis, I. P. Montañez, J. C. McElwain, Evolutionary differences in $\Delta^{13}\text{C}$ detected between spore and seed bearing plants following exposure to a range of atmospheric $\text{O}_2\text{:CO}_2$ ratios; implications for paleoatmosphere reconstruction. *Geochim. Cosmochim. Acta* **213**, 517–533 (2017). [doi:10.1016/j.gca.2017.07.007](https://doi.org/10.1016/j.gca.2017.07.007)
354. M. A. Scher, R. S. Barclay, A. A. Baczynski, B. A. Smith, J. Sappington, L. A. Bennett, S. Chakraborty, J. P. Wilson, J. P. Megonigal, S. L. Wing, The effect of CO_2 concentration on carbon isotope discrimination during photosynthesis in *Ginkgo biloba*: Implications for reconstructing atmospheric CO_2 levels in the geologic past. *Geochim. Cosmochim. Acta* **337**, 82–94 (2022). [doi:10.1016/j.gca.2022.09.033](https://doi.org/10.1016/j.gca.2022.09.033)
355. A. F. Diefendorf, K. E. Mueller, S. L. Wing, P. L. Koch, K. H. Freeman, Global patterns in leaf ^{13}C discrimination and implications for studies of past and future climate. *Proc. Natl. Acad. Sci. U.S.A.* **107**, 5738–5743 (2010). [doi:10.1073/pnas.0910513107](https://doi.org/10.1073/pnas.0910513107) [Medline](#)
356. V. Galy, L. François, C. France-Lanord, P. Faure, H. Kudrass, F. Palhol, S. K. Singh, C4 plants decline in the Himalayan basin since the Last Glacial Maximum. *Quat. Sci. Rev.* **27**, 1396–1409 (2008). [doi:10.1016/j.quascirev.2008.04.005](https://doi.org/10.1016/j.quascirev.2008.04.005)

357. D. A. Stolper, M. L. Bender, G. B. Dreyfus, Y. Yan, J. A. Higgins, A Pleistocene ice core record of atmospheric O₂ concentrations. *Science* **353**, 1427–1430 (2016).
[doi:10.1126/science.aaf5445](https://doi.org/10.1126/science.aaf5445) [Medline](#)
358. D. C. Wade, N. L. Abraham, A. Farnsworth, P. J. Valdes, F. Bragg, A. T. Archibald, Simulating the climate response to atmospheric oxygen variability in the Phanerozoic: A focus on the Holocene, Cretaceous and Permian. *Clim. Past* **15**, 1463–1483 (2019).
[doi:10.5194/cp-15-1463-2019](https://doi.org/10.5194/cp-15-1463-2019)
359. D. C. Frank, B. Poulter, M. Saurer, J. Esper, C. Huntingford, G. Helle, K. Treydte, N. E. Zimmermann, G. H. Schleser, A. Ahlström, P. Ciais, P. Friedlingstein, S. Levis, M. Lomas, S. Sitch, N. Viovy, L. Andreu-Hayles, Z. Bednarczyk, F. Berninger, T. Boettger, C. M. D’Alessandro, V. Daux, M. Filot, M. Grabner, E. Gutierrez, M. Haupt, E. Hiltunen, H. Jungner, M. Kalela-Brundin, M. Krapiec, M. Leuenberger, N. J. Loader, H. Marah, V. Masson-Delmotte, A. Pazdur, S. Pawelczyk, M. Pierre, O. Planells, R. Pukienė, C. E. Reynolds-Henne, K. T. Rinne, A. Saracino, E. Sonninen, M. Stievenard, V. R. Switsur, M. Szczepanek, E. Szychowska-Krapiec, L. Todaro, J. S. Waterhouse, M. Weigl, Water-use efficiency and transpiration across European forests during the Anthropocene. *Nat. Clim. Chang.* **5**, 579–583 (2015). [doi:10.1038/nclimate2614](https://doi.org/10.1038/nclimate2614)
360. D. O. Breecker, Atmospheric pCO₂ control on speleothem stable carbon isotope compositions. *Earth Planet. Sci. Lett.* **458**, 58–68 (2017). [doi:10.1016/j.epsl.2016.10.042](https://doi.org/10.1016/j.epsl.2016.10.042)
361. R. A. Stein, N. D. Sheldon, S. Y. Smith, C₃ plant carbon isotope discrimination does not respond to CO₂ concentration on decadal to centennial timescales. *New Phytol.* **229**, 2576–2585 (2021). [doi:10.1111/nph.17030](https://doi.org/10.1111/nph.17030) [Medline](#)
362. G. Mora, A. M. Carmo, W. Elliott, Homeostatic response of Aptian gymnosperms to changes in atmospheric CO₂ concentrations. *Geology* **49**, 703–707 (2021).
[doi:10.1130/G48037.1](https://doi.org/10.1130/G48037.1)
363. H.-Y. Zhang, H. Hartmann, G. Gleixner, M. Thoma, V. F. Schwab, Carbon isotope fractionation including photosynthetic and post-photosynthetic processes in C₃ plants: Low [CO₂] matters. *Geochim. Cosmochim. Acta* **245**, 1–15 (2019).
[doi:10.1016/j.gca.2018.09.035](https://doi.org/10.1016/j.gca.2018.09.035)
364. C. J. Hollis, T. Dunkley Jones, E. Anagnostou, P. K. Bijl, M. J. Cramwinckel, Y. Cui, G. R. Dickens, K. M. Edgar, Y. Eley, D. Evans, G. L. Foster, J. Frieling, G. N. Inglis, E. M. Kennedy, R. Kozdon, V. Laetani, C. H. Lear, K. Littler, L. Lourens, A. N. Meckler, B. D. A. Naafs, H. Pälike, R. D. Pancost, P. N. Pearson, U. Röhl, D. L. Royer, U. Salzmann, B. A. Schubert, H. Seebeck, A. Sluijs, R. P. Speijer, P. Stassen, J. Tierney, A. Tripathi, B. Wade, T. Westerhold, C. Witkowski, J. C. Zachos, Y. G. Zhang, M. Huber, D. J. Lunt, The DeepMIP contribution to PMIP4: Methodologies for selection, compilation and analysis of latest Paleocene and early Eocene climate proxy data, incorporating version 0.1 of the DeepMIP database. *Geosci. Model Dev.* **12**, 3149–3206 (2019).
[doi:10.5194/gmd-12-3149-2019](https://doi.org/10.5194/gmd-12-3149-2019)
365. Y. Cui, B. A. Schubert, Quantifying uncertainty of past pCO₂ determined from changes in C₃ plant carbon isotope fractionation. *Geochim. Cosmochim. Acta* **172**, 127–138 (2016).
[doi:10.1016/j.gca.2015.09.032](https://doi.org/10.1016/j.gca.2015.09.032)

366. M. J. Kohn, Carbon isotope compositions of terrestrial C3 plants as indicators of (paleo)ecology and (paleo)climate. *Proc. Natl. Acad. Sci. U.S.A.* **107**, 19691–19695 (2010). [doi:10.1073/pnas.1004933107](https://doi.org/10.1073/pnas.1004933107) [Medline](#)
367. R. J. Brien, G. Helle, T. L. Pons, J.-L. Guyot, M. Gloor, Oxygen isotopes in tree rings are a good proxy for Amazon precipitation and El Niño-Southern Oscillation variability. *Proc. Natl. Acad. Sci. U.S.A.* **109**, 16957–16962 (2012). [doi:10.1073/pnas.1205977109](https://doi.org/10.1073/pnas.1205977109) [Medline](#)
368. J. Franke, D. Frank, C. C. Raible, J. Esper, S. Brönnimann, Spectral biases in tree-ring climate proxies. *Nat. Clim. Chang.* **3**, 360–364 (2013). [doi:10.1038/nclimate1816](https://doi.org/10.1038/nclimate1816)
369. J. Pechtl, A. Land, Tree rings as a proxy for seasonal precipitation variability and Early Neolithic settlement dynamics in Bavaria, Germany. *PLOS ONE* **14**, e0210438 (2019). [doi:10.1371/journal.pone.0210438](https://doi.org/10.1371/journal.pone.0210438) [Medline](#)
370. P. Wilf, S. L. Wing, D. R. Greenwood, C. L. Greenwood, Using fossil leaves as paleoprecipitation indicators: An Eocene example. *Geology* **26**, 203 (1998). [doi:10.1130/0091-7613\(1998\)026<0203:UFLAPI>2.3.CO;2](https://doi.org/10.1130/0091-7613(1998)026<0203:UFLAPI>2.3.CO;2)
371. I. S. Castañeda, S. Schouten, A review of molecular organic proxies for examining modern and ancient lacustrine environments. *Quat. Sci. Rev.* **30**, 2851–2891 (2011). [doi:10.1016/j.quascirev.2011.07.009](https://doi.org/10.1016/j.quascirev.2011.07.009)
372. G. E. Stinchcomb, L. C. Nordt, S. G. Driese, W. E. Lukens, F. C. Williamson, J. D. Tubbs, A data-driven spline model designed to predict paleoclimate using paleosol geochemistry. *Am. J. Sci.* **316**, 746–777 (2016). [doi:10.2475/08.2016.02](https://doi.org/10.2475/08.2016.02)
373. S. A. Blumenthal, N. E. Levin, F. H. Brown, J.-P. Brugal, K. L. Chritz, J. M. Harris, G. E. Jehle, T. E. Cerling, Aridity and hominin environments. *Proc. Natl. Acad. Sci. U.S.A.* **114**, 7331–7336 (2017). [doi:10.1073/pnas.1700597114](https://doi.org/10.1073/pnas.1700597114) [Medline](#)
374. N. E. Levin, T. E. Cerling, B. H. Passey, J. M. Harris, J. R. Ehleringer, A stable isotope aridity index for terrestrial environments. *Proc. Natl. Acad. Sci. U.S.A.* **103**, 11201–11205 (2006). [doi:10.1073/pnas.0604719103](https://doi.org/10.1073/pnas.0604719103) [Medline](#)
375. B. H. Passey, N. E. Levin, Triple oxygen isotopes in meteoric waters, carbonates, and biological apatites: Implications for continental paleoclimate reconstruction. *Rev. Mineral. Geochem.* **86**, 429–462 (2020). [doi:10.2138/rmg.2021.86.13](https://doi.org/10.2138/rmg.2021.86.13)
376. B. H. Passey, H. Ji, Triple oxygen isotope signatures of evaporation in lake waters and carbonates: A case study from the western United States. *Earth Planet. Sci. Lett.* **518**, 1–12 (2019). [doi:10.1016/j.epsl.2019.04.026](https://doi.org/10.1016/j.epsl.2019.04.026)
377. T. E. Cerling, Stable carbon isotopes in paleosol carbonates. *Spec. Publ. Int. Assoc. Sedimentol.* **27**, 43–60 (1999).
378. W. Jost, *Diffusion in Solids, Liquids, and Gases* (Academic Press, 1960).
379. H. Craig, The geochemistry of the stable carbon isotopes. *Geochim. Cosmochim. Acta* **3**, 53–92 (1954). [doi:10.1016/0016-7037\(53\)90001-5](https://doi.org/10.1016/0016-7037(53)90001-5)

380. N. C. Arens, A. H. Jahren, R. Amundson, Can C3 plants faithfully record the carbon isotopic composition of atmospheric carbon dioxide? *Paleobiology* **26**, 137–164 (2000). [doi:10.1666/0094-8373\(2000\)026<0137:CCPFRT>2.0.CO;2](https://doi.org/10.1666/0094-8373(2000)026<0137:CCPFRT>2.0.CO;2)
381. J. Balesdent, C. Girardin, A. Mariotti, Site-related $\delta^{13}\text{C}$ of tree leaves and soil organic matter in a temperate forest. *Ecology* **74**, 1713–1721 (1993). [doi:10.2307/1939930](https://doi.org/10.2307/1939930)
382. M. Brunn, S. Spielvogel, T. Sauer, Y. Oelmann, Temperature and precipitation effects on $\delta^{13}\text{C}$ depth profiles in SOM under temperate beech forests. *Geoderma* **235-236**, 146–153 (2014). [doi:10.1016/j.geoderma.2014.07.007](https://doi.org/10.1016/j.geoderma.2014.07.007)
383. C. D. Keeling, The Suess effect: ^{13}C - ^{14}C interrelations. *Environ. Int.* **2**, 229–300 (1979). [doi:10.1016/0160-4120\(79\)90005-9](https://doi.org/10.1016/0160-4120(79)90005-9)
384. M. S. Torn, A. G. Lapenis, A. Timofeev, M. L. Fischer, B. V. Babikov, J. W. Harden, Organic carbon and carbon isotopes in modern and 100-year-old-soil archives of the Russian steppe. *Glob. Change Biol.* **8**, 941–953 (2002). [doi:10.1046/j.1365-2486.2002.00477.x](https://doi.org/10.1046/j.1365-2486.2002.00477.x)
385. M. A. Poage, X. Feng, A theoretical analysis of steady state $\delta^{13}\text{C}$ profiles of soil organic matter. *Global Biogeochem. Cycles* **18**, GB2016 (2004). [doi:10.1029/2003GB002195](https://doi.org/10.1029/2003GB002195)
386. J. G. Wynn, Carbon isotope fractionation during decomposition of organic matter in soils and paleosols: Implications for paleoecological interpretations of paleosols. *Palaeogeogr. Palaeoclimatol. Palaeoecol.* **251**, 437–448 (2007). [doi:10.1016/j.palaeo.2007.04.009](https://doi.org/10.1016/j.palaeo.2007.04.009)
387. D. O. Breecker, S. Bergel, M. Nadel, M. M. Tremblay, R. Osuna-Orozco, T. E. Larson, Z. D. Sharp, Minor stable carbon isotope fractionation between respired carbon dioxide and bulk soil organic matter during laboratory incubation of topsoil. *Biogeochemistry* **123**, 83–98 (2015). [doi:10.1007/s10533-014-0054-3](https://doi.org/10.1007/s10533-014-0054-3)
388. B. H. Passey, N. E. Levin, T. E. Cerling, F. H. Brown, J. M. Eiler, High-temperature environments of human evolution in East Africa based on bond ordering in paleosol carbonates. *Proc. Natl. Acad. Sci. U.S.A.* **107**, 11245–11249 (2010). [doi:10.1073/pnas.1001824107](https://doi.org/10.1073/pnas.1001824107) [Medline](#)
389. J. Quade, J. Eiler, M. Daëron, H. Achyuthan, The clumped isotope geothermometer in soil and paleosol carbonate. *Geochim. Cosmochim. Acta* **105**, 92–107 (2013). [doi:10.1016/j.gca.2012.11.031](https://doi.org/10.1016/j.gca.2012.11.031)
390. J. R. Kelson, K. W. Huntington, D. O. Breecker, L. K. Burgener, T. M. Gallagher, G. D. Hoke, S. V. Petersen, A proxy for all seasons? A synthesis of clumped isotope data from Holocene soil carbonates. *Quat. Sci. Rev.* **234**, 106259 (2020). [doi:10.1016/j.quascirev.2020.106259](https://doi.org/10.1016/j.quascirev.2020.106259)
391. E. O. Heitmann, S. Ji, J. Nie, D. O. Breecker, Orbitally-paced variations of water availability in the SE Asian Monsoon region following the Miocene Climate Transition. *Earth Planet. Sci. Lett.* **474**, 272–282 (2017). [doi:10.1016/j.epsl.2017.06.006](https://doi.org/10.1016/j.epsl.2017.06.006)
392. L. Zhang, C. Wang, P. B. Wignall, T. Kluge, X. Wan, Q. Wang, Y. Gao, Deccan volcanism caused coupled $p\text{CO}_2$ and terrestrial temperature rises, and pre-impact extinctions in northern China. *Geology* **46**, 271–274 (2018). [doi:10.1130/G39992.1](https://doi.org/10.1130/G39992.1)

393. C. Huang, G. J. Retallack, C. Wang, Q. Huang, Paleatmospheric pCO₂ fluctuations across the Cretaceous–Tertiary boundary recorded from paleosol carbonates in NE China. *Palaeogeogr. Palaeoclimatol. Palaeoecol.* **385**, 95–105 (2013). [doi:10.1016/j.palaeo.2013.01.005](https://doi.org/10.1016/j.palaeo.2013.01.005)
394. G. A. Brook, M. E. Folkoff, E. O. Box, A world model of soil carbon dioxide. *Earth Surf. Process. Landf.* **8**, 79–88 (1983). [doi:10.1002/esp.3290080108](https://doi.org/10.1002/esp.3290080108)
395. A. Indermühle, T. F. Stocker, F. Joos, H. Fischer, H. J. Smith, M. Wahlen, B. Deck, D. Mastroianni, J. Tschumi, T. Blunier, R. Meyer, B. Stauffer, Holocene carbon-cycle dynamics based on CO₂ trapped in ice at Taylor Dome, Antarctica. *Nature* **398**, 121–126 (1999). [doi:10.1038/18158](https://doi.org/10.1038/18158)
396. D. O. Breecker, Z. D. Sharp, L. D. McFadden, Atmospheric CO₂ concentrations during ancient greenhouse climates were similar to those predicted for A.D. 2100. *Proc. Natl. Acad. Sci. U.S.A.* **107**, 576–580 (2010). [doi:10.1073/pnas.0902323106](https://doi.org/10.1073/pnas.0902323106) [Medline](#)
397. I. P. Montañez, Modern soil system constraints on reconstructing deep-time atmospheric CO₂. *Geochim. Cosmochim. Acta* **101**, 57–75 (2013). [doi:10.1016/j.gca.2012.10.012](https://doi.org/10.1016/j.gca.2012.10.012)
398. J. M. Cotton, N. D. Sheldon, New constraints on using paleosols to reconstruct atmospheric pCO₂. *Geol. Soc. Am. Bull.* **124**, 1411–1423 (2012). [doi:10.1130/B30607.1](https://doi.org/10.1130/B30607.1)
399. D. O. Breecker, G. J. Retallack, Refining the pedogenic carbonate atmospheric CO₂ proxy and application to Miocene CO₂. *Palaeogeogr. Palaeoclimatol. Palaeoecol.* **406**, 1–8 (2014). [doi:10.1016/j.palaeo.2014.04.012](https://doi.org/10.1016/j.palaeo.2014.04.012)
400. B. A. Maher, R. Thompson, Paleorainfall reconstructions from pedogenic magnetic susceptibility variations in the Chinese loess and paleosols. *Quat. Res.* **44**, 383–391 (1995). [doi:10.1006/qres.1995.1083](https://doi.org/10.1006/qres.1995.1083)
401. T. E. Huth, T. E. Cerling, D. W. Marchetti, D. R. Bowling, A. L. Ellwein, B. H. Passey, Seasonal bias in soil carbonate formation and its implications for interpreting high-resolution paleoarchives: Evidence from Southern Utah. *J. Geophys. Res. Biogeosci.* **124**, 616–632 (2019). [doi:10.1029/2018JG004496](https://doi.org/10.1029/2018JG004496)
402. D. O. Breecker, Improving paleosol carbonate based estimates of ancient atmospheric CO₂. *Geochem. News*, no. 144, September 2010 issue (2010); <https://www.geochemsoc.org/publications/geochemicalnews/gn144sep10/improvingpaleosolcarbonate>.
403. Y. Gao, D. E. Ibarra, J. K. Caves Rügenstein, J. Chen, T. Kukla, K. Methner, Y. Gao, H. Huang, Z. Lin, L. Zhang, D. Xi, H. Wu, A. R. Carroll, S. A. Graham, C. P. Chamberlain, C. Wang, Terrestrial climate in mid-latitude East Asia from the latest Cretaceous to the earliest Paleogene: A multiproxy record from the Songliao Basin in northeastern China. *Earth Sci. Rev.* **216**, 103572 (2021). [doi:10.1016/j.earscirev.2021.103572](https://doi.org/10.1016/j.earscirev.2021.103572)
404. T. E. Cerling, Use of carbon isotopes in paleosols as an indicator of the P(CO₂) of the paleoatmosphere. *Global Biogeochem. Cycles* **6**, 307–314 (1992). [doi:10.1029/92GB01102](https://doi.org/10.1029/92GB01102)

405. J. Da, Y. G. Zhang, H. Wang, W. Balsam, J. Ji, An Early Pleistocene atmospheric CO₂ record based on pedogenic carbonate from the Chinese loess deposits. *Earth Planet. Sci. Lett.* **426**, 69–75 (2015). [doi:10.1016/j.epsl.2015.05.053](https://doi.org/10.1016/j.epsl.2015.05.053)
406. D. D. Ekart, T. E. Cerling, I. P. Montañez, N. J. Tabor, A 400 million year carbon isotope record of pedogenic carbonate; implications for paleoatmospheric carbon dioxide. *Am. J. Sci.* **299**, 805–827 (1999). [doi:10.2475/ajs.299.10.805](https://doi.org/10.2475/ajs.299.10.805)
407. L. Nordt, S. Atchley, S. Dworkin, Paleosol barometer indicates extreme fluctuations in atmospheric CO₂ across the Cretaceous-Tertiary boundary. *Geology* **30**, 703 (2002). [doi:10.1130/0091-7613\(2002\)030<0703:PBIEFI>2.0.CO;2](https://doi.org/10.1130/0091-7613(2002)030<0703:PBIEFI>2.0.CO;2)
408. L. Nordt, S. Atchley, S. Dworkin, Terrestrial evidence for two greenhouse events in the latest Cretaceous. *GSA Today* **13**, 4 (2003). [doi:10.1130/1052-5173\(2003\)013<4:TEFTGE>2.0.CO;2](https://doi.org/10.1130/1052-5173(2003)013<4:TEFTGE>2.0.CO;2)
409. G. J. Retallack, Refining a pedogenic-carbonate CO₂ paleobarometer to quantify a middle Miocene greenhouse spike. *Palaeogeogr. Palaeoclimatol. Palaeoecol.* **281**, 57–65 (2009). [doi:10.1016/j.palaeo.2009.07.011](https://doi.org/10.1016/j.palaeo.2009.07.011)
410. P. Srivastava, S. Patel, N. Singh, T. Jamir, N. Kumar, M. Aruche, R. C. Patel, Early Oligocene paleosols of the Dagshai Formation, India: A record of the oldest tropical weathering in the Himalayan foreland. *Sediment. Geol.* **294**, 142–156 (2013). [doi:10.1016/j.sedgeo.2013.05.011](https://doi.org/10.1016/j.sedgeo.2013.05.011)
411. L. Nordt, J. Tubbs, S. Dworkin, Stable carbon isotope record of terrestrial organic materials for the last 450 Ma yr. *Earth Sci. Rev.* **159**, 103–117 (2016). [doi:10.1016/j.earscirev.2016.05.007](https://doi.org/10.1016/j.earscirev.2016.05.007)
412. M. J. Kohn, C. A. E. Strömberg, R. H. Madden, R. E. Dunn, S. Evans, A. Palacios, A. A. Carlini, Quasi-static Eocene–Oligocene climate in Patagonia promotes slow faunal evolution and mid-Cenozoic global cooling. *Palaeogeogr. Palaeoclimatol. Palaeoecol.* **435**, 24–37 (2015). [doi:10.1016/j.palaeo.2015.05.028](https://doi.org/10.1016/j.palaeo.2015.05.028)
413. N. D. Sheldon, G. J. Retallack, S. Tanaka, Geochemical climofunctions from North American soils and application to paleosols across the Eocene-Oligocene boundary in Oregon. *J. Geol.* **110**, 687–696 (2002). [doi:10.1086/342865](https://doi.org/10.1086/342865)
414. N. D. Sheldon, N. J. Tabor, Quantitative paleoenvironmental and paleoclimatic reconstruction using paleosols. *Earth Sci. Rev.* **95**, 1–52 (2009). [doi:10.1016/j.earscirev.2009.03.004](https://doi.org/10.1016/j.earscirev.2009.03.004)
415. A. Licht, G. Dupont-Nivet, N. Meijer, J. Caves Rugenstein, A. Schauer, J. Fiebig, A. Mulch, C. Hoorn, N. Barbolini, Z. Guo, Decline of soil respiration in northeastern Tibet through the transition into the Oligocene icehouse. *Palaeogeogr. Palaeoclimatol. Palaeoecol.* **560**, 110016 (2020). [doi:10.1016/j.palaeo.2020.110016](https://doi.org/10.1016/j.palaeo.2020.110016)
416. J. M. Cotton, N. D. Sheldon, M. T. Hren, T. M. Gallagher, Positive feedback drives carbon release from soils to atmosphere during Paleocene/Eocene warming. *Am. J. Sci.* **315**, 337–361 (2015). [doi:10.2475/04.2015.03](https://doi.org/10.2475/04.2015.03)
417. T. M. Gallagher, C. G. Cacciatore, D. O. Breecker, Interpreting the difference in magnitudes of PETM carbon isotope excursions in paleosol carbonate and organic

- matter: Oxidation of methane in soils versus elevated soil respiration rates. *Paleoceanogr. Paleoclimatol.* **34**, 2113–2128 (2019). [doi:10.1029/2019PA003596](https://doi.org/10.1029/2019PA003596)
418. T. M. Gallagher, L. Serach, N. Sekhon, H. Zhang, H. Wang, S. Ji, X. Chang, H. Lu, D. O. Breecker, Regional patterns in Miocene-Pliocene aridity across the Chinese loess plateau revealed by high resolution records of paleosol carbonate and occluded organic matter. *Paleoceanogr. Paleoclimatol.* **36**, e2021PA004344 (2021). [doi:10.1029/2021PA004344](https://doi.org/10.1029/2021PA004344)
419. A. Barral, B. Gomez, S. Legendre, C. Lécuyer, Evolution of the carbon isotope composition of atmospheric CO₂ throughout the Cretaceous. *Palaeogeogr. Palaeoclimatol. Palaeoecol.* **471**, 40–47 (2017). [doi:10.1016/j.palaeo.2017.01.034](https://doi.org/10.1016/j.palaeo.2017.01.034)
420. H. P. Eugster, Sodium carbonate-bicarbonate minerals as indicators of Pco₂. *J. Geophys. Res.* **71**, 3369–3377 (1966). [doi:10.1029/JZ071i014p03369](https://doi.org/10.1029/JZ071i014p03369)
421. R. V. Demicco, T. K. Lowenstein, When “evaporites” are not formed by evaporation: The role of temperature and pCO₂ on saline deposits of the Eocene Green River Formation, Colorado, USA. *Geol. Soc. Am. Bull.* **132**, 1365–1380 (2019). [doi:10.1130/B35303.1](https://doi.org/10.1130/B35303.1)
422. E. Guillerm, V. Gardien, D. Ariztegui, F. Caupin, Restoring halite fluid inclusions as an accurate palaeothermometer: Brillouin thermometry versus microthermometry. *Geostand. Geoanal. Res.* **44**, 243–264 (2020). [doi:10.1111/ggr.12312](https://doi.org/10.1111/ggr.12312)
423. C. M. Duarte, Y. T. Prairie, C. Montes, J. J. Cole, R. Strieg, J. Melack, J. A. Downing, CO₂ emissions from saline lakes: A global estimate of a surprisingly large flux. *J. Geophys. Res.* **113**, G04041 (2008).
424. R. Golan, I. Gavrieli, J. Ganor, B. Lazar, Controls on the pH of hyper-saline lakes – A lesson from the Dead Sea. *Earth Planet. Sci. Lett.* **434**, 289–297 (2016). [doi:10.1016/j.epsl.2015.11.022](https://doi.org/10.1016/j.epsl.2015.11.022)
425. L. E. Lisiecki, M. E. Raymo, A Pliocene-Pleistocene stack of 57 globally distributed benthic δ¹⁸O records. *Paleoceanography* **20**, 2004PA001071 (2005). [doi:10.1029/2004PA001071](https://doi.org/10.1029/2004PA001071)
426. G. J. Bowen, SPATIAL-Lab/CenoCO₂: for publication (v1.1), Zenodo (2023); <https://doi.org/10.5281/zenodo.10162425>.
427. R. A. Berner, A. C. Lasaga, R. M. Garrels, The carbonate-silicate geochemical cycle and its effect on atmospheric carbon dioxide over the past 100 million years. *Am. J. Sci.* **283**, 641–683 (1983). [doi:10.2475/ajs.283.7.641](https://doi.org/10.2475/ajs.283.7.641)
428. J. K. Caves, A. B. Jost, K. V. Lau, K. Maher, Cenozoic carbon cycle imbalances and a variable weathering feedback. *Earth Planet. Sci. Lett.* **450**, 152–163 (2016). [doi:10.1016/j.epsl.2016.06.035](https://doi.org/10.1016/j.epsl.2016.06.035)
429. N. Komar, R. E. Zeebe, G. R. Dickens, Understanding long-term carbon cycle trends: The late Paleocene through the early Eocene. *Paleoceanography* **28**, 650–662 (2013). [doi:10.1002/palo.20060](https://doi.org/10.1002/palo.20060)
430. M. Plummer, “JAGS: A program for analysis of Bayesian graphical models using Gibbs sampling” in *Proceedings of the 3rd International Workshop on Distributed Statistical Computing*, vol. 124, no. 125.10, pp. 1–10 (2003).

431. R Core Team, R: A Language and Environment for Statistical Computing (R Foundation for Statistical Computing, 2022); <https://www.R-project.org>.
432. Y. Su, M. Yajima, R2jags: Using R to Run ‘JAGS,’ R package version 0.7-1 (2021); <https://CRAN.R-project.org/package=R2jags>.
433. M. Plummer, rjags: Bayesian Graphical Models using MCMC, R package version 4-14 (2023); <https://CRAN.R-project.org/package=rjags>.
434. A. Gelman, D. B. Rubin, Inference from iterative simulation using multiple sequences. *Stat. Sci.* **7**, 457–472 (1992). [doi:10.1214/ss/1177011136](https://doi.org/10.1214/ss/1177011136)
435. T. M. Marchitto, W. B. Curry, J. Lynch-Stieglitz, S. P. Bryan, K. M. Cobb, D. C. Lund, Improved oxygen isotope temperature calibrations for cosmopolitan benthic foraminifera. *Geochim. Cosmochim. Acta* **130**, 1–11 (2014). [doi:10.1016/j.gca.2013.12.034](https://doi.org/10.1016/j.gca.2013.12.034)
436. J. Ahn, E. J. Brook, L. Mitchell, J. Rosen, J. R. McConnell, K. Taylor, D. Etheridge, M. Rubino, Atmospheric CO₂ over the last 1000 years: A high-resolution record from the West Antarctic Ice Sheet (WAIS) Divide ice core. *Global Biogeochem. Cycles* **26**, GB2027 (2012). [doi:10.1029/2011GB004247](https://doi.org/10.1029/2011GB004247)
437. M. E. Raymo, L. E. Lisiecki, K. H. Nisancioglu, Plio-Pleistocene ice volume, Antarctic climate, and the global $\delta^{18}\text{O}$ record. *Science* **313**, 492–495 (2006). [doi:10.1126/science.1123296](https://doi.org/10.1126/science.1123296) [Medline](#)
438. U. Riebesell, A. T. Revill, D. G. Holdsworth, J. K. Volkman, The effects of varying CO₂ concentration on lipid composition and carbon isotope fractionation in *Emiliana huxleyi*. *Geochim. Cosmochim. Acta* **64**, 4179–4192 (2000). [doi:10.1016/S0016-7037\(00\)00474-9](https://doi.org/10.1016/S0016-7037(00)00474-9)
439. E. B. Wilkes, R. B. Y. Lee, H. L. O. McClelland, R. E. M. Rickaby, A. Pearson, Carbon isotope ratios of coccolith-associated polysaccharides of *Emiliana huxleyi* as a function of growth rate and CO₂ concentration. *Org. Geochem.* **119**, 1–10 (2018). [doi:10.1016/j.orggeochem.2018.02.006](https://doi.org/10.1016/j.orggeochem.2018.02.006)